Lawrence Berkeley National Laboratory

LBL Publications

Title

Utilizing Oxygen Redox in Layered Cathode Materials from Multiscale Perspective

Permalink

https://escholarship.org/uc/item/95z08130

Journal

Advanced Energy Materials, 11(27)

ISSN

1614-6832

Authors

Lee, Gi-Hyeok
Lau, Vincent Wing-hei
Yang, Wanli
et al.

Publication Date

2021-07-01

DOI

10.1002/aenm.202003227

Peer reviewed

Utilizing oxygen redox in cathodic layered oxide materials from multi-scale perspective

Gi-Hyeok Lee†, Dr. Vincent Wing-hei Lau†, Dr. Wanli Yang* and Prof. Yong-Mook Kang*

G.-H. Lee, Dr. W. Yang

Advanced Light Source, Lawrence Berkeley National Laboratory, Berkeley, CA 94720

(USA)

E-mail: wlyang@lbl.gov

Dr. V. W. Lau, Prof. Y.-M. Kang

Department of Materials Science and Engineering, Korea University, Seoul 02841 (Republic

of Korea)

E-mail: dake1234@korea.ac.kr

G.-H. Lee

Department of Energy and Materials Engineering, Dongguk University—Seoul, Seoul 04620

(Republic of Korea)

Abstract

In high-capacity layered oxide cathode materials, utilization of lattice oxygen as a redox

center is considered to be one of the promising approaches to achieve capacity exceeding the

limitation set by conventional transition metal redox center. However, rapid material

deteriorations are often associated with the oxygen oxidation, leading to formidable

challenges on utilizing oxygen redox reactions in batteries. Further mechanistic

understanding of the oxygen activities thus becomes critical to better control the oxygen

redox reactions. This review summarizes recent advances in the investigation of oxygen

redox reactions in cathode materials from a multiscale perspective, i.e., from the atomistic

level to the microstructure regime. We first discuss the mechanistic aspects of oxygen redox

and the consequences of this reaction on various electrode degradation pathways during

battery operation (e.g. oxygen loss, transition metal migration, irreversible phase transition),

relating structural changes at the crystallographic scale to those in the macro scale. We then

recount recent developments based on atomic and microstructure modifications that are

promising for improving the reversibility of oxygen redox reaction or mitigating the harmful

processes arising from oxidation of the oxygen centers under high operating voltage. We

conclude our analysis with a commentary on further research directions for optimizing the

oxygen activity for high-capacity charge storage.

1. Introduction

Layered oxides that can reversibly intercalate and deintercalate lithium ions with the charge

balanced through a redox-intercalation mechanism has long been recognized for their

applicability as battery cathode materials. Their high energy density can be attributed to the

high potential of the transition metal (TM) redox, a reaction that involves electrons in the TM

d-orbitals hybridized with oxygen (O) 2p orbitals.[1] It is the high energy density that this

class of cathode materials retain their leading positions in the Li-ion battery market since its

first commercialization based on LiCoO$_2$ (LCO) cathodes by Sony in 1992. The major

research efforts to date have focused on performance improvements as demanded by today's

sustainable energy applications, especially on longer cycle life, higher energy density and low

cost. Optimizing the cycle life involves overcoming the degradation mechanisms of $LiTMO_2$ in the highly delithiated state, specifically instability of the crystal structure and undesirable side reactions at the interface.[2] Additionally, the capacity of conventional layered oxides is reaching their theoretical value with recent developments in Ni-rich layered oxides, and further innovation beyond TM-redox as traditionally pursued in cathode materials is required to reach ever higher energy density as demanded.[3] In this context, harnessing the oxygen of the oxide as an additional redox center is attractive because addition capacity can be extracted in the same class of materials by changing only the electrochemical parameters of the reaction. The utilization of oxygen redox for lithium/electron storage in Li-rich cathode materials has been actively investigated from early 2010s, and is now one of the main research directions in the development of future cathode materials. The foci of this topic are not only in realizing stable oxygen redox for charge storage, but also to understand the intriguing phenomenon of how oxygen is oxidized during redox reactions in the cathode. Unlike the TM redox reaction, the oxygen redox reaction often triggers complicated electrochemical properties, so the practical realization is tightly coupled with the fundamental understanding. It is important to note that, in the early years when the capacity contribution of O was first proposed in 1999, limitation in experimental techniques and absence of theoretical framework prevented researchers from making concrete conclusions regarding this phenomenon.[4] However, with recent development of more sophisticated analytical techniques targeting the study of oxygen redox, we can now reevaluate our current understanding of how cathode materials degrade over cycling from a mechanistic perspective and even uncover new findings that were previously inaccessible due to experimental limitations. Most of the studies on oxygen redox reactions focus on Li-rich cathode materials with the stoichiometry $Li_{1+x}TM_{1-x}O_2$, however, with the development of modern advanced

3

characterizations, traditional LiTMO$_2$ such as LiNi$_x$Co$_y$Mn$_{1-x-y}$O$_2$ (NCM) and LiNiO$_2$ (NLO) have also been found to have oxygen redox at high potentials.[3h, 5] At this time, the fundamental mechanism of oxygen redox reaction remains a highly debated topics with contraversial discussions, it is thus critical to develop a more comprehensive understanding of the underlying issues hindering further improvement in battery performance for both traditional and state-of-the-art cathode materials.

To date, many strategies employed for enhancing the battery performance of LiTMO$_2$ were also found to be transferable to Li-rich cathode compounds, a generalization that was rationalized on the basis of the structural similarity of these two classes of materials. A general consent in battery field is that the oxygen oxidation process is associated with structure instability and parasitic interfacial reactions;[2f, 6] however, of oxygen redox reactions could be stablized with high reversibility, it could enhance the battery performance with high capacity and/or energy density.[7] Therefore, it is a good motivation to revisit the recent innovative strategies in oxygen redox point of view and review its effect to the performance of Li-rich cathodes and highly delithiated LiTMO$_2$. In this review, we introduce the current understanding of oxygen redox first, addressing their mechanistic aspects and consequences for battery performance. We then discuss various strategies from the atomic to microstructure scale for improving the battery performance based on oxygen redox reactions while mitigating the detrimental effects.

2. Oxygen redox in layered oxide cathode materials

2.1.   A recent history about the origin of oxygen redox based on Li-rich cathodes

Even though the oxygen redox activities in cathode materials have expected from early stage of cathode developments, oxygen was not considered as an important reversible redox center

until early 2010s. In the middle of 2010s, Tarascon et al., with many other researchers, ignited the fevent studies on the utilization of oxygen redox by showing the possibility of reversible oxygen redox with lithium-rich layered oxide cathodes.[3a, 3d, 8]

The first model used to study the oxygen redox mechanism by Tarascon group was the Li_2TMO_3 rock-salt structure and their analogues as the Li_2TMO_3 rock-salt structure takes advantage to show the oxygen redox activities in the cathode materials.[8b, 8c, 8f, 8g, 9] There have been studies by Thackery et al. from the 1990s to reveal the insertion/extraction mechanism of the cathodes which containing electrochemically inactive Li_2MnO_3.[10] The electrochemical inactiviy have been attributed from the instability of highly oxidized cations as the formal charge of the cation in this system is 4+. However, the Li-rich cathodes show the extraction of the excess lithium in the Li_2MnO_3, therefore, and the oxidation of oxygen was naturally expected in the viewpoint of the charge compensation. Because the reversible redox of lattice oxygen was away from the conventional idea, a lot of endeavors were triggered to find the systems which have reversible oxygen.

The early trials to enhance the reversibility of oxygen redox were exchanging Mn with heavy elements like 4d or 5d metals. As shown in the **Figure 1b and 1c**, more Li was extracted from the $Li_2Ru_xM_{1-x}O_3$ than that of Li-stoichiometric cathode materials, oxygen was attributed to the charge compensation for the further Li extraction. Experimentally, the oxidation behavior of oxygen was characterized through the comprehensive analyses including EPR, XPS, the short and long oxygen pairs were reported to support their model of oxygen dimerization towards peroxo-like species in the $Li_2Ir_xSn_{1-x}O_3$. Later, the peroxo-like structure in Li_2IrO_3 was reported through transmission electron microscopy (TEM) observations and neutron powder diffraction (NPD). The authors showed a bond distance of $(O_2)^{n-}$ pair

5

decreasing to ~2.4 Å after 75 % of Li ions are extracted, and the oxygen is ~2.7 Å far away from another oxygen which is not dimerized with it.[8g]
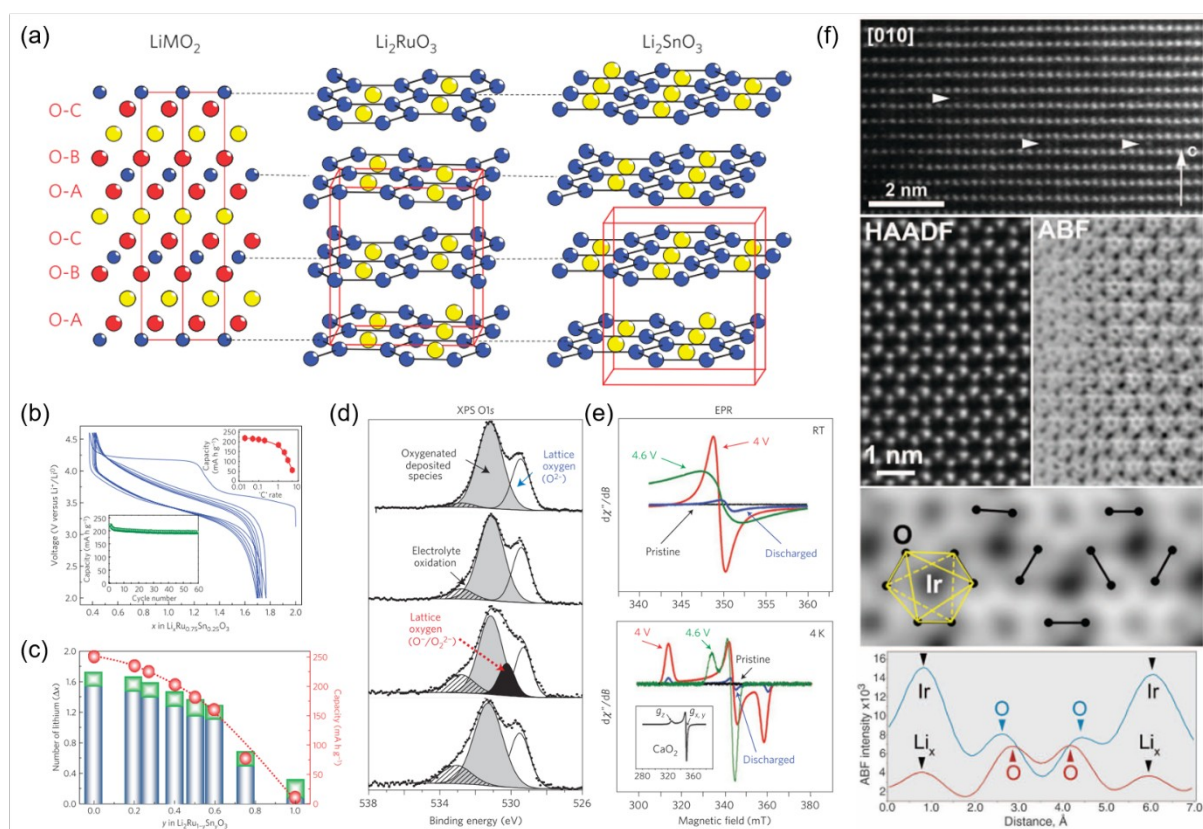

Figure 1. (a) Structure models of LiMO$_2$, Li$_2$RuO$_3$, Li$_2$SnO$_3$. The yellow, red and blue dots indicate the Li, O and TM atoms respectively. (b) The voltage profile of Li$_2$Ru$_{0.75}$Sn$_{0.25}$O$_3$, and (c) their reversible (blue) and irreversible (green) capacities depending on the amount of Sn. (d) O 1s XPS results showing the additional peak at ~531.6 eV regarding oxidized oxygen on their surface region, and (e) X-band EPR spectra showing the existence of peroxo-like species in Li$_2$Ru$_{0.75}$Sn$_{0.25}$O$_3$. Reproduced with permission.[8c] Copyright 2013, Springer Nature. (f) Transmission electron microscopy results of Li$_{0.5}$IrO$_3$ showing the distortion of IrO$_6$ octahedra. Adapted with permission.[8g] Copyrights 2015, American Association for the Advancement of Science.

Doublet et al. suggested the reductive coupling mechanism to rationalize the formation of peroxo-like $(O_2)^{n-}$ species as shown in the **Figure 2**. The main idea of reductive coupling is reconstruction of band structure through the change to metastable structure which allows the charge transfer from oxygen to TM. When the more than half of Li ions are delithated from the Li_2RuO_3, the octahedral structure of RuO_6 is significantly distorted to form short oxygen pairs as shown in **Figure 2b**.[8c, 11] Li_2MnO_3, which has highly ionic bond and thought to show the irreversible oxygen redox, was used as a control group to show the effect of covalency to the reversibility of oxygen redox. While the highly covalent Ru-O bond forms O-O intralayer bonds preventing the short O-O interlayer bonds, the lesser covalent Mn-O allows the O_2 elimination process by the formation of short O-O interlayer bonds as shown in **Figure 3**. The formation of intralayer O dimer was also observed in other systems, rationalized the stable oxygen behavior in those systems.[9d, 12] The interesting point of the reductive coupling is that the scenario covers the change of band structure during the charging process and it also rationalizes the unexpected reduction of Ru at the highly delithiated state. As Sathiya et al. reported in above Ru containing oxide works, Ru shows the reduction behavior in middle of charging process which is not expected in the conventional band structure model. The reduction of Ru is explained by the reorganization of O networks, which induces the charge transfer from O to Ru.
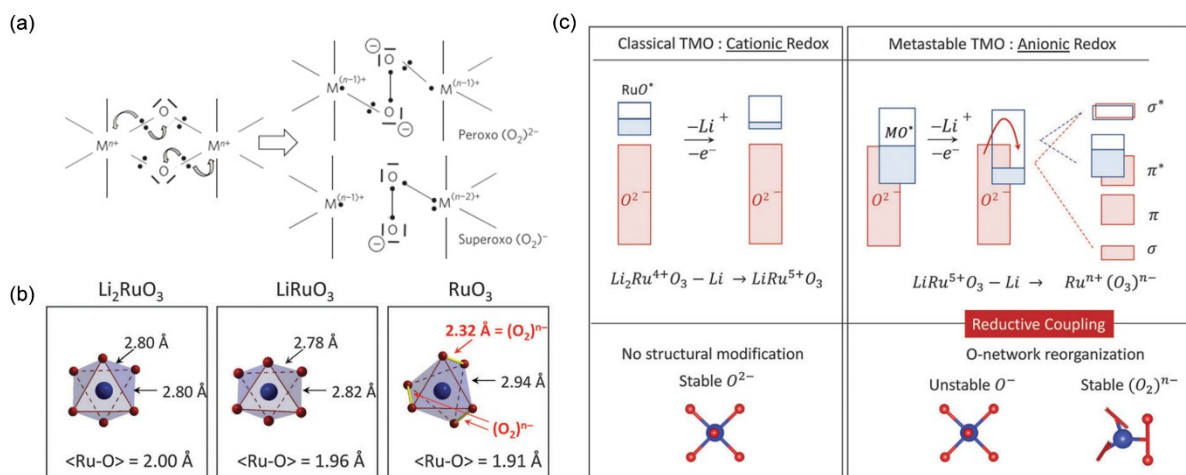
Figure 2. (a) The reductive coupling mechanism of two oxo-ligands coordinated to the TM in $Li_2Ru_xSn_{1-x}O_3$. Adapted with permission.[8c] Copyright 2013, Springer Nature. (b) A distortion of RuO_6 octahedra depending on the contents of Li ion. (c) A schematic diagram for electronic structures for cationic and anionic redox, the electronic structure was rearranged through the reductive coupling during the anionic redox process. Reproduced with permission.[11] Copyright 2016, Royal Society of Chemistry.
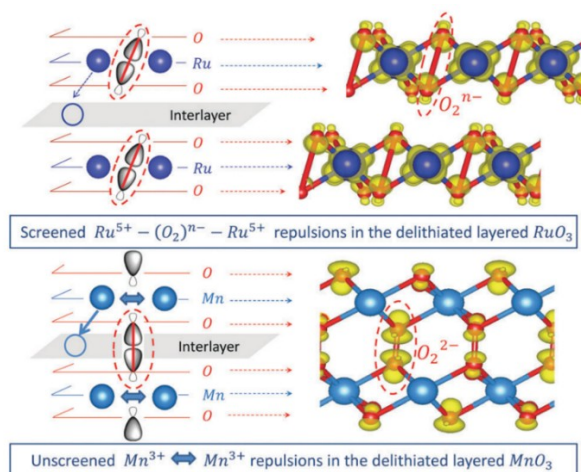
Figure 3. The different formation of O-O dimer due to the cation-cation electrostatic repulsion in metallic layer. Adapted with permission.[11] Copyright 2016, Royal Society of Chemistry.

However, the formation of peroxo-like structure was not universally accepted for understanding the oxidized oxygen states in cathode materials. In a later study, it was reported that the Li_2IrO_3 system that displays the oxygen dimmerization in the structural probes, as disscussed above,[8g] does not have oxygen redox reactions involved unless doped.[13] Luo et al. reported that $LiTMO_2$-Li_2MnO_3 (hereafter Li, Mn rich cathodes; LMR) cathodes composed with 3d transition metals do not form a peroxide species, because they did not find the corresponding signals in their results of Raman spectroscopy[8l, 8m], which is highly sensitive to the vibration of peroxide species $(O_2)^{2-}$ having bond length of ~1.45 Å.[14] Although without the signature of the peroxo- species, Luo et al. reported that the O-K X-ray absorption spectroscopy (XAS) pre-edge intensity varied upon cycling, indicating the oxygen redox reaction in LMR cathodes. While the XAS pre-edge intensity was later clarified as just a results of TM-O hybridization changes, as elaborated later, this work triggered a great number of interest for revisiting LMR materials with the oxygen redox concept. We note that this work also displays several spectra from resonant inelastic X-ray scattering (RIXS) that shows some changes on the lineshape with unclear mechanism, which will also be discussed later in this review. Very recently, the group has used high resolution RIXS with the focus on the low-energy excitation signals from the vibronic modes and reported that the oxdized oxygen is realized by O_2 molecules trapped in the materials.[7c]

Seo et al. proposed an explanation the formation of the band based on the DFT calculation as shown in **Figure 4d**.[3d] The case studies for various Li-O-Li environments from Li_2MnO_3 analogues to disordered rock-salt (DRX) cathodes suggested that Li-O-Li arrangement give rise to the labile oxygen electrons that participate in the redox activity. The paper explains why the arrangement can provide a band lied near the Fermi level. Unlike the Li-stoichiometric cathode materials, an 'orphaned unhybridized O 2p states' can be occurred

9

through the Li-O-Li configurations in Li-excess materials due to the energy difference

between Li 2s and O 2p. Therefore, the energy level of Li-O-Li state is similar with the one

of unhybridized O 2p orbital, the oxygen can be oxidized through the labile Li-O-Li state.

Theoretical works by Okubo et al. proposed an approach based on the structure symmetry

that the electronic state is π-type less-antibonding (b1*) orbital arose from the C_{2v} symmetry

of OM_2Li_4 octahedra consisted of 4 Li ions and 2 TM ions as illustrated in **Figure 4c**.[15]
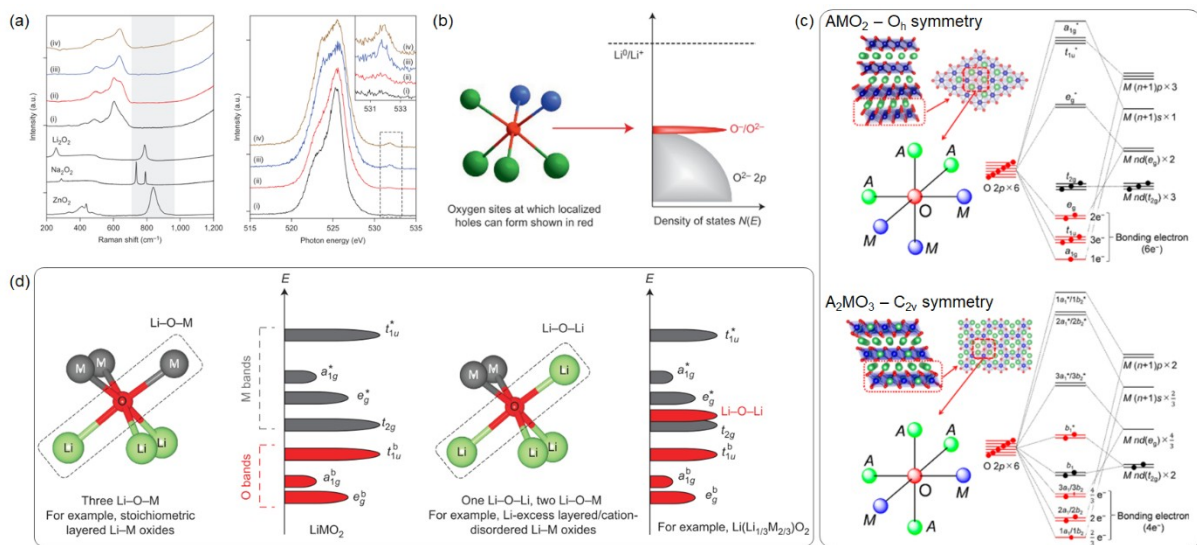
Figure 4. (a) Raman and RIXS spectra of LMR during the charging process, and (b)

presumed O 2p lone pair state from (a). Reproduced with permission.[8m] Copyright 2016,

American Chemical Society. (c) Molecular orbital diagrams for AMO_2 (O_h symmetry) and

A_2MO_3 (C_{2v} symmetry). Reproduced with permission.[15] Copyright 2016, American

Chemical Society. (d) The schematic diagrams of electronic structure for $LiMO_2$ and

$Li(Li_{1/3}M_{2/3})O_2$, which show the Li-O-Li arrangement induced O state. Reproduced with

permission.[3d] Copyright 2016, Springer Nature.

At present, the model of oxygen oxidation based on the Li-O-Li configuration is probably the most popular for understanding the oxygen redox reaction in Li-rich compounds. The Li-O-Li perspective is different from the one based on peroxo-like species through reductive coupling. One important difference between two theories is whether the configuration of Li-O-M stabilizes the O-O bonding. The calculation from Seo et al. suggests that the Li-O-Sn configuration does not stabilize the O-O bonding but rather byproduct of the σ bonding between Li-O-Li states, unlike the Sathiya et al. insisted that unchanged hybridization of Sn^{4+} can prevent the condensation of O_2.[3d, 8c] According to Seo's explanation, the oxygen redox in $Li_2Ru_xM_{1-x}O_3$ attribute to the Li-O-Li state and the peroxo-like formation is a byproduct of oxygen redox. Doublet et al. also suggested the similar mechanism for O-O σ formation, but the hybridization between O-Ru stabilizes the O-O and the difference between Ru and 3d metals including Mn is arisen from the difference of covalency.

Besides, Seo et al. suggested that the formation of peroxo-like species depends on the character of metal and it needs some prerequisites to explain the formation only limited few cathode compositions. To form O-O bonds, the Li-O-Li states should be neighbored, and the states should not loss much hybridization character with transition metals. According to this explanation, the O-O formation occurs through the little rotation of unhybridized O 2p orbital, therefore, the highly directional TM-O (2p) hybridization is not favorable to make the peroxo-like species. Instead, d-electron filled Sn^{4+} could be more flexible so that preferable to form the O-O. However, the explanation does not include the relationship between O-O and heavy transition metals such as Ru and Ir containing oxide.
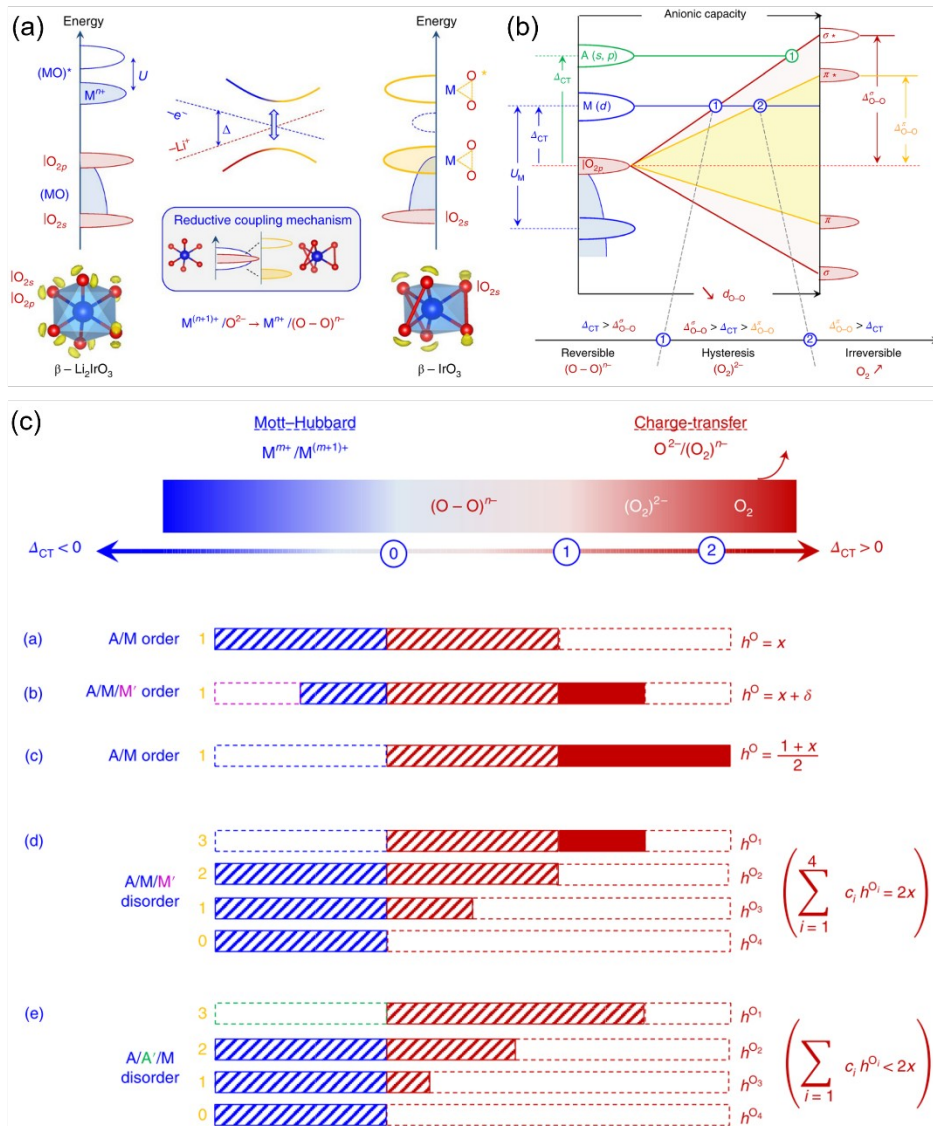
Figure 5. The reorganization of electronic structures of (a) Mott-Hubbard cathodes and (b) Charge-transfer cathodes. (c) A unified picture of oxygen redox in alkali-rich cathode materials. Reproduced with permission.[16] Copyright 2019, Springer Nature.

Hong et al. tried to define the oxygen redox with the concept of the 'formal charge' through the case of doped Li_2IrO_3, which is known to form peroxo-species.[13] By the help of bulk sensitive X-ray techniques, hard X-ray absorption spectroscopy (hXAS) and scanning transmission X-ray microscopy (STXM), they observed the oxidation trend of Ir and O with more reliable methods. The oxidation of Ir showed a monotonic behavior even until the 75 %

of Ir was extracted from Li_2IrO_3, which have not observed in other cathodes which utilize the TM unhybridzed oxygen redox. Furthermore, the RIXS results showed no feature of the oxygen oxidation, even Li_2IrO_3 has a lot Li-O-Li arrangement inside. The large energy gap between Ir 5d-O 2p and Li-O-Li states prevented the competition between hybridized and unhybridized oxygen redox. It means that the oxygen of Li_2IrO_3 is involved in the cycling only through the hybridized TM-O states, which should be considered as a typical 'cationic redox' behavior in conventional materials.

To understand what determines the difference of the redox process, many studies conducted including the report from Yahia et al.[16] In 2019, Yahia et al. proposed a unified picture based on the electron localization function (ELF) calculation, and expected properties of cathodes based on physical parameter of materials such as charge-transfer energy (Δ_{CT}), d-electron Coulombic interaction (U) and O-O discrete energies (Δ_{O-O}). The cathodes are classified to two groups, charge-transfer regime and Mott-Hubbard regime, depending on their electronic structure. As shown in **Figure 5a**, the Mott-Hubbard cathodes retain their oxygen dimer structure stable through the reductive coupling. Due to the instability of O lone pair hole, the structure was distorted by removing the degeneration of states which inducing the M-(O-O) formation. On the other hand, the peroxide formation in charge-transfer cathodes are not always stable, the stability depends on the relative energy level between Δ_{CT} and Δ_{O-O} as plotted in **Figure 5b**. The O dimer is stable if the $\Delta_{CT} > \Delta_{O-O}$, it will lead O_2 gas evolution or hysteresis in the material for other cases. In addition to this classification, the number of O 2p lone pair holes were calculated based on the stoichiometry of materials and plotted together with energies to expect the stability of peroxides as shown in **Figure 5c**. The number of O hole per TM is known to determine the stability of O redox, the expectation looks consistent with the reported results.[7c, 17]

2.2. The challenge on defining the oxygen redox

The "Cationic redox" has been used to explain the redox reactiosn in the conventional operation range of cathode materials, especially the Li-stoichiometric oxide materials such as $LiCoO_2$, $Li[Ni_xCo_yMn_{1-x-y}]O_2$. In these systems and in the conventional potential range, the O is only involved through the TM-O hybridizatin that always exists for TM oxides. TMs are dominantly in charge of that state due to energy level difference between TM 3d and O 2p. The changes in the materials well elaborated by valence change of cations, charges of O could be observed through spectroscopic features of TM-O hybridization in all cathode systems.[18] In this context, the intrinsic O redox reaction should be differentiated from the oxygen involvement through the universally existing hybridization effect. The "anionic redox" should thus be defined as an oxygen state that is indeed oxidized not only through the TM-O hybrdization. A natural model is the unhybridized O redox state that shows distinct physical and chemical properties from TM redox behavior. More specifically, in many works, the oxygen redox activity is often considered to take place on the non-bonding electrons in the 2p orbital of oxygen, as Doublet et al. suggested.[3e, 16] This deductive way to define the oxygen redox has not been resistive so far even it is not always true. However, this remains an actively debated topic and a variety of oxidized oxygen states and their transformations such as O-O dimerization have been reported, as discussed in the last section.
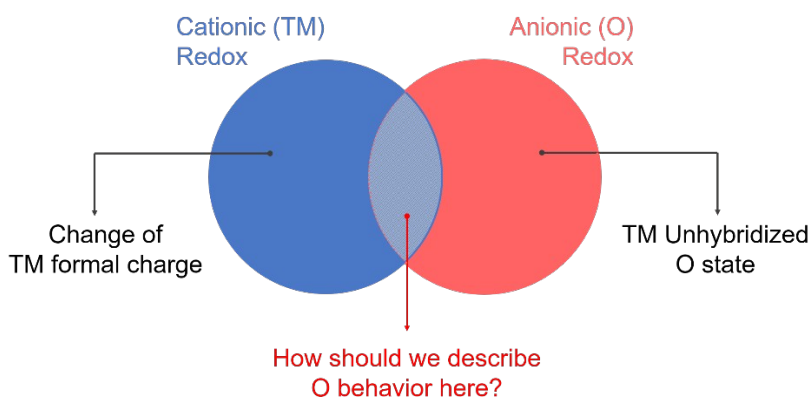
Figure 6. A schematic showing the debate on the definition of oxygen redox. Blue circle and red circle indicate the TM redox and unhybridized O redox, respectively. The shaded area indicates the oxygen states that also vary upon electroehcmical cycling but associated with TM-O hybridization.

Recently, Gent et al. have insisted a necessity of a contemporary definition of oxygen redox, and suggested prerequisites of oxygen redox in their work.[13, 19] According to their statement, formation of any oxidized species in the oxide such as O^{1-} (note that Greek character implies the formal charge), O-O < 1.5 Å, that does not require TM-O bonding should be considered the oxygen redox. On the other hand, the TM=O formation or O-O ~ 2.4 Å are considered as a result of stabilization by help of hybridization with transition metal or by structural distortion rather than the oxygen redox. The definition provides useful criteria to categorize the TM unhybridized oxygen redox from other type of oxygen activities, and the activities can be experimentally distinguished by resonant inelastic X-ray scattering (RIXS) technique. The debate on the definition of the oxygen redox persists as the discrepancy between the different models of oxygen redox mechanism remains a challenging topic until the fundamental mechanism of oxygen redox reactions could be clarified.

15

At least phenomenally, the definition of the oxygen redox should refer to a reaction that involves both oxydation and reduction, i.e., the "red-ox" reaction. Although there is very likely an association between the many irreversible oxygen oxidation reactions, e.g., gas release and surface reactions, and the reversible redox reaction, we suggest studies should clearly differentiate the mere oxygen oxidation from a practicable/reversible oxygen redox reaction.

Fundamentally, due to the elusive mechanism of oxygen redox reaction at this time, this review emphasizes the contradiction in the current studies and try to incorporate the different models by considering all the reported oxygen redox reactions that include any type of "reversible" oxidation and reduction reactions directly on O states, and the modifiers (e.g. (un)hybridized, short/long peroxide formation) describing the property of the redox are used to show which oxygen redox model we use in the context. As a matter of fact, a large number of publications on oxygen redox topics are still based on the results and analysis from TM-O hybridizations, which we believe should be differentiated from the modern definition of oxygen redox concept, however, the link between the two remains an open question. In **Figure 6**, we provide a naive schematic to illustrate the debate. At present, a holistic picture of the roles of the TM, the unhybridized O, and the hybridized TM-O states on the oxygen redox reaction in oxide systems remains missing, which strongly depends on the ultimate clarification of the fundamental mechanism of oxygen redox reactions and its association with TMs.

2.3. Spectroscopic techniques to probe the oxygen redox related phenomenon

The developments and improvements of modern synchrotron analyses empower the researchers to access unprecedented information. The discussion on the oxygen redox has

16

heavily benefited from these techniques. Although significant debates remain on the mechanism of the oxygen redox, the analyses flourish the discussion by providing more direct evidences on the oxygen states through spectroscopic tools. In this section, we briefly introduce the characterizations which provide the information about the oxygen chemistry involved in oxygen redox systems.
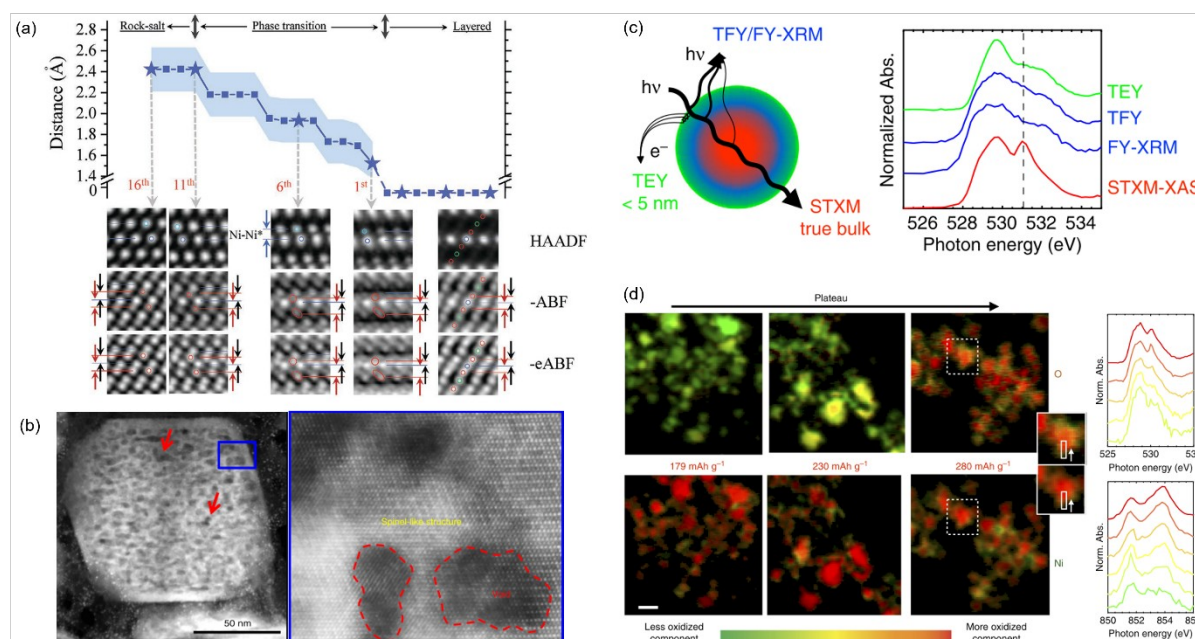
Figure 7. (a) enhanced annular bright-field (ABF) images during the charging process of LNO by scanning transmission electron microscopy (STEM). Reproduced with permission.[20] Copyright 2020, Wiley. (b) The TEM and STEM images indicate the occurrence of spinel transition and pores inside the LMR particle. Reproduced with permission.[21] Copyright 2019, Springer Nature. (c) A schematic of detection limits for detection modes, and spectra by different detection modes. (d) STXM images of LMR during the charge process. Reproduced with permission.[22] Copyright 2019, Springer Nature.

Structurally, electron microscopy has been widely employed for sub-angstrom atomic scale studies of battery materials. As shown in the **Figure 1f**, the abrasion-corrected scanning

transmission electron microscopy (STEM) detects the atom in the material.[8g] The high angle

annular dark-field (HAADF) and annular bright-field (ABF) imaging detects heavy ions and

light ions, respectively, to visualize the structure of the material. The formation of short and

long O-O pairs in the highly delithiated cathode was detected by the STEM, this has been one

of the most important experimental bases for the peroxo species with reductive coupling

mechanism. Lee et al. suggested that the directional cracking through the TEM and STEM,

the migration of oxygen vacancy in the bulk has a preference of facet.[23] The STEM results

from Yan et al. also support that the spinel phase and oxygen loss behavior in the bulk.[21]

Furthermore, the enhanced ABF (eABF) imaging by 4D STEM reported by Ahmed et al.

shed light on the better observation of light element such as oxygen.[20] The contrast between

HAADF and eABF clearly show the migration behavior of Ni in LNO, unexpected one-

directional Ni migration was observed through this method. Some part of results revealed by

the electron microscopies suggested above are contrast to the conventional idea that the phase

degradation and oxygen gas evolution starts from the surface region. Electron microscopies

reveal the novel structural evolution which is crucial to correctly understand the materials.

However, there are concerns about the damage by the beam as the ABF imaging needs high

flux of the beam due to its low efficiency, and whether the phenomenon is general through the

material. [24] Therefore, the experiments and data analyses must be carefully handled.

While the electron microscopies provide important information focusing on the atomic

position of the materials, Raman spectroscopy determines the oxygen redox by observing the

chemical resultant of the oxygen redox. As stated in Figure 4a, Raman spectroscopy show

specialty to characterize the oxygen dimer having the bond length of 1.45 Å even though

there are debates whether the oxygen dimer is general resultant of the oxygen redox.[8m] Qiao

et al. reported that the reversible occurence of peak around 900 cm^{-1} in highly desodiated region through the in-situ Raman spectroscopy, and Taylor et al. clarified the peak is assigned to the stretch mode of the peroxide bond in oxygen dimer by DFT calculation.[25] It is noteworthy that the peroxide peak happened or not in the same material e.g. $Li_{1.2}Ni_{0.2}Mn_{0.6}O_2$. The difference of the spectra is attributed to the probing region as the surface Raman signal can be enhanced by using the gold nanoparticles.[25a] Considering the difference depending on the probing depth, the peroxide peak of Raman spectra is possibly happened near the surface of $Li_{1.2}Ni_{0.2}Mn_{0.6}O_2$. According to the previous theory based on the reductive coupling mechanism, the intralayer peroxide formation as shown in Figure 3 can be one of the ways to interpret the reversible peak occurence of the Raman spectra. However, the reductive coupling is one of the theories to explain the oxygen redox and still remains controversy. Recently, House et al. insisted that the oxygen dimer formation in the $Na_xLi_yMn_{1-y}O_2$ is close to the molecular O_2 rather than the peroxide $(O_2)^{2-}$ based on the vibrational frequency extracted by the RIXS spectra.[7c] The claim from the report is contradictory with the theory that the formation of the peroxide is a stable state which is resulted from the oxygen redox. Thus, more detailed discussion must be followed to understand what the Raman peak stands for and to bring better insight regarding the resultant of oxygen redox.

While the electron microscopies provide important information focusing on the structure of the material, the soft X-ray spectroscopy (SXS) techniques are useful tools to characterize the chemical states, such as the electronic structure and the valence of ions. The energy range of soft X-ray covers the O K-edge and L-edge of *3d* TM, which correspond the excitations directly to the valence O-*2p* and TM-*3d* states,[18a] introducing the most directly probes for

19

detecting the chemical states and redox mechanism of electrode materials with both TM and O redox.

To discuss the oxygen redox behavior in transition metal oxide system, soft X-ray XAS (sXAS) and X-ray photoelectron spectroscopy (XPS) analyses of TM and O have been frequently employed to characterize their oxidation states.[8b, 8c, 8g, 8m, 26] The total electron yield (TEY) and total fluorescence yield (TFY) modes of sXAS have different probe depth of about 10 and 150-300 nm (photon energy dependent), respectively. It is important to note that, TFY signals of sXAS, although with deeper probe depth, suffer notorious lineshape distortion due to the so-called self-absorption effects.[18a] But it is known that such a distortion could be eliminated if sXAS could be collected in transmission modes. For example, Gent et al. used scanning transmission X-ray microscopy (STXM) method to reveal the TM and O states.[22] Several reports have used hard X-ray Photoelectron Spectroscopy (HAXPES) for same purpose, and the detection of signal from relatively bulk part is available due to the deep penetration of hard X-ray.[27] However, we note that the applications of both sXAS and HAXPES remains debated topics. For example, interpretations of XPS results towards oxidized oxygen species have been considered risky due to the limited probe depth even with hard X-rays.[28] Because the inelastic mean free path (IMFP) of the emitted electrons is few nanometers-short even at hard X-ray energy range, the spectra from electron detection mode contains surface dominated information.[29]

Studies on oxygen redox based on O-K sXAS have been focusing on the variations of the so-called pre-edge features upon battery cycling.[8m, 26] However, such variations are significantly affected by TM-O hybridization environment.[18a, 30] Indeed, even for the $LiFePO_4$ system without any oxygen redox reaction, a strong pre-edge variation could be observed during the

delithiation process (**Figure 8a**), leading to the serious concern on using O-K sXAS for

detecting the oxygen redox states.[18b] Unfortunately, characteristic features of the oxidized

oxygen states, e.g., peroxides and O_2 gas, fall into the same energy range as the pre-edge

features in TM oxides.[31] Therefore, to distinguish the intrinsic oxygen redox states from the

dominating TM-O hybridization becomes critical. This technical challenge has led to the

significant efforts on developing the ultra-high effeciency mapping of RIXS (mRIXS).[18a, 32]

As shown in **Figure 8b**, mRIXS covers the full energy range of the sXAS on excitation

energies, however, detects a new dimension of information on the emission energy of the

outcoming fluorescence signals, which enables the distinction of the oxygen redox feature

from the dominaing TM-O signals as demonstrated in both Li-ion and Na-ion battery

systems.[33]
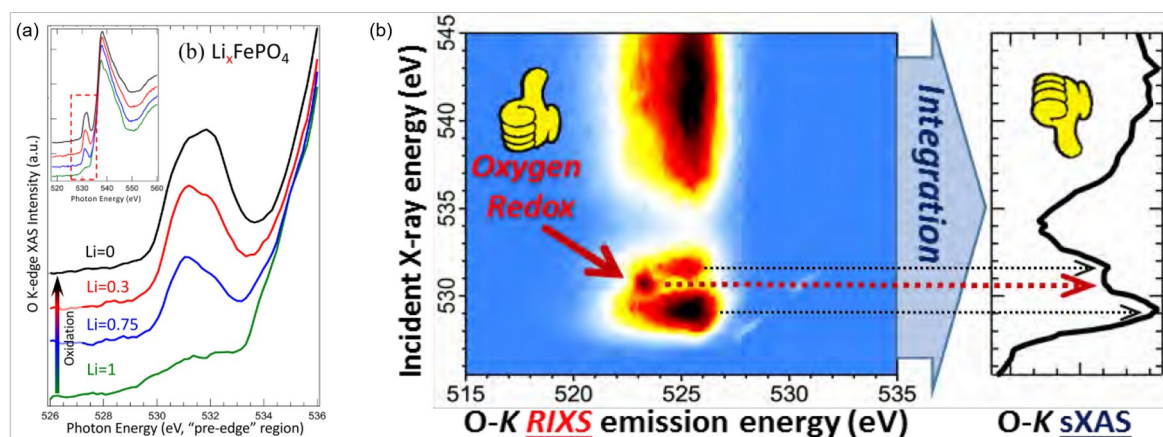
Figure 8. (a) The pre-edge region of O-K edge from Li_xFePO_4 depending on their Li

concentration. Reproduced with permission.[18b] Copyright 2020, Wiley. (b) A schematic of

O-K edge RIXS mapping that resolves the spectra as the functions of incident energy and

emission energy. Reproduced with permission.[18a] Copyright 2018, Elsevier.

RIXS is a photon hungry experiment, which triggers the concern on irradiation damage.

Experimental results show that the oxidized oxygen feature could be eliminated by too much

X-ray radiation, indicating the importance of high-effeciency RIXS experiements and also the validity of the RIXS probe as it could at worst underestimate the oxidized oxygen state.[26c] At present, mRIXS has been established as a crucial tool for characterizing various systems with oxygen redox reactions, with several examples shown in **Figure 9a**.[19] A recent study also indicates that the oxidized oxygen state in the oxide cathodes displays distinct patterns in the full-range mRIXS results from the molecular systems of peroxides and O_2 (**Figure 9b**).[31] Therefore, the fingerprinting feature from the mRIXS can be useful indicator to determine the existence of the oxygen redox. For example, recent study from Jatinkumar et al. claimed based on the RIXS feature that there is no oxygen redox in the Li_2MnO_3, which is an early target material to understand the oxygen redox. They suggested the carbonate formation/deformation happens at the surface of Li_2MnO_3 instead of the oxygen redox in the bulk.

However, it is important to note that the fundamental understanding of the fingerprinting mRIXS feature emphasized in these studies, around 531 eV excitation and 523.7 eV emmission energies, remains unclear. Additionally, recent studies of high-resolution RIXS focus on different part of the low-energy excitation features,[34] which point towards a trapped O_2 gas model of the oxidized oxygen.[7c] Therefore, as the most direct and sensitive probe of the oxygen redox states in oxide cathodes, there is still a keen need of the intepretation of the mRIXS features through future theoretical and experimental works.
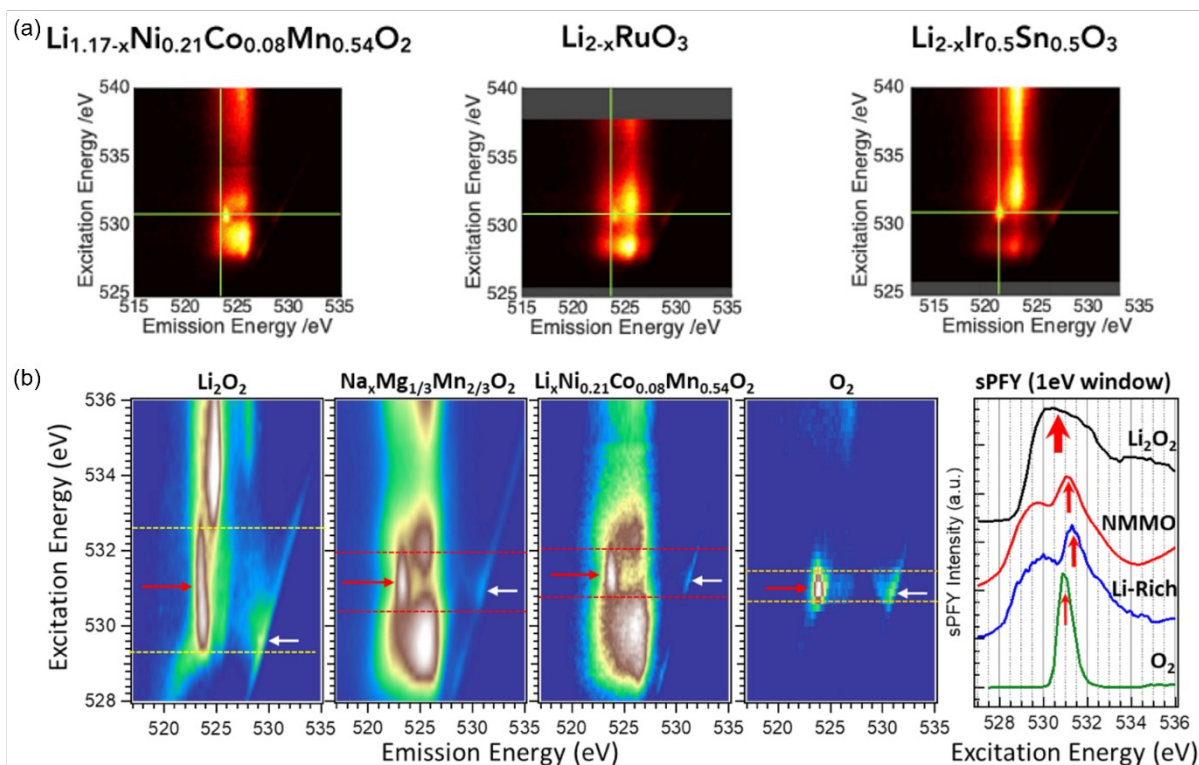
Figure 9. (a) The mRIXS spectra of $Li_{1.17-x}Ni_{0.21}Co_{0.08}Mn_{0.54}O_2$, $Li_{2-x}RuO_3$ and $Li_{2-x}Ir_{0.5}Sn_{0.5}O_3$. The crosshair indicates the energy level of RIXS features. Reproduced with permission.[19] Copyrights 2020, Cell Press. (b) The comparison of mRIXS spectra between cathodes, peroxide, and O_2. The sPFY spectra were extracted from mRIXS maps by integrating the intensity within 0.5 eV of 523.7 eV emission energy. Reproduced with permission.[31a] Copyright 2020, American Chemical Society.

2.4. Myths on the relationship between oxygen redox and simultaneous phenomena happen in high voltage region

Various phenomena happen during the redox of cathode materials, and the phenomena such as transition metal migration, voltage hysteresis, oxygen evolution usually get severe along to the degree of delithiation. As the contribution of oxygen redox in charge compensation increases at the high voltage region where the phenomena happen simultaneously. Therefore, the oxygen redox has been deductively considered as one of the major causes for the

phenomena. However, the effect of oxygen redox to the phenomena remains elusive. The conclusive decoupling is almost impossible due to the complexity of the redox chemistry. In this case, suggesting disproofs of the myths can be useful and direct way to decouple them. Here we summarize the works that emphasize the coupling of oxygen redox and these phenomena, as well as other contraversal reports.

2.4.1 Oxygen redox and transition metal migration

The transition metal migration from TM-O slab to alkali metal slab is known to major degradation factor of layered oxide cathodes from the early stage of cathode studies. The TMs in Li slab not only deteriorate the movement of alkali ions but also lower the capacity by increasing the number of immobile alkali ions. Especially, the densification mechanism that migrating the transition metals from the surface to the bulk is believed to responsible for major degradation pathway of Li-rich cathode materials. The densification of TM is simultaneously observed with the evolution of O_2 gas, they are likely to correlated each other. However, it has been not fundamentally understood that the oxygen redox leads the densification so far, vice versa.
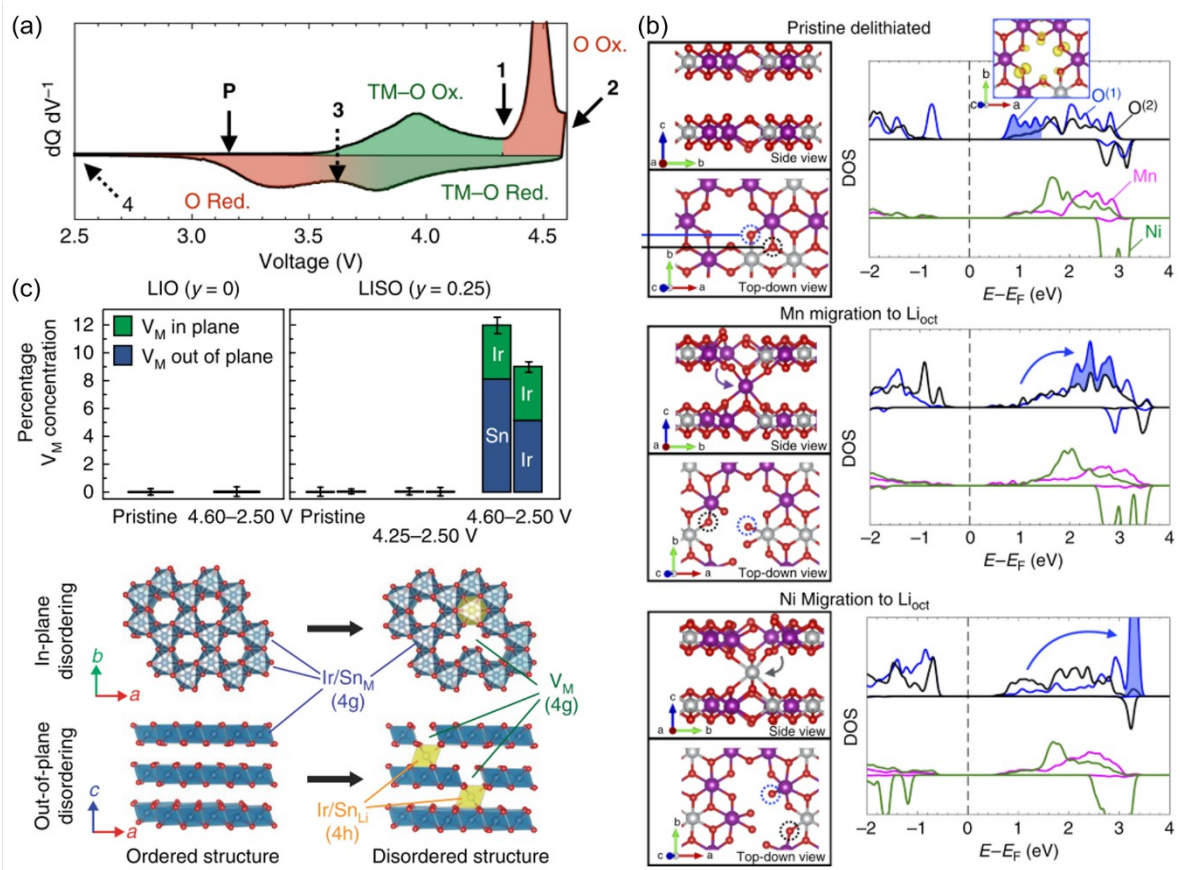
Figure 10. (a) The cyclic voltammetry result of LMR, and the sequence of TM and O redox were reversed after initial charging process. (b) DOS calculation results considering the migration of TM to octahedral site in Li slab. Reproduced with permission.[22] Copyright 2017, Springer Nature. (c) TM migration behaviors in IRSO. Reproduced with permission.[13] Copyright 2019, Springer Nature.

Gent et al. insisted the oxygen redox necessarily induce the oxygen redox by changing the electronic structure of cathode after charging process.[22] The bulk detective TXM revealed the detailed redox sequence as illustrated in the **Figure 10a**. TM participate to the charge compensation first and O follows during charging process. Interestingly, the sequence of TM and O redox was inversed when the cathode is under discharging process while the redox below 4.35 V where unhybridized O does not participate shows symmetric redox curve.

Therefore, it implies some changes in electronic structure after the cathode was charged to 4.6 V when the unhybridized O participates. As the static localized O 2p band model cannot explain the dynamic behavior of band structure alone, they employed transition metal migrated model for the DFT calculation.[3d, 15] When the migrated Ni and Mn occupy the octahedral site in Li slab neighboring the TM vacancy, the O 2p band bonded with two TM significantly shift to higher energy level as shown in **Figure 10b**. For this point, Wei et al. also investigated about the densification in similar system of $Li_{1.2}Ni_{0.13}Co_{0.13}Mn_{0.54}O_2$, and insisted that Mn has higher possibility to occupy the octahedral site than other TMs (Ni and Co) based on the neutron/X-ray diffraction results.[35] Due to the lifted energy level of O non-bonding band, the band is filled after the TM-O hybridized band is filled during discharging process. Finally, the alternative notation for oxygen redox was suggested; $[O^{2-} + TM] \rightarrow [O^- + TM_{mig}] + e^-$.

Hong et al. further developed the oxygen redox-defect coupling mechanism in their following work with $Li_2Ir_{1-x}Sn_xO_3$.[13] While the Li_2IrO_3 (LIO) does not show the unhybridized oxygen redox even their high amount of Li-O-Li states, Sn doping in $Li_2Ir_{1-x}Sn_xO_3$ (LISO) induces the redox of unhybridized oxygen states. When the concentration of Sn increases, the amount of TM vacancy (denoted to V_M) increases with the migration of Sn into Li (denoted to Sn_{Li}) slab as shown in **Figure 10c**. The formation of Sn_{Li}-V_M is energetically more favorable than the Ir_{Li}-V_M, and significantly stabilize the structure. As a result, the Sn_{Li}-V_M results the Ir=O and Sn-(O-O) where Sn anchored to oxygen dimer having ~1.44 Å of bond length. It is noteworthy that the oxygen dimer is not same with the one in LIO having ~2.4 Å of long distance between two oxygens. The short O-O dimers that usually observed in LMR can be considered to have a bond due to their short bond length like other peroxide species, and only formed when the migration of metal happens, which have differentiated characters from the

long O-O dimer. According to the spectroscopic analyses, these large difference in structural evolution between LIO and LISO arises from the oxidation of Ir in LISO over 5.5+. Beyond 5.5+, Ir=O bond is formed by the strong covalency of Ir-O bond inducing the ligand to charge transfer (LMCT) from O to TM. Consequently, the LMCT is more stabilized by structural evolution, and short O-O formation near the $Sn_{Li}-V_M$ is led by the substantial amount of LMCT. The theory suggests the dynamic change of the electronic structure is cooperative process between the oxygen redox and TM migration, and the formation of antisite-vacancy is originated by oxygen redox or high-valent cationic redox unlike conventional insight that the defect attributes to the structural instability.

The TM migration-oxygen redox coupling theory well rationalizes that the unhybridized oxygen redox can be a driving force for TM migration. However, we face a big dilemma about the practicality of oxygen redox if it always accompanies the TM migration. Eum et al. answers the problem with O2-phase $Li_x(Li_{0.2}Ni_{0.2}Mn_{0.6})O_2$ (O2-LLNMO) which shows reversible TM migration with the unhybridized oxygen redox activity.[7a] The structure of O2-LLNMO has unique sharing structure that the O_h sites in Li slab and TM slab share their faces while they share their edges in O3 structure. The structure was derived from the Na-layered oxides which shows better oxygen redox reversibility than Li-layered oxides, and the reversibility of the structure was rationalized by a viewpoint of cation repulsion here.[36] The unique sharing structure makes a large energy barrier of TM migration to O_h site in Li slab due to electric repulsion between TMs. Therefore, the TM migration was limited to the tetrahedral site and return to their original site when the cathode was discharged as shown in **Figure 11a**. In addition, the flip of electronic states by decoordination of TM, reported by Gent et al., was not observed in this material, which suggests reversible migration behavior of TM as shown in **Figure 11b**.
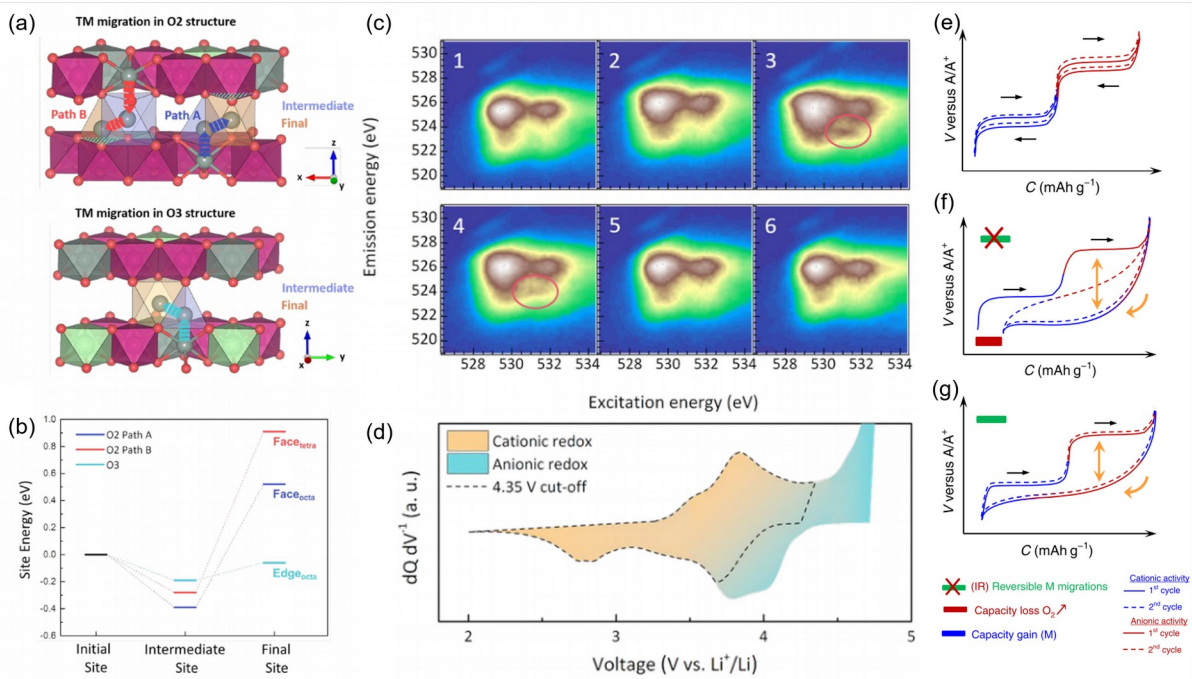
Figure 11. (a) TM migration pathways of O2 and O3-LLNMO structure, and (b) the calculation result for each site energy. (c) mRIXS result through the initial cycle and red circle in 3 indicates the RIXS feature due to oxygen redox. (d) CV result for first cycle of O3-LLNMO, and the sequence of TM and O redox was not reversed during the cycling. Reproduced with permission.[7a] Copyright 2020, Springer Nature. (e-f) Schematic galvanic curves of alkali-rich cathodes. Reproduced with permission.[16] Copyright 2019, Springer Nature.

In general, the studies on this topic suggest that the TM migration, although strongly coupled to oxygen redox when it takes place, can be prevented by the material modification in oxygen redox systems. However, we note that the discussions on the mechanism remain controversial even for very similar materials, further studies are needed to unify the models with underlying mechanism and to reveal the intriguing correlation between the cation migration and oxygen redox reactions.

2.4.2 Oxygen redox and voltage hysteresis

The voltage hysteresis of layered oxides has been observed in almost of cathodes utilizing oxygen redox and considered to one of the thresholds for practical utilization of oxygen redox.[37] The oxygen redox has thus been considered to be almost inherent to the voltage hysteresis. As we discussed through part 2.4.1, other than the cation migration that was considered as an important factor leading to hysteresis,[13, 22] another major factor is believed to be the layered-to-spinel transition correlated with the densification of the surface. Recent studies support the scenario that the structural reorganization lead the voltage fade and hysteresis based on experimental evidences such as STEM, XRD, Raman, thermometry, 3D tomography, etc.[8n, 9d, 27, 37-38] Therefore, the several works insisted that oxygen redox induces the voltage hysteresis through the structural reorganization. However, the key prerequisite of this theory is oxygen redox must involve the TM migration resulting phase transition. As we discussed above, oxygen redox can provide the driving force for the migration, and part of oxygen drives oxygen loss through irreversible oxidation. However, the reversible oxygen redox does not necessarily introduce the detremental effects. In another words, the voltage hysteresis associated with the structural reorganization may not be directly caused by oxygen redox reaction itself. Indeed, a recent study shows that, $Na_{2/3}Ni_{1/3}Mn_{2/3}O_2$ displays very strong oxygen redox behaviors but with negligible voltage hyesteresis and highly reversible electrochemical profile.[39]

2.4.3 Oxygen redox and oxygen loss

The oxidation process in oxygen redox produces highly electronegative elements so that makes a lot of unwanted reactions such as oxygen gas evolution or electrolyte decomposition. [38a] Besides, the densification of surface accompanies the loss of oxygen and its propagating

behavior which makes continuous oxygen loss in some materials.[3f] For this reason, it is easy to be confused that the oxygen redox is a process causing the oxygen loss of materials. However, as we discussed in the definition of oxygen redox, we must distinguish the irreversible oxygen oxidation and reversible oxygen redox processes. Every oxygen atom does not have same chemical or structural environment, they make different results once they oxidized. Therefore, the key discussion of this part should be whether the oxygen redox is intrinsically irreversible process resulting the oxygen loss of cathodes or the loss of oxygen is arising from the irreversible oxygen oxidation.
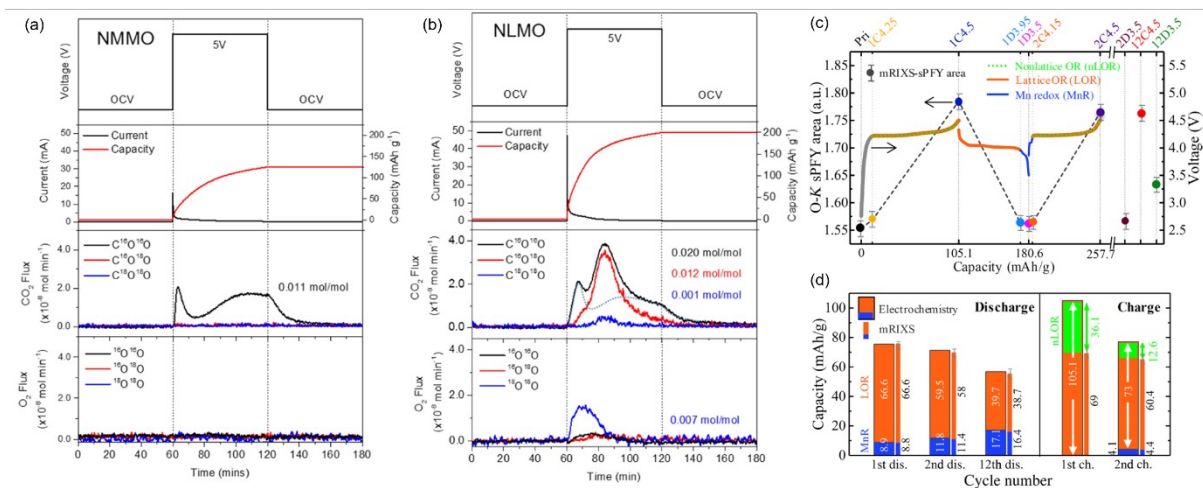
Figure 12. OEMS results of (a) NMMO and (b) NLMO. The black, red and blue lines regard to $^{16}O^{16}O$, $^{16}O^{18}O$ and $^{18}O^{18}O$, respectively. Reproduced with permission.[26b] Copyright 2019, (c) The redox map of NLMO based on the quantified spectroscopies including sXAS and sPFY-RIXS. (d) The charge contribution analysis of NLMO. Reproduced with permission.[7b] Copyright 2020, American Association for the Advancement of Science.

As the experimental characterization shows the result of two type of oxygens together, distinguishing the two oxygen is barely possible in general. However, P2-$Na_{0.67}[Mg_{0.28}Mn_{0.72}]O_2$ (NMMO), which has the unique redox property that shows no oxygen

gas evolution and purely depends on the oxygen redox, helps the distinguishing two oxygen properties.[7b, 26b] The NMMO and $Na_{0.78}[Li_{0.25}Mn_{0.75}]O_2$ (NLMO) have Mg and Li in their octahedral site of TM slab, and the overall structures have high similarity except their stacking. House et al. compared the OEMS results of two materials, and the results shows impressive difference in gas evolution behavior. The NMMO and NLMO used in the OEMS analyses was sintered in $^{18}O_2$ gas, the isotope of $^{16}O_2$, to replace the ^{16}O at the surface of cathodes to ^{18}O. Therefore, the detected gas allows to find the origin of oxygen is the electrolyte or the surface of materials. As shown in **Figure 12a**, detected CO_2 gas from NMMO cell only includes ^{16}O while the NLMO shows all combination of ^{16}O and ^{18}O, which indicates the surface oxygen of NMMO does not participate to form CO_2 evolution while the surface oxygen of NLMO did. Furthermore, NMMO shows no O_2 evolution while the NLMO show O_2 evolution especially from the bonding of lattice oxygens. The result was analyzed that this difference came from the coordination number of the oxygen. While the Li in NLMO moves to Li slab in the highly oxidizing condition, Mg retains their original position in TM slab. When the shortfall of the oxygen coordination number happened in NLMO due to the migration of Li, the loss of oxygen triggered from the surface of NLMO. In addition, it was also revealed that the total concentration of vacancy in crystal structure determines the stability of oxygen redox rather than depending on the coordination number of the specific oxygen atom near vacancy.[7c, 17]

The same group of materials was discussed with quantified spectroscopic data from Wu et al., provides detailed understanding on the origin of the charge. The charge compensations from lattice oxygen redox, irreversible oxygen oxidation, and Mn were distinguished by the quantification of spectrum from the RIXS technique as shown in **Figure 12c** and **12d**. The consistency between electrochemical evaluation and Mn oxidation trend abled the separation

of TM contribution, and the trend of the unique feature in O K-edge RIXS map allowed to distinguish the reversible oxygen redox from the irreversible oxidation. The collective analysis of electrochemical and spectroscopic results reveals the capacity loss and voltage decay are originated from the irreversible oxygen oxidation which derives significant change of the surface environment. Therefore, the comparison of NMMO and NLMO indicates that the oxygen redox is independent process from the oxygen loss, and the irreversible oxygen oxidation also can be controlled by the environment of the oxygen.

2.4.4 Oxygen redox and Alkali-excess configurations

So far, most of endeavors to understand the oxygen redox in cathode materials have focused on the alkali-rich materials.[37] Furthermore, the theoretical models for oxygen redox require the existence of alkali ion in the transition metal slab forming the oxygen non-bonding states. [3d, 15] However, there have been several reports of oxygen redox reactions in non-alkali-rich cathodes.
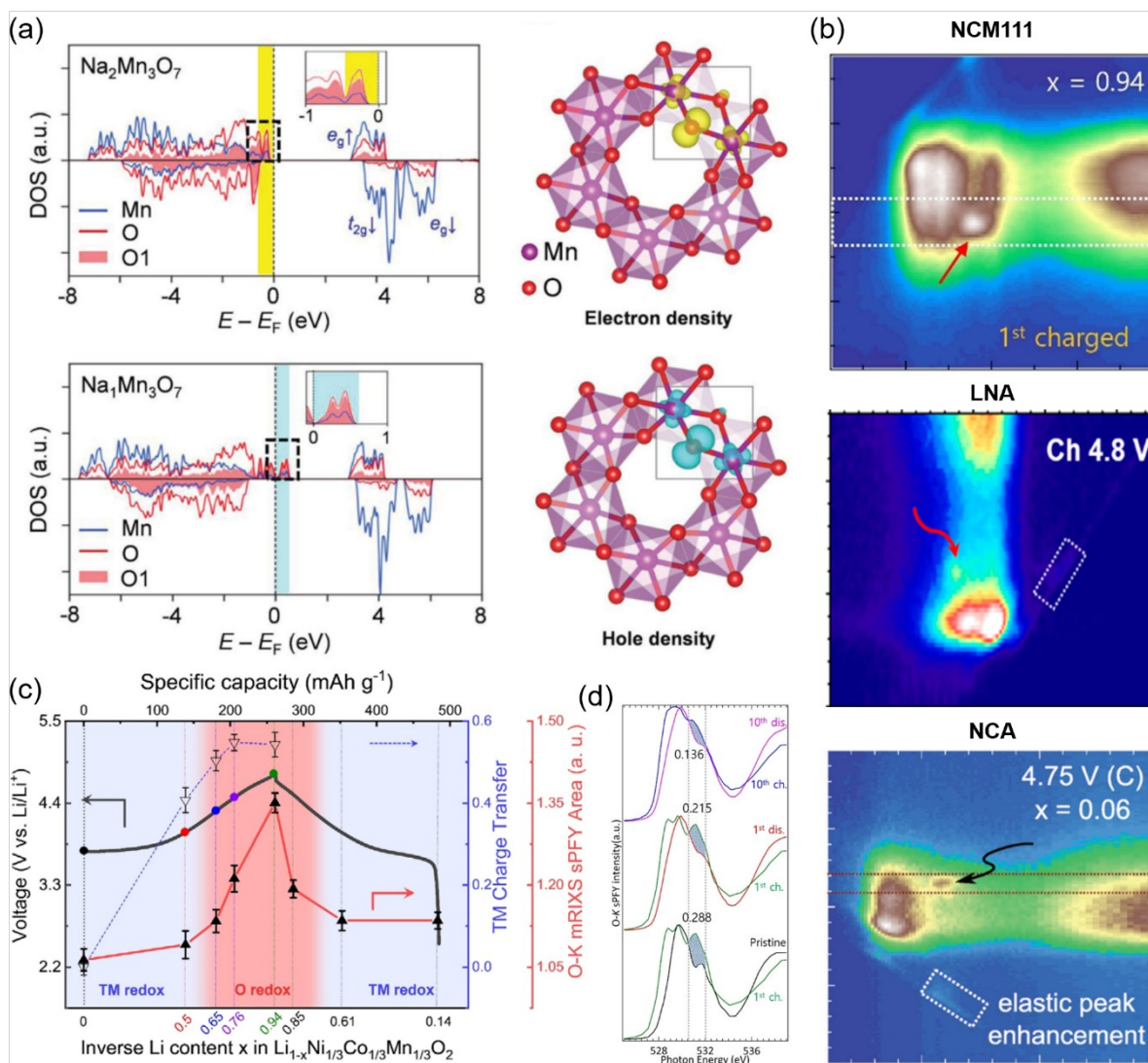
Figure 13. (a) The calculated electron density and hole density near TM vacancy in $Li_2Mn_3O_7$ cathode. Reproduced with permission.[17] Copyright 2018, Wiley. (b) RIXS maps showing oxygen redox feature at highly delithiated Li-stoichiometric cathodes, NCM111, LNA and NCA. (c) Full redox map of NCM111 based on the quantification of sXAS (TM-*L*) and sPFY-RIXS spectra (O-*K*). (d) sPFY-RIXS spectra of NCM111 through the cycling. The reversibility of O redox was evaluated by the ratio of shaded area. Reproduced with permission.[3h, 5] Copyright 2019 & 2020, Wiley, Royal Society of Chemistry & American Chemical Society.

Recent reports have revealed the oxygen redox behaviors in non-alkali-rich cathode materials such as NMMO, $Na_2Mn_3O_7$, $Na_{2/3}Ni_{1/3}Mn_{2/3}O_2$, $LiNi_{1/3}Co_{1/3}Mn_{1/3}O_2$ (NCM111), $LiNi_{0.8}Co_{0.15}Al_{0.5}$ (NCA) and $LiNiO_2$ (LNA), etc.[5, 8n, 12, 26a, 26b, 40] The different kind of environments having no alkali-ion are were reported to have reversible oxygen redox activities. In NMMO, Mg substituted the TM site, oxygen redox behavior was observed and show the different stability with NLMO as discussed part 2.4.3 [26a, 33]. Boisse et al. proved the oxygen redox activity also can evolved through the TM vacancy. The $Na_2Mn_3O_7$, which can be denoted to $Na_{4/7-x}[\square_{1/7}Mn_{6/7}]O_2$ ($\square$: Mn Vacancy), has a structure that the TM site is partially unoccupied unlike alkali-rich materials, which the alkali ion occupies the site instead of vacancy or TM.

As shown in **Figure 13b**, the mRIXS results of the Li-stochiometric layered oxide cathode materials show the fingerprinting feature of the oxidized oxygen states observed in non-alkali-rich cathodes, consistent with some of the speculations on LCO in early 2000s by various research groups.[41] However, these previous works concluded that the partial contribution of oxygen to the charge compensation is via hybridized form that considered as a cationic redox. The modern studies through mRIXS provide strong evidences of the oxidized oxygen state, separated from the typical hybridization effect. Additionally, the quantification of TM and O redox can provide advanced understanding on the whole redox process of the materials. Lee et al. suggested the detailed redox map for NCM111 as shown in **Figure 13c**. [5a] The qualitative trends of TMs consistent with the previous results. The consistency of the TM oxidation state from hard and soft X-ray analysis implies that the redox behavior is not localized property, and the inflection point suggest the oxygen redox became major contributor for the charge compensation from ~4.5 V. Besides, the reversibility of oxygen redox revealed by mRIXS-sPFY in **Figure 13d** suggest the reaction is a partially reversible

oxygen redox process. NCA and LNA were also analyzed through similar methods and concluded that they also have the reversible oxygen redox process with the quantified redox map.[3h, 5]

While the oxygen redox in non-alkali-rich cathodes does not provide additional Li more than one per each $LiTMO_2$ unit, the fundamental understanding of oxygen redox in those cathodes is crucial to extend their operation range to high potentials. The vulnerable status of highly delithated $LiTMO_2$ limits the full utilization of the material, preventing the side reactions of materials will lead the enhancement of performances such as capacity and cyclability. The side reactions such as gas evolution and the densification of material are the major degradation factors of Li-stoichiometric layered oxides, their oxygen activity which is similar with the one in alkali-rich cathode suggests the necessity of stabilization of the oxidized oxygen. Therefore, more detailed and comparative studies to clarify the origin of oxygen redox in non-alkali-rich cathode are in urgent need, which is strongly coupled to the ultimate clarification of the fundamental mechanism of the oxygen redox reactions in all oxide cathode materials.

3. Revisiting of the strategies for layered oxide cathodes in oxygen redox point of view

3.1. Material engineering strategies at crystal structure level

3.1.1 Alkali-ion exchange

The crystal structure of the materials is energetically determined, a phase has lowest energy is finally made after the synthetic procedure. Therefore, making a polymorph is challenging and needs special procedures such as quenching, step control and so on. On the other hand, the alkali-ion exchange provides facile route to realize different structure without expensive procedures. The size difference of alkali-ions such as Li^+ (0.76 Å), Na^+ (1.02 Å) and K^+ (1.38

Å) makes the different parent structure, and structure is succeeded by other alkali-ions by the cation exchange. For example, while the β-Li_2IrO_3, a polymorph of Li_2IrO_3, can be synthesized through the optimization of sintering process, the trials to obtain β-Na_2IrO_3 by sintering was not successful. Instead, Pearce et al. made β-$Na_{1.7}IrO_3$ by electrochemically substituting the Li with Na.[42] The deficiency of Na in the material implies the host structure does not have enough space to contain 2 Na ions as it was fit for 2 Li ions.

Like Pearce's work, the electrochemical alkali-ion exchange is most usual ways to obtain the target structure. The exchange can be conducted through various ways such as sintering, aging in the electrolyte, using alkali halides, etc.[43] Gao et al. used two methods, sintering and electrochemical exchange, to make the K-birnessite material.[43a] Yang et al. rhombohedral $Li_3V_2(PO_4)_3$ by aging the $Na_3V_2(PO_4)_3$ in the Li electrolyte.[43b] The spontaneous exchange of ions was occurred due to the energy difference between Na and Li. Park et al. introduced LiBr solution to substitute Na in $Na_{1.5}VOPO_4F_{0.5}$ with Li to observe the kinetic when they are exchanged. The concentration of LiBr determined the contents of Li in the $Na_{1.5}VOPO_4F_{0.5}$, the in-situ synchrotron analyses observed their exchange behavior. The proper methods should be chosen considering the chemical and physical property of materials.

Unlike the robust structures in polyanion or spinel structures retain their parent structures after the ion exchange, the flexible interlayer interactions make the free exchange of alkali ions. When the larger alkali-ion substitute the existing ion, the interlayer expands and accept the new ions. Meanwhile, the TM-O slab glides to form a stacking which lowering the energy of the crystal structure. Due to the structure change, the expectation of physical properties of ion exchanged materials are much harder than that of polyanion or spinel structures, even more challenging if the chemical composition of layered oxide cathodes is complex.

Therefore, experimental studies are necessary to elucidate the accurate properties of materials.

Figure 14 shows an example that how the electrochemical property of material can be modulated by ion exchange.[42d] As shown in **Figure 14a** and **14c**, XRD pattern change of B to C indicates that the stacking sequence of Li-NCM811 is changed when the Na ions are electrochemically inserted to delithiated host structure. While the other Ni-rich Na layered cathodes suffers the multiple plateaus from gliding of slabs and Na/vacancy ordering, this structure makes smooth voltage profiles and the plateaus are hardly observed.[44] Due to the relieved structure change during the cycling, the material shows the decent cycle life. Similarly, Hwang et al. reported a cathode for K-ion batteries (PIB) by the ion exchange of O3-NaCrO$_2$.[42b] The work is motivated by the difficulty of directly synthesizing K$_x$CrO$_2$, the obtained P3-K$_x$CrO$_2$ show the recordable cyclability among PIB cathodes in 2018 as shown in **Figure 14d**.
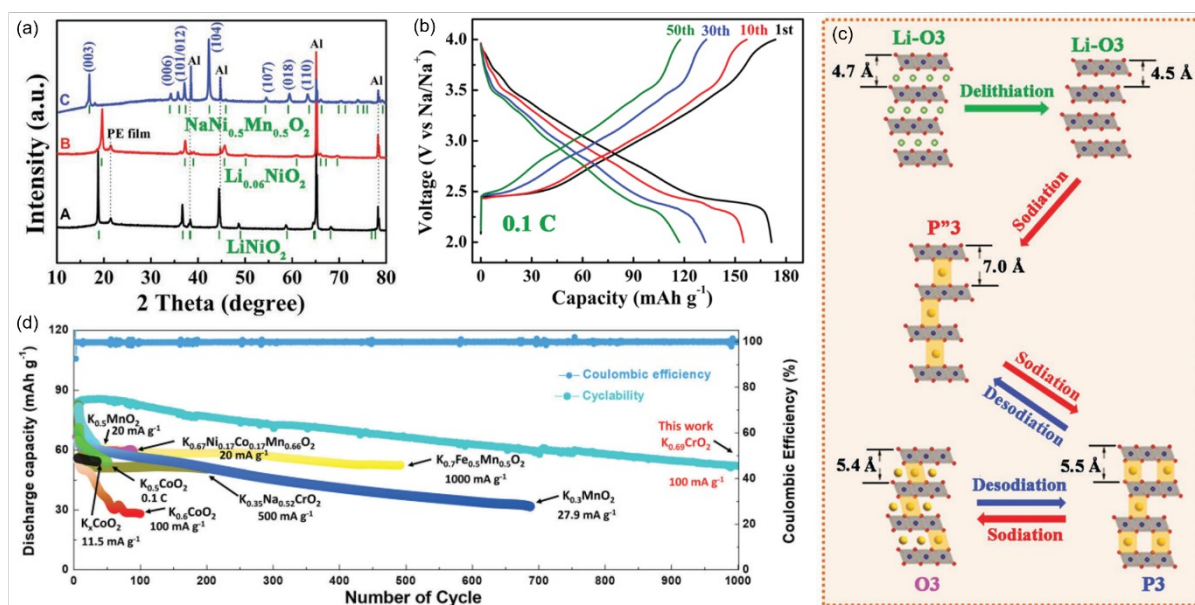
Figure 14. (a) XRD patterns of Na-ion exchanged LiNi$_{0.82}$Co$_{0.12}$Mn$_{0.06}$O$_2$ (Na-NCM811). A, B and C regards to different charged states that pristine, Li-ion extracted and Na-ion inserted states, respectively. (b) The voltage profiles of Na-NCM811 at 0.1 C of current density. (c) A

schematic of phase evolution through the ion exchange and consequent cycles. Reproduced with permission.[42d] Copyright 2019, Wiley. (d) Cyclability of $K_{0.69}CrO_2$ over 1000 cycles at 1C rate and comparison of specific capacity vs. cycle number for the layered oxide cathode. Reproduced with permission.[42b] Copyright 2018, Royal Society of Chemistry.

In oxygen redox point of view, Eum et al. recently reported an important result using the ion exchange method stabilizing oxygen redox in the layered oxide.[7a] The P2-NLNMO originated stacking period was retained for O2-LLNMO, the sharing of TM octahedra was modulated as **Figure 15**. O2-LLNMO has different migration pathway from O3-LLNMO, the irreversible migration of TM to Li slab was prevented by repulsion between TMs. The migration of TM is confined to their intermediate states as shown in Figure 11, the migrated TMs to Li slab went back to their original site after discharging process. According to the discussion in part 2.4.1, the ion exchange method seems to indirectly contributes to the stabilization of oxygen redox by preventing the TM migration as the dynamic property of oxygen redox state is induced by the migration of TM suggested by Gent and Yahia et al.
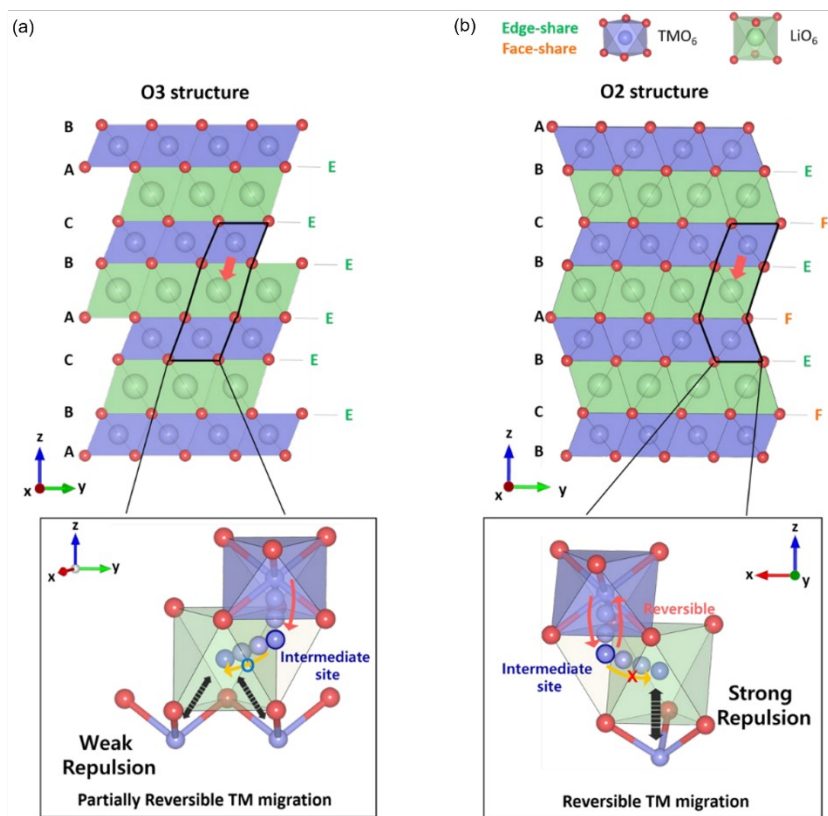
Figure 15. Cation migration pathway modulation of $Li[Li_{0.2}Ni_{0.2}Mn_{0.6}]O_2$. Crystal structures and migration pathways of (a) O3 structure and (b) O2 structure. Reproduced with permission.[7a] Copyright 2020, Springer Nature.

Other than this viewpoint, the expansion of interlayer spacing when the larger ion was substituted. As suggested in the Figure 3,[11] the condensation of oxygen gas can be prevented by far interlayer distance even though the cathodes do not contain 4d or 5d TMs if the structure is maintained in highly charged state like the case of $P3\text{-}K_xCrO_2$.[42b]

In summary, the exchange of parent structure does not ensure the totally same structure parameters, and some sensitive structural factors such as local symmetry, stacking sequence of layered oxides can be changed after the ion exchange and even during cycling. Nevertheless, the unique structures which is not able to be synthesized by usual procedures are obtained with the methods, the structures are worth to be studied to explore the

unexpected novel structure of cathode materials having better structural and oxygen redox stabilities.

3.1.2 Doping for the better oxygen redox activities

The doping for layered oxide cathodes has been a routine way to enhance the performance of cathodes, however, the aesthetic feature that even with a trace amount of dopant can lead dramatic enhancement of performances makes the doping keep attractive. Furthermore, the various properties such as electronic structure, bond characters or mechanical properties of cathodes can be minutely tuned by the type, occupancy sites and concentration of dopants, the deep exploration of doping strategy provides a favorable material structure to manifest the reversible redox. In this part, we introduce the effects of the doping to increase the structural stability of cathodes and discuss about the effect of the tuned structures to the oxygen redox activities.

The extraction of alkali-ion induces the significant change such as slab gliding and TM migration.[45] The gliding of slab by the extraction as the O repulsion between two TM-O slabs getting stronger when the Li is extracted. The repulsion increases the energy of the phase, which leads the phase transition to other phase has lower energy. In addition, the order-disorder phase transition usually observed in LCO also induced by the Li extraction, which results the gliding of slabs. When some dopants were employed in the structure, it can make the slabs not to be glided in various aspects.

When a dopant occupies a site in alkali-ion slab of layered oxides, the dopant has different electrostatic interaction with neighboring two TM-O slabs.[46] If the size of the ion is larger than the original alkali ion, the ion sterically expands the interlayer spacing, and if the ion has higher valence state the alkali ion, it makes stronger interaction with lattice oxygen. As a

result of the doping, the gliding of slabs is hindered, the effect is also known as "Pillar effect"

as it looks like the immobile atom props up the two slabs. Other than the basic concepts of

the pillar effects, additional effects from various dopants have been investigated. Choi et al.

reported a selective Mg doping in the Li slab of Mn-rich NCM cathodes.[46c] In NCM, Mn has

relatively higher electronegativity than other TM, Mg^{2+} is more stabilized near the Mn by

forming Mg-O-Mn interaction. Even though the Mg does not show the selectivity for doping

site, TM or Li site, the richness of Mn makes the Mg more prefer the Li slab near Mn.[45b] As

a result, the interaction hinders the migration of Ni to the Li slab, mitigate the degradation of

the layered-to-spinel phase transition. On the other hand, Liu et al. intentionally induced the

migration of Ni to use it as a pillar of the material by engineering the Li vacancy in LMR.[46b]

The migrated Ni not only increase the stability of the phase but also facilitate the Li

extraction from Li_2MnO_3 by lowering the energy barrier. The lower kinetic property of

oxygen redox is enhanced by the engineering of tetrahedral site hopping, the rate capability

of LMR greatly enhanced as shown in **Figure 16e**. Also, the report from Zhang et al. about

Zn doping in $Na_{0.833}[Li_{0.25}Mn_{0.75}]O_2$ suggest the interaction with TM (Mn) and the pillar ion

(Zn) can relieve the Jahn-Teller distortion and the computational results (**Figure 16g** and

16h) suggest that the doping provides more energetically stable states which prevent the

phase transition of P2 to P2'.[46j] Resultantly, the consequent oxygen loss induced by the P2 to

P2' transition is also relieved by the Zn doping.
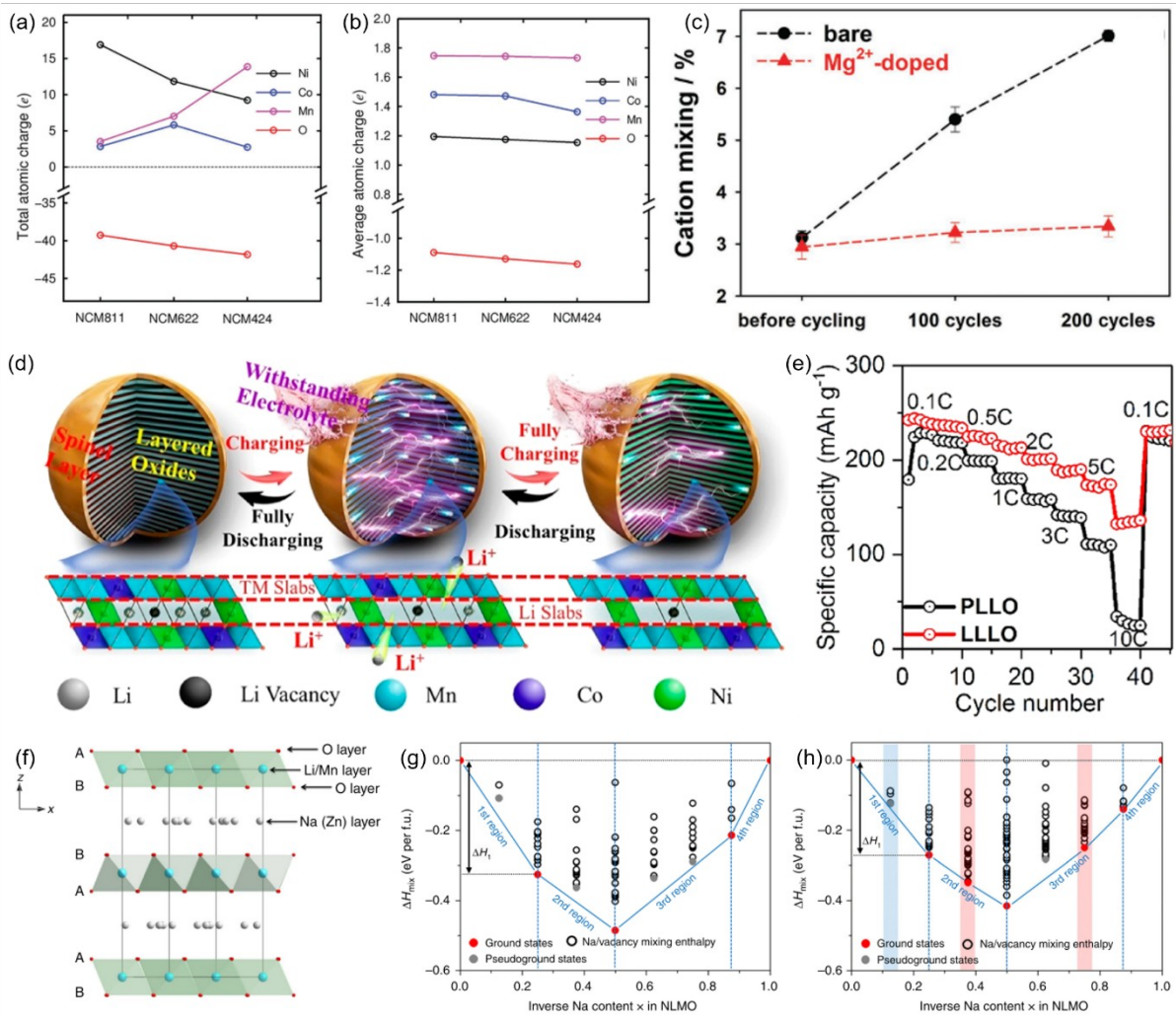
Figure 16. The (a) total charges and (b) average charges of Ni, Co, Mn and O in the NCM 811, NCM622 and NCM 424. (c) The amount of cation mixing for pristine NCM and Mg-doped NCM. Reproduced by permission.[46c] Copyright 2018, Wiley. (d) The schematic for in-situ doping of Ni in Li slab. (e) The rate capability test for pristine and Ni-pillared LMR. Reproduced with permission.[46i] Copyright 2019, American Chemical Society. (f) The crystal structure of Zn-doped $Li_{0.833}[Li_{0.25}Mn_{0.75}]O_2$. The calculation of the energy of ground states for (g) pristine and (h) Zn-doped NLMO. Reproduced with permission.[46j] Copyright 2019, Wiley

The dopants substituted in the TM sites also have significant effects to the phase stability, it induces many unexpected effects that mitigating phase transitions.[6b, 45a, 47] Zhang et al. reported that a trace amount of Al can significantly prevent the order-disorder transition of LCO.[45a] The order-disorder transition, which is considered as a major degradation factor of LCO, have limited the extraction of Li from LCO over than half. As shown in **Figure 17a**, the transition of LCO is reflected as a kink in the voltage profile, however, the kink is not observed after the doping of La and Al. The major phase stabilization effect is from the Al, the invariant charge of Al^{3+} during the charge block the reorganization of Li vacancy. Resultantly, the volume change of LCO was relieved due to the absence of phase transition as proved by in-situ XRD (**Figure 17c**). The Sn doping in LCO reported by Zhao et al. suggests a similar strategy with Liu's report.[47g] The Sn exist as Sn^{4+} in the LCO, and the valence is invariant during the charging process. However, the voltage profile still shows the kink after the doping as shown in the Figure 17a, it seems to Sn does not prevent the order-disorder transition. Instead of the order-disorder transition, in-situ XRD results suggest that the layered-to-spinel transition is relieved. Zhao et al. suggested the decrease of vibration in the material as one of the causes. As proved by electron paramagnetic resonance spectra (EPR) and Rietveld refinement of XRD results, the heavy Sn decreases the vibration of TM-O and makes CoO_6 octahedron lesser distorted after charging.
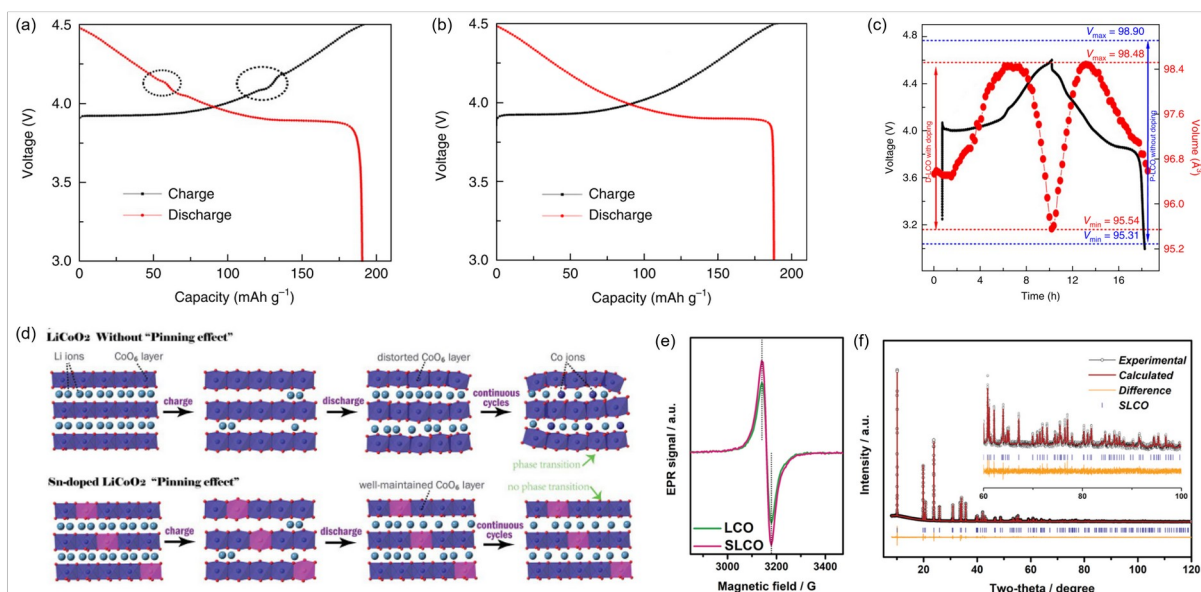
Figure 17. The voltage profile of the (a) pristine (b) La, Al doped LCO. The dotted circle indicates the order-disorder transition. (c) The trend of volume of LCO crystal structure extracted by the in-situ XRD. Reproduced with permission.[48] Copyright 2018, Springer Nature. (d) The schematic of pinning effect by the Sn doping in LCO. The comparison of (e) electron paramagnetic resonance spectra and (f) the Rietveld refinement results of Sn-doped LCO. Reproduced with permission.[47g] Copyright 2020, Royal Society of Chemistry.

While some elements have enough solubility to be incorporated to the targeted layered oxides, some are not.[49] It means the homogeneous doping of those elements to the structure is not stable, most of dopants exceeding the solubility segregated out or concentrated to the surface of the target compounds. In case, the chemical composition of the dopant is dominant in the surface, show very different electronic structure with the target compounds. By the utilization of the solubility, the phase stability of the surface could be enhanced by concentrating the dopants at the surface. Zhang et al. simultaneously employed the three elements, Ti, Mg and Al in LCO, Ti shows much higher concentration at the surface while Mg and Al show similar concentration for the surface and bulk region (**Figure 18b** and **18c**).

44

[45a] The lattice oxygen in the surface could retain the charge with the trace amount of Ti, the surface is lesser reactive than the pristine material as shown in **Figure 18d** and **18f**.
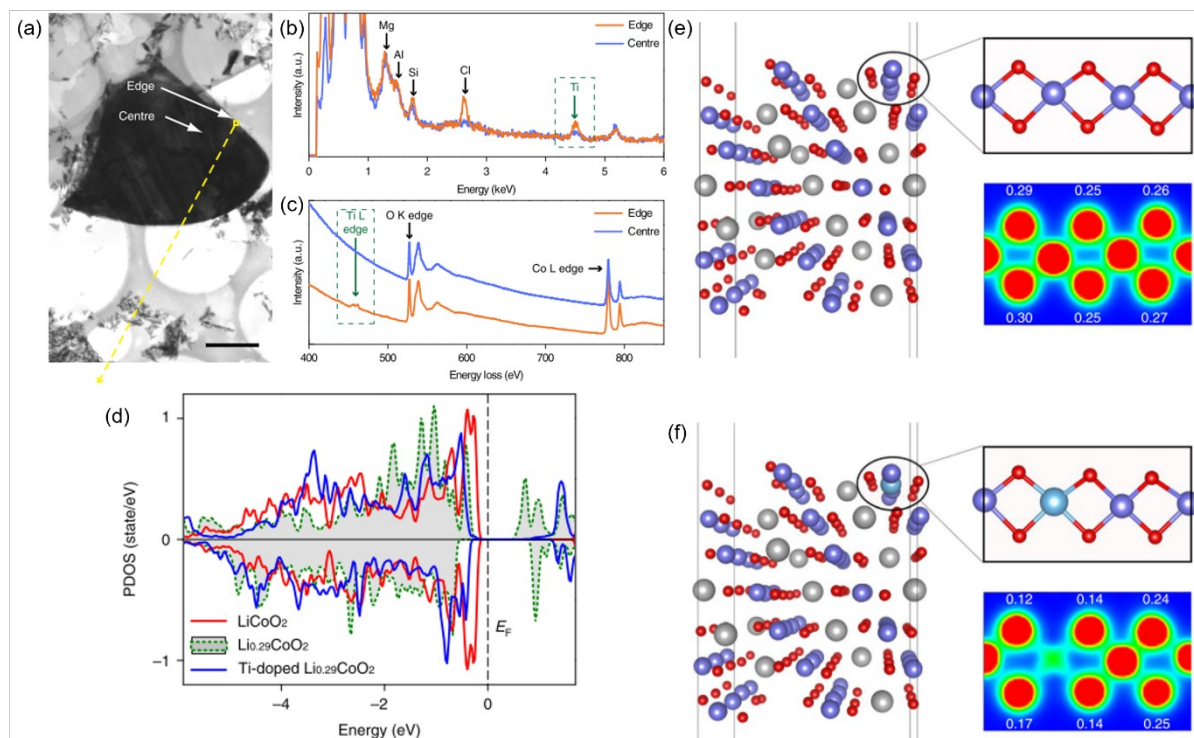
Figure 18. The (a) transmission electron microscopy (TEM) image, (b) electron dispersive spectroscopy (EDS), and (c) electron energy loss spectroscopy (EELS) results of Mg-Al-Ti doped LCO. (d) The calculated partial density of states of LCO, delithiated LCO, and Ti-doped LCO. (e, f) The top views of the surface structure and surface charge density contours of (e) LCO and (f) Ti-doped LCO. Reproduced with permission.[45a] Copyright 2019, Springer Nature.

Likewise, the dopants introduced in the layered oxides can make enhancement of the performance in various ways such as the mitigating the phase transition to the tuning the electronic structure of the cathodes. As a result of the phase stabilization, the performance related to the oxygen redox also enhanced by the modified structure, the doping seems to

effective strategy to enhance the overall performance of the cathodes. However, even though the numerous reports about the doping of layered oxide cathodes have provided abundant information about the effect of the doping, the history of oxygen redox is too short to elucidate the correlation between the doping and the oxygen redox. As suggested above, many factors such as occupancy site, concentration, solubility, and valence of ion determine the effect of doping, it makes difficult to expect how the oxygen redox will be affected by the doping in real system.

3.1.3 Surface reconstruction of cathodes

The degradation of the surface in layered oxides includes the densification and oxygen loss process, various approaches are employed to protect the surface from the degradation factors. [50] Among the approaches, engineering surface environment has been effective to prevent TM dissolution, O_2 gas evolution. In O oxidation perspective, the interfacial reactions from the labile O have been considered one of factors to derive the degradations, the surface engineering is an intuitive way to conserve the O from the unwanted reactions during the cycling. The O can be shielded by coating of more robust materials or the environment of surface oxygen can be tuned by several treatments. As the effect of coating is highly dependent to the property of heterogeneous materials and microscale factors, it will be discussed in part 3.2 with more detailed classification of materials. In this section, we discuss about the stabilization effect on O by surface reconstruction in oxygen redox point of view. As the lattice oxygen terminated surface is susceptible to react with electrolyte, various approaches tried to substitute the surface lattice oxygen framework to other more stable systems such as polyanion, fluorinated or spinel structures.[2f, 6a, 51] Min et al. introduced a O_2-PO_4 framework at the surface of LCO by reacting the oxophile organic phosphine on the

surface of LCO, Zhao et al. doped -PO_4 to the surface of LMR by calcination with phosphate salt, $NH_4H_2PO_4$.[2f, 6a] As shown in Figure 18b-e, the surface of layered structure is changed when the PO_4 was doped. The STEM images in two works suggested something occupies the Li slab, two different explanations are provided that phosphorous occupies TM site in Zhao's work (**Figure 19d** and **19e**) and Li site in Min's work (**Figure 19b** and **19c**). Regardless of the different explanation, both works suggested the strong covalency between P and O mitigated the TM migration and loss of oxygen after employing the PO_4 structure at their surface. Figure 16f suggests that the cyclic performance of LMR is much enhanced by the phosphate doping, the STEM images in Figure 16h and 16i suggest that the amorphization of LMR is prevented. In addition, the similar surface reconstruction behaviors by -BO_4, -SiO_4 were observed and lead the enhancement of performances.[6a]
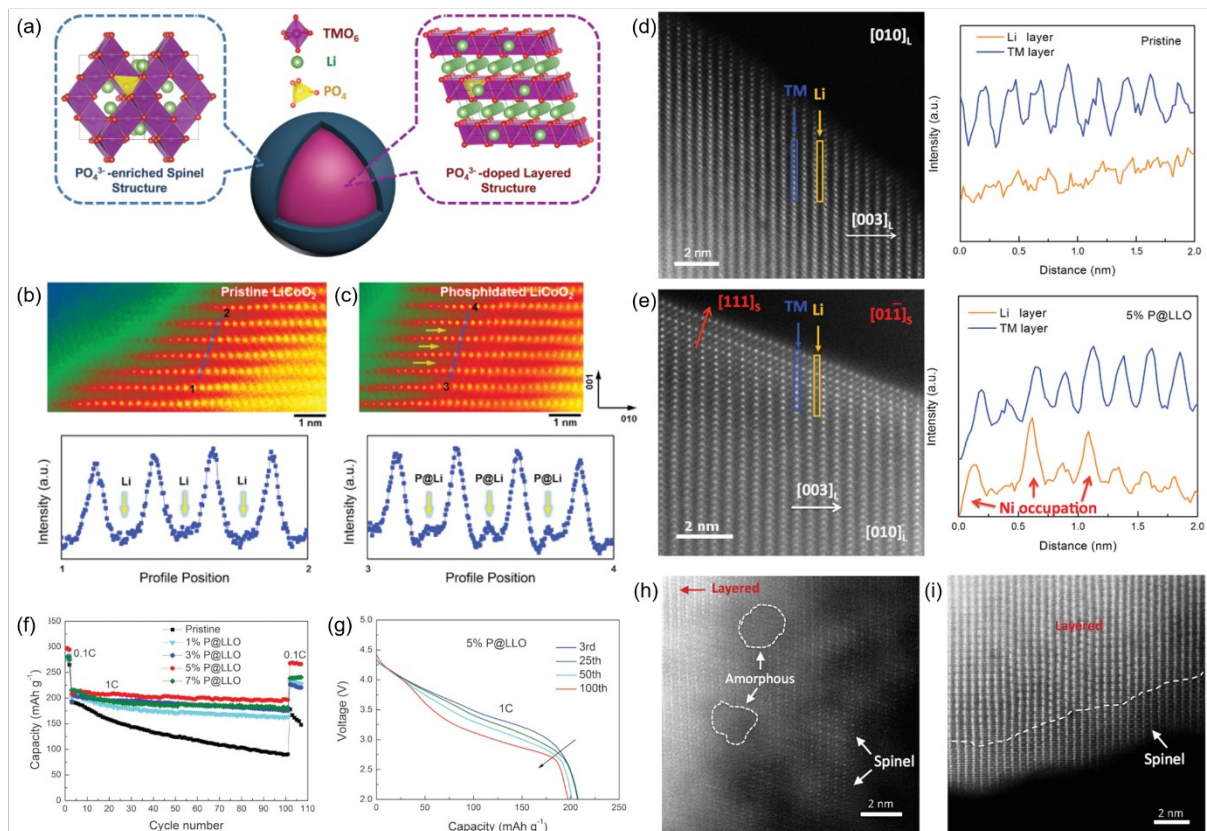


Figure 19. (a) A schematic of -PO_4 doped layered oxide cathodes. (b-c) STEM results of pristine and phosphidated LCO. Reproduced with permission.[2f] Copyright 2016, Wiley. (d-e)

STEM result of pristine and -PO$_4$ doped LMR. (f) Capacity trend of PO$_4$ doped LMR for different concentration of PO$_4$. (g) Change of the voltage profile in consequent cycles. STEM image of cycled (h) pristine LMR and (i) PO$_4$ doped LMR. Reproduced with permission.[6a] Copyright 2016, Wiley.

It seems clear that the propagation of phase degradation is mitigated when the spinel-like (oxygen-deficient) phase is formed as a protective layer at the surface of cathodes as shown in **Figure 19h** and **19i**. With this motivation, several studies tried to form the oxygen deficient phase to prevent the oxygen loss and degradations by reductive processes such as gas treatments, acid treatments, or synthetic condition control.[52] For example, the NH$_3$ gas treatment reported by Erickson et al. protonate the surface of LMR, the Li ion is leached out and loss of lattice oxygen is followed due to maintain the charge balance.[53] As a result of reduction, the layered-to-spinel transition was induced, the surface was covered by the oxygen deficient spinel-like phase. Similarly, wet chemical process using acid solution makes the oxygen deficient phases through the protonation of the cathode surface. While some studies concentrated the structural stabilization effect from the layered-to-spinel transition, other emphasized the importance of oxygen vacancies to mitigate the oxygen loss.[6b, 52b] The CO$_2$ gas treatment reported by Qui et al. extracts the Li and O from the surface by inducing the formation of Li$_2$CO$_3$ rather than directly reduce the surface with reductants. **Figure 20a** illustrates the formation of oxygen deficient surface after reacting cathode surface with CO$_2$ and their effects during the electrochemical reaction. Qui suggested that the oxygen vacancies decreased the partial pressure of oxygen gas at the surface, and it reduces the oxygen loss. Furthermore, the oxygen vacancy induced by gas treatment facilitates the migration of Li in the Li$_2$MnO$_3$ domain, which provides more stable structure for the oxygen redox process. In

addition to this perspective, Lin et al. suggested the facilitated Li migration relieves the strain of the c-lattice as the extraction of Li is not dominant from "primary Li extraction (PLE)" but dispersed to "secondary Li extraction (SLE)" as shown in the **Figure 20b**.[6c]
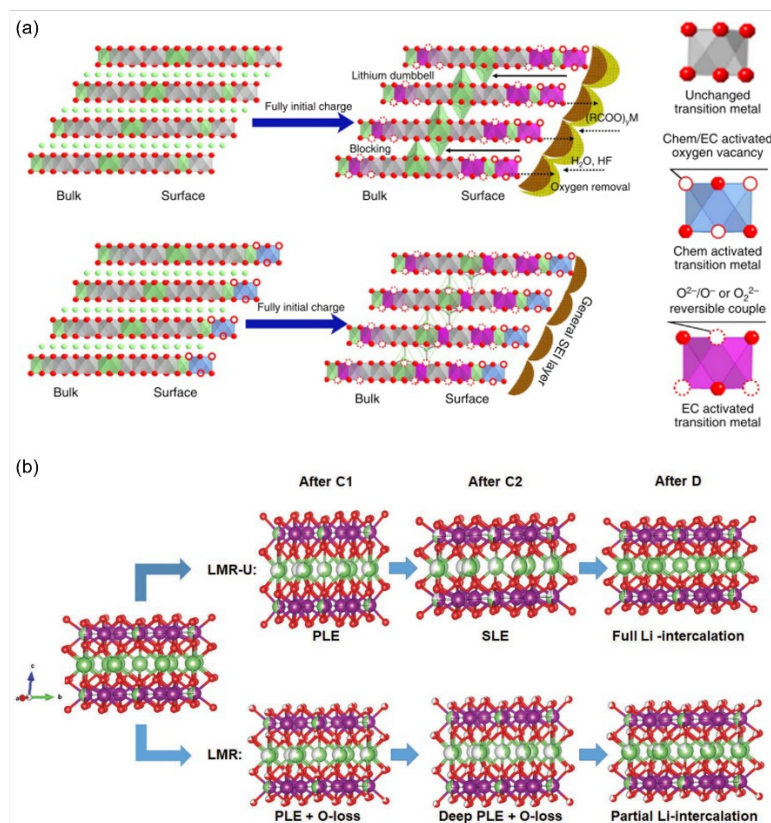
Figure 20. (a) A schematic of pristine LMR and chemically activated LMR by CO_2 treatment. The blue octahedra indicates the chemically/electrochemically activated octahedra act as a protective layer. Reproduced with permission.[52b] Copyright 2016, Springer Nature. (b) A schematic of Li extraction from LMR and LMR-U (having oxygen vacancy). Reproduced with permission.[6c] Copyright 2020, Wiley.

Recently, Ramakrishnan suggested how this surface construction can be related with the oxygen redox in the layered oxides based on the quantification of peroxo-like species.[52j] In this work, the formation of peroxo-like species was assumed as a result of oxygen redox, the

49

peroxo-like species was titrated by the concentrated H_2SO_4. The titration results of pristine

and acid treated LMR suggests that the reversibility of bulk O redox is invariant by the

treatment as shown in **Figure 21a** and **21b**, and the isotopic DEMS analysis for charge

electrode indicates the irreversible O_2 loss is arisen from the surface of cathodes not the bulk.

In contrast, CO_2 analysis of two cathodes show a stark decrease of CO_2 evolution as shown in

Figure 21c, which suggests the acid treatment is highly related to minimizing the surface

effects.
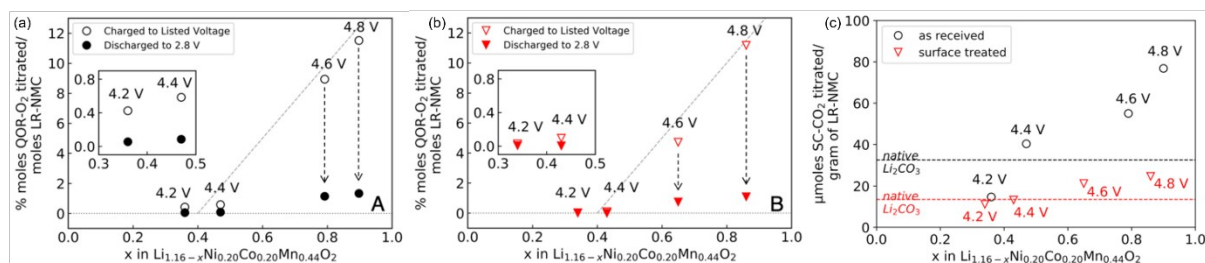
Figure 21. The quantification of oxygen redox (QOR-O2) results for different charged states

of (a) pristine, (b) acid treated LMR electrodes. (c) The amount of CO_2 evolved from the two

cathodes at various charged states. Reproduced with permission.[52j] Copyright 2020,

American Chemical Society.

The conclusion of Ramakrishnan's work is also consistent with the results from other reports

using surface reconstruction methods. After tuning the surface, the electrochemical

performance change shows common points that the gas evolution and cycle performance are

significantly enhanced, however, the effect on the voltage hysteresis is limited. As we

discussed in the part 2.4, the O loss of cathode is mostly surface phenomenon, and voltage

hysteresis attributes to the bulk phenomenon. Therefore, the change of surface environment

can enhance the surface related properties while it does not affect to the bulk properties of

cathodes. Nevertheless, the penetrating property of surface degradation makes the surface reconstruction promising for cathodes. Therefore, the combination with bulk stabilization strategy is anticipated synergistically protecting the bulk structure and the surface from the degradation.

3.2 Microstructure engineering

3.2.1 Structural evolution at micron scale

The aforementioned modifications at the atomic scale of the material bulk or surface seek to directly redress the mechanistic causes of the cathode deterioration processes arising from (ir)reversible oxidation of the lattice oxygen. However, as alluded to above, a multitude of other deterioration processes is indirectly initiated by participation of the oxygen in the electrochemical reaction, such as the dissolution of the transition metal(s) into the electrolyte, which accompanies gaseous oxygen evolution and can lead to permanent reduction of cathode capacity due to loss of the redox-active sites, a process that may be further aggravated by the negative effects associated with deposition of transition metal species in the anode (i.e. the so-called cathode-anode cross talk).[54] Another performance-damaging outcome is the formation of the so-called cathode-electrolyte interface (CEI) from oxidative electrolyte decomposition at high voltage, resulting in high impedance and thus reduced ion transport across the interface.[55] In addition to surfacial processes, changes in the bulk lattice caused by (ir)reversible oxygen oxidation (possibly accompanied by layer-to-spinel phase change) together with repeated unit cell expansion and contraction associated with redox cycling induce mechanical stress within individual crystals or at the grain boundaries, eventually causing fractures that propagate throughout the cathode particles into cracks at the micron-scale.[56] As the electrolyte infiltrate into these cracks, the exposed cathode surface

51

would then be subjected to the harmful processes mentioned, specifically surface corrosion (i.e. HF-induced metal leaching into electrolyte) and/or CEI formation.[57] Furthermore, this repeated volume change in the cathode oxide also loosens the compaction of the electrode constituents and ultimately leads to loss of contact between the redox-active material, the carbon conductor and binder, as well as possibly the current collector, which can be visualized, for example, by electron microscopy techniques.[58] Considering that the severity of these degradation mechanisms is related to the amount of cathode surface exposed (to the electrolyte), altering the microstructure of the cathode material offers a general strategy alternative to modification at the atomic scale discussed to mitigating performance loss over extensive cycling.[54a, 56a] The sections below highlight some recent developments targeting the intrinsic and extrinsic modification of cathode microstructure, where we distinguish the two as follows. Intrinsic modification refers to methods of stabilizing the structure of the active material inherently, while extrinsic modification describes forming composites of the cathode material with other compounds to inhibit structural deterioration of the cathode. Although the preceding section on oxygen redox covers a range of cathode material types, this section will focus exclusively on microstructure modification of $LiNi_xCo_yMn_zO_2$ (henceforth abbreviated as NCM followed by numbers indicating the atomic ratio between the three transition metals), considering the commercial importance of this cathode material. Since current research trend is aiming towards extracting more capacity by elevating the operating voltage to well beyond 4.3 V vs Li, participation of the lattice oxygen in the electrochemical oxidation becomes prevalent in participating (which we recently demonstrated for NCM111) [5a] and therefore exercabates the aforementioned degradation mechanisms. Hence, the following review of microstructural modification will cover general approaches on improving performance (in terms of achieving both high capacity and long cycle life), as well as

highlighting examples where a distinct improvement is observed at an upper voltage limit beyond 4.3 V, even if stabilizing oxygen redox was not the original research motivation.

3.2.2 Extrinsic modification of NCM microstructures

During the early years of NCM development, the active material was prepared by standard solid-state synthesis route and comprised crystalline primary particles of several hundred nanometers aggregating into secondary particles of tens of micrometers.[59] However, while the small primary particles provide a short ionic diffusion pathway conducive to electrochemical reaction kinetics, this microstructure morphology is increasingly recognized to be unsuitable for capacity retention over the long term, given that the large amount of surface area and grain boundaries are the starting points of several degradation mechanisms described above. Hence, recent research efforts have been directed towards synthesizing micron-sized NCM single crystals, which are anticipated (and subsequently confirmed by experiments) to have an enhancement in intrinsic performance owing to the reduced amount of sites for surface degradation process to be initiated.[60] The optimum range of particle size for the single crystals is considered to be 1–5 μm, based on the competing demand of larger particle size for high tap density and smaller particle size for shorter ionic diffusion pathways. [61] With this target in mind, recent research has focused on method development for the preparation of NCM single crystals and investigation of their structural and electrochemical properties as dependent on microstructure, as well as their utilization for fundamental studies for the elucidation of structural evolution during cell operation. The discussions below will primarily focus on achievements in the last three years with due reference to earlier work where appropriate.

Synthesis of single crystalline NCM

To synthesize discrete, micron-sized single crystals (as opposed to secondary particles that are aggregate of single crystalline primary particles), common routes either employ multi-step calcination of precursors produced from co-precipitation of transition metal salts, or use a salt melt as synthesis medium. In one of the first synthesis procedures of the former as described by Fu et al.[62] and illustrated in **Figure a**, poly(vinylpyrrolidine) (PVP) was used to regulate the kinetics of nucleation and particle growth through coordination interactions and viscosity during the co-precipitation of the transition metal salts into the hydroxide as the NCM precursor. Here, PVP was thought to also serve as a capping agent so as to yield the mixed metal hydroxide precursor with a plate-like morphology, which has a pre-organization effect upon the crystallinity of the final NCM material. Mechanistically, in calcining platelets of precursors mixed with the lithium source, the authors proposed that this morphology promotes Li^+ insertion in-between the transition metals layers as the hydroxide decomposes in a two-step calcination sequence into the final NCM oxide, which has a brick-like morphology as seen in the SEM image of **Figure b**. Other than PVP, similar brick-like or disc-like morphology has since been achieved using ligands such as ethylene glycol by itself or together with citrate acid as part of the Pechini synthesis methods.[63]
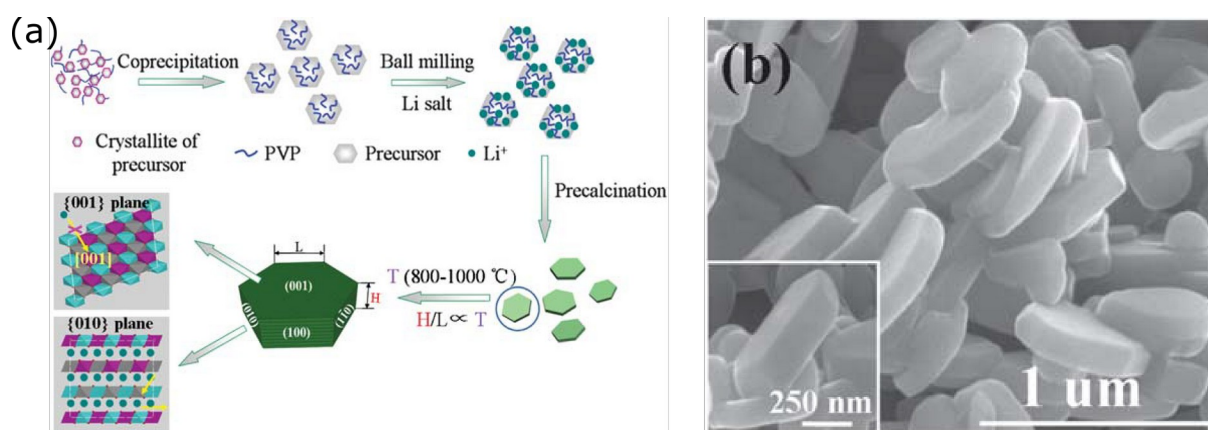
Figure 22. Synthesis of single crystals of NCM: (a) Synthesis route as described by Fu et al. by co-precipitation of the transition metal salts in the presence of PVP into the metal hydroxide platelets as the precursor to NCM. Multi-step calcination of this precursor with a lithium source led to NCM with controllable dimensions of layer width L and height H. (b) SEM image of the resultant single crystalline NCM with a brick-like morphology. Reproduced with permission.[62] Copyright 2013, Royal Society of Chemistry.

An alternative route to NCM single crystal is to use a salt melt, which acts as a thermally stable solvent to regulate the transport of solutes for crystal growth and nucleation. While this route has been previously explored for preparation of NCM secondary particles, Kimijima et al. were the first to employ this synthesis route to obtain discrete NCM single crystals, using Li_2MoO_4 (melting point 705 °C) to solubilize the metal constituents and forming the final product in a single calcination step.[61, 64] By adjusting the solute-solvent concentration and heating duration, dispersed primary particles can be obtained with controllable range of size (though with some polydispersity), since the salt melt prevents particle aggregation and induces Ostwald ripening to steer the synthesis towards crystal growth. The use of salt melt as synthesis medium adds a handle to controlling the outcome of the final NCM particles, especially in terms of the morphology, as the constituents of the melt can affect the growth

and stabilization of particular surfaces. In selecting the salt melt used, Chen and coworkers proposed oxygen and lithium chemical potential during the synthesis to be descriptors affecting the final NCM morphology. This is based on density functional theory (DFT) studies which found the (012) and the (104) surfaces to be the least and most stable surface, and the prevalence of these different surfaces, and in turn the equilibrium crystal morphology, in the final NCM crystal is dependent on the chemical potential of these two elements, as graphically summarized in **Figure 3a** and **23b**.[65] Experimentally, oxygen chemical potential can be varied qualitatively by the calcination temperature or how oxidative the synthesis environment is. On the other hand, the lithium chemical potential can seemingly be varied by the amount of lithium relative to the transition metal precursor, with the lithium present either as a reactant (e.g. Li_2CO_3) or as a component of the salt melt (e.g. $LiNO_3$/LiCl eutectic).[66] With these considerations, the authors demonstrated all equilibrium morphologies with various Ni:Co:Mn ratios are synthetically accessible by controlling the lithium and oxygen chemical potentials through the choice of precursor and components of the salt melt, as well as tuning the heating time and duration, as shown in **Figure 3c**. Within the various morphologies, the particle size of the final NCM can be adjusted by varying the ratio between the solute and the solvent (i.e. the salt melt).
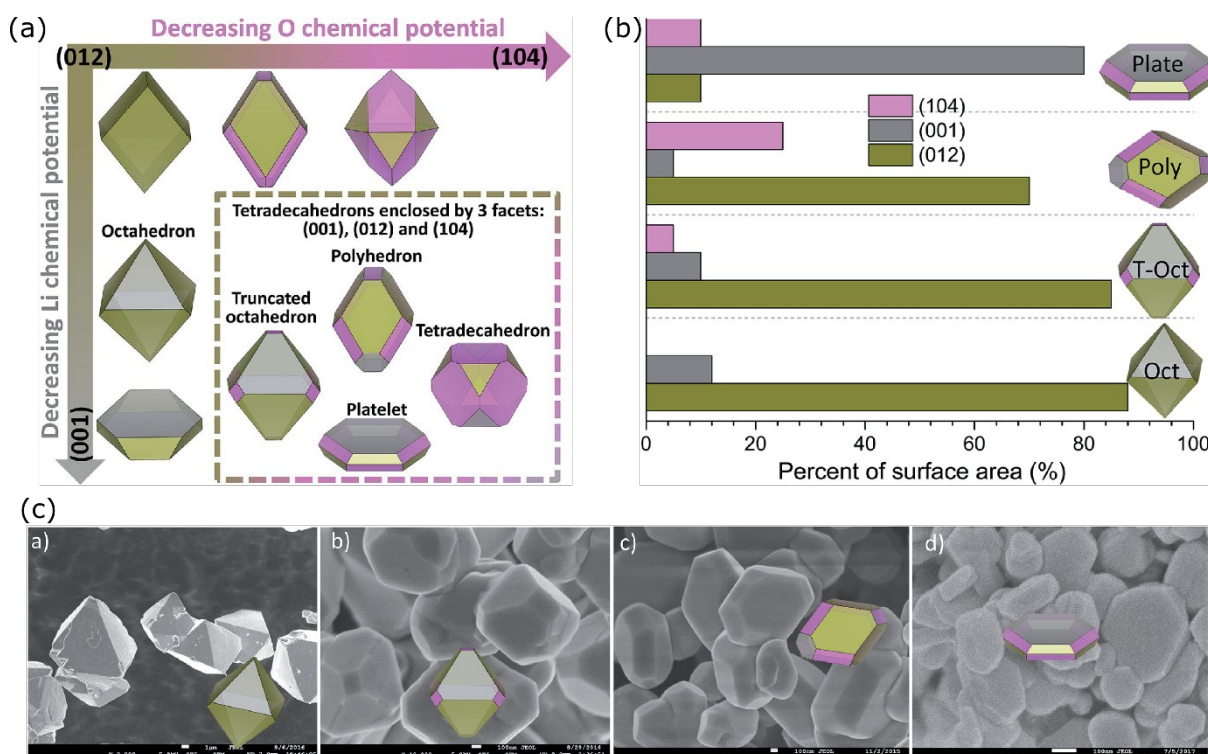
Figure 23. Morphology and facet control of NCM: (a) Dependencies of morphology/facet based on the lithium and oxygen chemical potential of the environment surrounding the crystallites during calcination, and (b) the calculated relative amount of facet exposed in each of the crystal morphology. (c) SEM images of NCM crystallites showing the morphology accessible by tuning the Li/O chemical potential as synthesis parameters, showing from left to right octahedra, truncated octahedra, polyhedra and platelets. Reproduced with permission. [67] Copyright 2019, Royal Society of Chemistry.

The ability to synthesize single crystalline NCM, especially with the type of facet exposed, is a major advance for both applicability and fundamental research. In terms of battery performance, exposing the (001) facet is not expected to promote ionic transport properties, since it is parallel to the transition metal layer and impermeable to Li$^+$ diffusion, but exposure of surfaces that cut across the transition metal layer, such as the (010) facet, would facilitate Li$^+$ exchange with the electrolyte. Indeed, NCM crystals that have greater exposure of these

lithium-transporting surfaces exhibit 10-20% increase in either capacity at high C-rates due to faster Li$^+$ diffusion, or larger overall capacity through increased material utilization.[62, 67] While such performance enhancement has been reported even for polycrystalline NCM exposing the appropriate facets, the results from discrete single crystals can be considered more experimentally rigorous as secondary particle effects are eliminated.[68]

Application of single crystalline NCM for fundamental investigation

From a fundamental perspective, the synthesis of discrete NCM single crystals can facilitate various characterization methods, particularly in unambiguously tracking structural and electronic changes to the material during battery operation so as to elucidate the (electro)chemical mechanisms associated with capacity loss. Several previous investigations using localized characterization techniques on secondary NCM particles illustrate how structural and electronic properties are spatially non-uniform, which can lead to incorrect interpretation of results from bulk-averaged techniques. For example, crystallographic analyses based on electron microscopy carried out by Wang and coworkers on $LiNi_{0.76}Mn_{0.14}Co_{0.10}O_2$ demonstrate that the deleterious phase change and oxygen loss take place primarily at the surfaces in contact with electrolyte, but not at liquid-impenetrable surfaces and grain boundaries of primary particles buried within the aggregate that is the secondary particle.[69] Along similar lines but demonstrating an opposite result, Sun and co-workers measured the electric conductivity of high-nickel NCM secondary particles (composition $LiNi_{0.98}Mn_{0.01}Co_{0.01}O_2$) using the scanning spreading resistance microscopy mode of atomic force microscopy, and found that electric resistivity is greater for the primary particles within the core of the secondary particles as compared to those near the surface.[70] The authors attributed the spatial conductivity difference to lithium deficiency in the core

58

region, in turn leading to greater susceptibility for electrolyte-induced phase transition to the insulating rock salt phase within the interior of the secondary particles. Evidently, the two examples presented here drew conflicting conclusions and may simply be attributed to different NCM compositions, although differences in how primary particles aggregate into secondary particles may also be a factor complicating analyses. Further complications can arise in how primary and secondary particles are commonly designated in the literature, as raised by Lee et al. in their recent electron microscopy investigation.[71] Here, by analyzing the electron diffraction patterns and the grain boundaries at atomic resolution on NCM samples (NCM111 and NCM811), the individual units comprising the secondary particles that have been typically considered to be primary particles were found to be, in fact, composed of several smaller single crystals aligned by oriented attachment, giving the appearance of larger single crystalline primary particles. This finding adds another layer of complexity to the study of NCM crystals, casting doubts on findings related to deterioration mechanism (e.g. whether cracks develop within the crystal grain or at grain boundaries). Hence, synthesizing true single crystals with well-defined morphology in terms of sharp edges and facets at the micro-scale and using them for fundamental investigations can avoid many of the ambiguity associated with secondary particles. Recognizing this, recent investigations on the fundamental aspects of NCM structural evolution during redox cycling have employed single crystalline NCM. Zhu et al. employed platelets of NCM333 and 622, which have >85% of its surface belonging to the (001) face with the remaining being (012) and (104) surfaces as seen in **Figure a**, for investigating whether surface reconstruction from layered to spinel to rocksalt phase is dependent on the crystallographic facet, based on HAADF STEM (high-angle annular dark-field scanning transmission electron microscopy) analyses.[72] The clean interfaces in both NCM samples enabled the authors to visualize this

surface reconstruction exclusively on the non-(001) facet, even in the pristine state (**Figure b**), and that severity of this reconstruction correlates with Ni content. Redox cycling led to growth of this surface reconstruction layer predominantly on the non-(001) facet, with growth greater in the Ni-rich sample, although some growth was also observed in the basal (001) facet to a much lesser extent in both samples (**Figure c**). Similar attempts to elucidate the degradation mechanism were conducted by Zhang et al., employing single crystals of Ni-rich NCM622 in experiments using in operando synchrotron transmission X-ray microscopy and combined x-ray fluorescence microscopy/ptychography, techniques which can spatially resolve not only the elemental distribution within the micron-sized particles but also their valence state. As visualized in **a**, changes within the pristine micron-sized crystal during charge and discharge are initiated and propagated from the surface to the particle interior, as monitored by the Ni K-edge ($Ni^{3+}/^{4+}$ oxidation state), showing complete reversibility only in the first cycle. However, by the 201st cycle, around 50% of the fully charged phase cannot be recovered during discharge, leading to significantly non-uniform valence state across the whole particle. Mapping the elemental distribution corroborates these results as shown in **b**, where the three transition metals originally found to be homogeneous throughout the particle in the pristine state become considerably segregated by the 201st cycle.
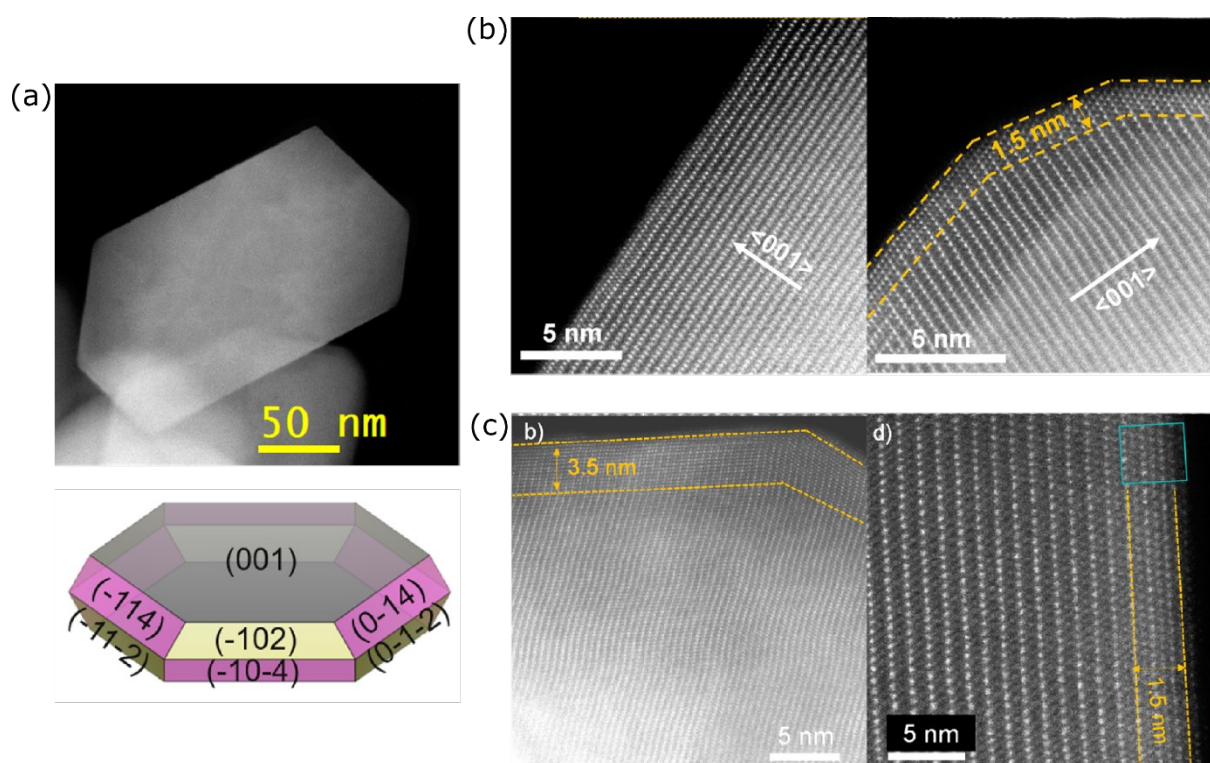
Figure 24. HAADF STEM analyses of NCM622 single crystal: (a) TEM image of a single crystalline NCM622 platelet used for microscopy analyses for tracking structural evolution (top) and a representation of the facet exposed based on crystal morphology (bottom); (b) pristine crystal showing absence of a surface reconstruction layer on the (001) surface (left) while a layer of thickness 1.5 nm was found on the non-(001) surface (right); (c) NCM crystals after 100 cycles in the voltage range 3.0–4.6 V, showing a thicker reconstruction layer of 3.5 nm on the non-(001) surface (left) compared to the thinner layer of thickness 1.5 nm on the (001) surface (right). Reproduced with permission.[72] Copyright 2020, American Chemical Society.
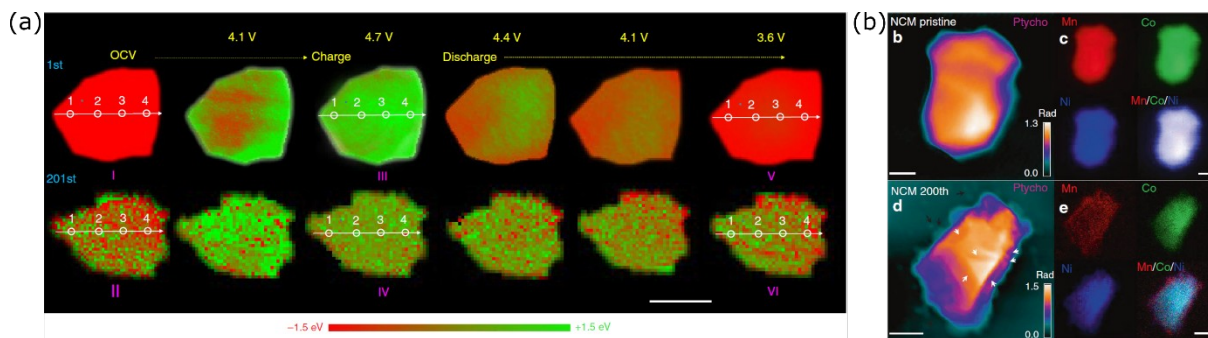
Figure 25. X-ray fluorescence microscopy of NCM622 single crystals: (a) in operando spatial mapping of changes in nickel valence state based on the shift in the Ni *K*-edge line (negative shift in red and positive shift in green refers to reduced and oxidized nickel) during charge and discharge in the pristine state (top) and after 200th cycles (bottom); scale bar in white is 2 μm. (b) X-ray fluoresnce and ptychographic image showing elemental distribution within the pristine state (top) and after 200 charge-discharge cycles (bottom); scale bars in white in the two left panels are 2 μm, while those in the two right panels are 1 μm. Reproduced with permission.[73] Copyright 2020, Springer Nature.

The clarity of these images enabled the authors to visualize the structural and chemical evolution during redox processes, and allowed them to draw convincing conclusions regarding the degradation process, thus highlighting the importance of using suitably crystalline samples for fundamental studies. As the synthesis of micron-sized NCM crystals is refined for better control of both the crystallinity and the facets exposed, we anticipate more sophisticated mechanistic studies to become feasible to advance our understanding the reaction processes during battery operations. Concurrently, we also anticipate improvements in battery performance—in terms of capacity achievable and/or capacity retained at high C-rate—arising from either the intrinsic merits of better quality single crystals, or from

implementing appropriate counter-measures against the performance-limiting processes as elucidated by the aforementioned mechanistic studies.

3.2.3 Extrinsic modification of NCM microstructures

Notwithstanding the merits of having low surface area in micron-sized single crystalline NCM, these oxide materials as ceramics are brittle. Elastic modulus has been measured to be around 200 GPa for NCM333, low enough for particle fracture to occur, and worsened by computation prediction that delithiation further weakens mechanical strength.[74] Hence, their particles can still fracture under mechanical stress, which can originate from several sources, such as during the final calendaring step in the electrode manufacturing process, or accumulation of lattice strain as the crystal expands and contracts over extended redox cycling.[56c, 75] Other performance-deteriorating processes, such as dissolution of transition metal by trace HF in the electrolyte or formation of cathode-electrolyte interfaces as discussed above, are inherent to battery operations and thus inevitable. Nevertheless, as will be discussed in this section, the severity of these deleterious processes can be mitigated to improve battery performance and lifetime, following strategies based on microstructuring of NCM through compositization with suitable materials.

Inorganic microstructure composites

Typically, compositization involves coating the redox-active cathode particles with another material having protective properties. As had already been reviewed elsewhere recently, coating materials such as metal oxides and metal phosphates have been applied using solution- and gas-/vacuum-based techniques, leading indeed to improved capacity retention as an illustration to the success of this strategy in reducing cathode degradation.[76] Less

63

discussed, however, is the oftentimes decrease in initial capacity compared to the uncoated

cathode, which is likely attributed to an increase in dead weight (i.e. extra material mass

without capacity contribution) or decreased material utilization owing to reduced charge

transport kinetics through the coating material. As for the applicability of this strategy, the

additional material and processing costs, especially in the case of vacuum-based methods

such as ALD requiring volatile precursors, make implementation in large-scale

manufacturing difficult. Therefore, the focus in this section will be on practical

compositization routes that are cost-effective and scalable, while delivering enhanced battery

performance through mitigation of cathode deterioration processes.

The aforementioned decrease in capacity associated with an increase in deadweight from

non-redox-active component(s) in the composite motivated Sun and coworkers to pioneer the

concept of nickel concentration gradient in NCM secondary particles.[77] This concept may be

considered as a form of self-coating, whereby the core of each secondary particles is nickel-

rich NCM or even pure $LiNiO_2$ so as to attain high capacity and is covered by a nickel-

deficient and manganese-rich shell (depicted in **a** and **26b**), such that the shell is also redox

active (albeit delivering lower capacity due to reduced nickel content) yet being more

resistant against the deleterious phase transition and electrolyte-related corrosion. The shell

has either a uniform composition or a continuous concentration gradient with increasing

manganese (and decreasing nickel) content towards the surface.[2d, 78] The markedly enhanced

cyclic capacity retention as shown in **c**, however, cannot be solely attributed to this core-shell

microstructure because the shell still has appreciable nickel content (>60% atomic ratio

compared to other transition metals) and would therefore be subjected to deterioration

processes discussed earlier. Analyses by electron microscopy show that the shell comprises

slab-like or columnar crystallites that radiate outward but stacked together along the c-axis, as

depicted in a and 26b. In-depth investigation conducted by Sun and coworkers demonstrated that this unique morphology originates from how the precursor to NCM, the mixed metal hydroxide nominally formulated as $Ni_xCo_yMn_z(OH)_2$, is crystallized and lithiated.[79] Specifically, air-oxidation of the manganese to 3+ yields MnOOH crystallites that have a lattice mismatch with $Ni(OH)_2$, causing this manganese species to segregate and crystallize into a twinned structure interspersed with $Ni(OH)_2$, which itself is also crystallographically aligned with MnOOH (i.e. [h00] zone axis of $Ni(OH)_2$ parallel to [00l] of MnOOH; see **f**). These twinned precursor crystallites radiate outward, and this twinning is preserved after lithiation and calcination to yield the radially aligned columns or slabs in the shell of the NCM particles. As the (003) crystal planes of the slab/column face outward from the spherical particles, this morphology would facilitate lithium diffusion to improve rate performance and/or utilization of active material. However, the most important advantage of this microstructure considered beneficial for capacity retention is the alignment of the slabs/columns along the direction of lattice contraction and expansion during charge and discharge (**d**). Compared to randomly oriented crystallites, the tensile stress induced from lattice changes is homogeneous around the parameter of the spherical particle, as shown in **e**, so as to reduce the likelihood of secondary particle fracture as well as to inhibit the propagation of cracks even if they form, thereby limiting electrolyte infiltration into the particle core and the associated capacity fading mechanism. This protective mechanism is summarized in d.[2d]
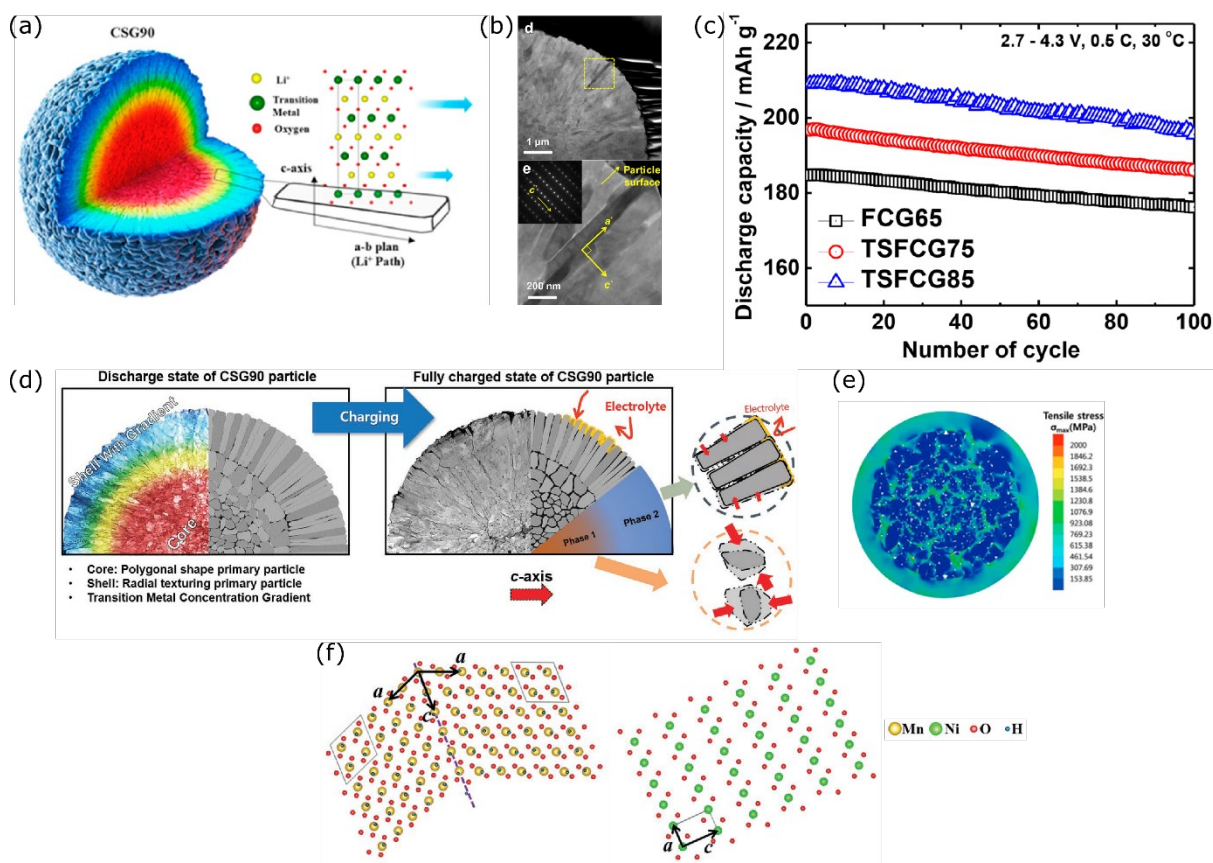
Figure 26. Concentration gradient in coating: (a) Representation of nickel-rich core for high capacity covered by a manganese-rich shell; the shell comprises crystallites with a columnar or slab-like morphology, with lithium diffusion direction radiating from particle center as indicated by the blue arrows; (b) transmission electron microscopy (TEM) images of the columnar/slab-like crystallites comprising the manganese-rich shell; Reproduced with permission.[2d] Copyright 2019, Wiley. (c) discharge capacity upon cycling for core-shell with full concentration gradient (FCG) and with two-sloped full concentration gradient (TSFCG) illustrating excellent capacity retention; Reproduced with permission.[78c] Copyright 2017, American Chemical Society. (d) anticipated advantage of the columnar/slab-like morphology of the shell, showing the lattice expansion upon charge is in the direction around the perimeter of the particle sphere as indicated by red arrows (in contrast to the anisotropic expansion of randomly orientated particles in the core), thereby preventing electrolyte

infiltration; (e) calculated tensile stress showing homogeneous distribution over the shell due to its morphology; (f) atomic structure of twinned MnOOH (left) and crystallographic alignment of Ni(OH)$_2$ (right), showing the [h00] zone axis of the former parallel to [00l] of the latter. Reproduced with permission.[80] Copyright 2018, Wiley.

As evident from the above series of work, while the original intention of using a nickel-deficient shell was to exploit its electrochemical stability, subsequent analyses attribute the improved capacity retention to how certain morphologies can directly alleviate specific degradation mechanisms inherent to NCM.[78a, 81] These results thus exemplify how the microstructure texture can be as important a consideration as chemical composition in terms of cathode material design, hence presenting a strategy for performance enhancement that can be readily implemented in pre-existing manufacturing equipment without compromising the intrinsic performance of the redox-active material.[82]

Composites with carbonaceous materials

In contrast to the aforementioned inorganic coatings, carbon-based or organic compounds for compositization offer another practical alternative. They are lightweight, generally inexpensive, and often can be facilely incorporated into the standard preparation protocols of cathode materials, thus making them a potentially cost-effective solution to improving cycling performance without sacrificing capacity due to excessive increase in electrode mass. Functionally, these materials can facilitate charge transport to the active material and, in turn, improve capacity retention with increasing C-rate. This is especially the case for carbonaceous materials since they have excellent electric conductivity, while polymers may have high ionic conductivity depending on their monomeric constituent. Here, it should be

noted that, NCM already has appreciable electric conductivity as correlated with nickel content, and rises from 10^{-8}–10^{-6} S cm^{-1} in the pristine state to 10^{-3} S cm^{-1} when charged above ~3.8 V, a conductivity increase associated with Ni$^{3+/4+}$ mixed valence (for reference, ionic transport remains at around 10^{-8}–10^{-10} S cm^{-1} across all state of charge).[83] Nevertheless, optimum rate performance in NCM can be attained only when the volume fraction of carbon conductor passes certain threshold values, which depends on the carbon morphology and how it disperses the redox-active NCM.[84] One of the most important advantages of these so-called soft materials is that, in addition to their resistance against HF corrosion, they also have the flexibility and mechanical robustness to withstand repeated lattice changes and structural distortions occurring in the cathode during charge/discharge. This advantage is best illustrated in the work by Yu et al., who prepared flexible and stretchable electrodes comprising alternating layers of carbon nanotubes and NCM111 on a strained polymeric substrate (**Figure a**).[85] Even without using binders, the electrode preserved its mechanical integrity after repeated tensile tests due to strong adhesion between all components based on van der Waals interaction, and retained much of the electrochemical capacity when the electrode was subjected to extensive strain. Full cells (prepared with $Li_4Ti_5O_{12}$ as flexible anode under an identical layer-by-layer procedure) exhibited excellent capacity retention over more than 50 charge-discharge cycles even under tensile strain, as shown in the cycle-capacity plot in **Figure b** and **27c**, thus evidencing the advantage of this carbon allotropes in buffering both internally as well as externally applied structural distortion.
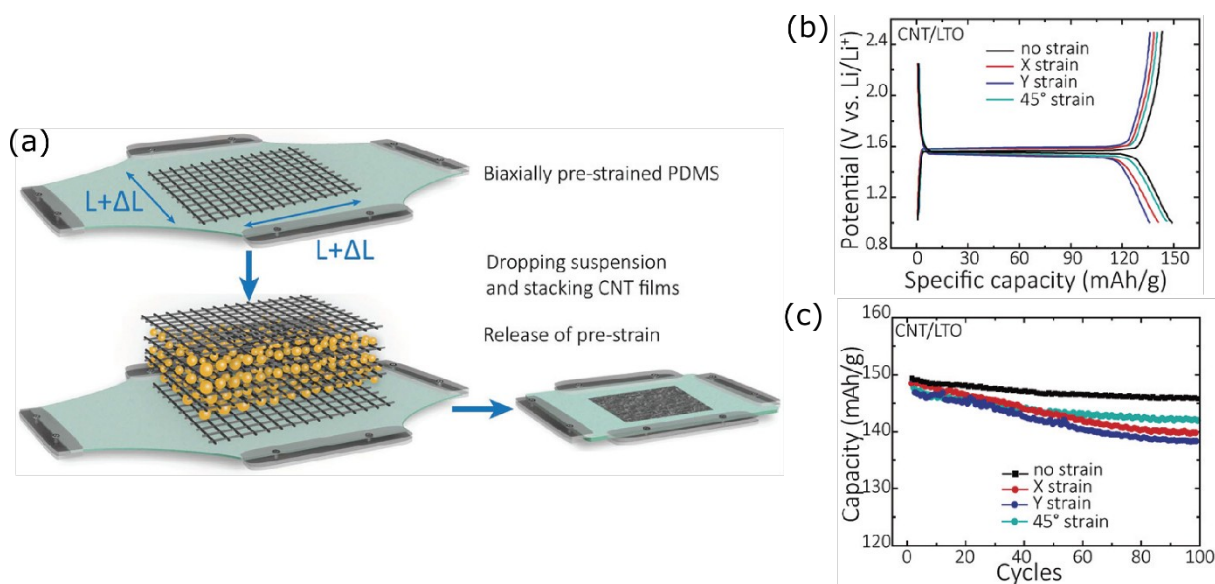
Figure 27. Flexible NCM electrode prepared by composition with carbon nanotube (CNT) to buffer against internally and externally applied structural changes: (a) Depiction of layer-by-layer deposition of alternating stacks of NCM and carbon nanotubes onto a pre-stretched polymeric substrate; (b) galvanic profile of full cell with $Li_4Ti_5O_{12}$ (LTO) showing charge discharge with strain along various directions; (c) capacity retention with cycling when strained along different directions. Reproduced with permission.[85] Copyright 2018, Royal Society of Chemistry.

Miniaturizing the low-dimensional carbon conductor to the nanoscale can provide enhancements in cell performance through improved charge distribution, and applications of nano-structured carbons such as the two-dimensional graphene and the one-dimensional carbon nanotube have been investigated since nearly a decade ago as they become commercially available.[86] In recent developments, composites with increasing structural complexity have been reported aiming to enhance the protection of the cathode materials while retaining the excellent charge transport properties of these nanostructured carbonaceous materials. For example, the addition of both graphene and nanotube to NCM leads to both greater capacity at high C-rate as well as improved capacity retention over extensive cycling

as compared to the unmodified NCM or NCM singly composited with either graphene or nanotube, a performance improvement attributed to graphene acting as a protective albeit imperfect covering against the corrosive processes while the nanotube providing the required charge percolation network.[87] Alternatively, the mechanical advantages of these carbonaceous nanostructures may be exploited to stabilize other rigid coating materials. As a case in point, Yang et al. coated NCM811 with carbon nanotube followed by Li_3PO_4, an inorganic lithium conductor (**Figure a** and **28b**), thereby allowing both electrons and ions to be quickly transported to the cathode material as evidenced by impedance measurements, in turn yielding cells possessing higher capacity at large C-rate as compared to the uncoated and singly-coated counterparts.[88] Most importantly, the nanotubes improve the adhesion of the Li_3PO_4 coating onto the NCM by ameliorating the mechanical stress induced by lattice changes during cycling (**Figure d**). Hence, the NCM with both coatings retained the most capacity under long term cycling as compared to the uncoated NCM and Li_3PO_4-coated NCM. As shown in **Figure c**, under the most aggressive cell test conditions conducted by the authors, using a cycling window of 3.0–4.5 V at 55 °C with 0.5 C current, doubly coated nanotube-Li_3PO_4-NCM retained 60.8% capacity after 500 cycles, as compared to 28.3% of uncoated NCM and 41.2% when NCM is coated with only Li_3PO_4. These results further exemplify the effectiveness of these carbon nano-materials especially in maintaining the structural integrity of composites, including multi-component architectures such as core-shell/coating particles, by buffering volume changes during redox cycling.
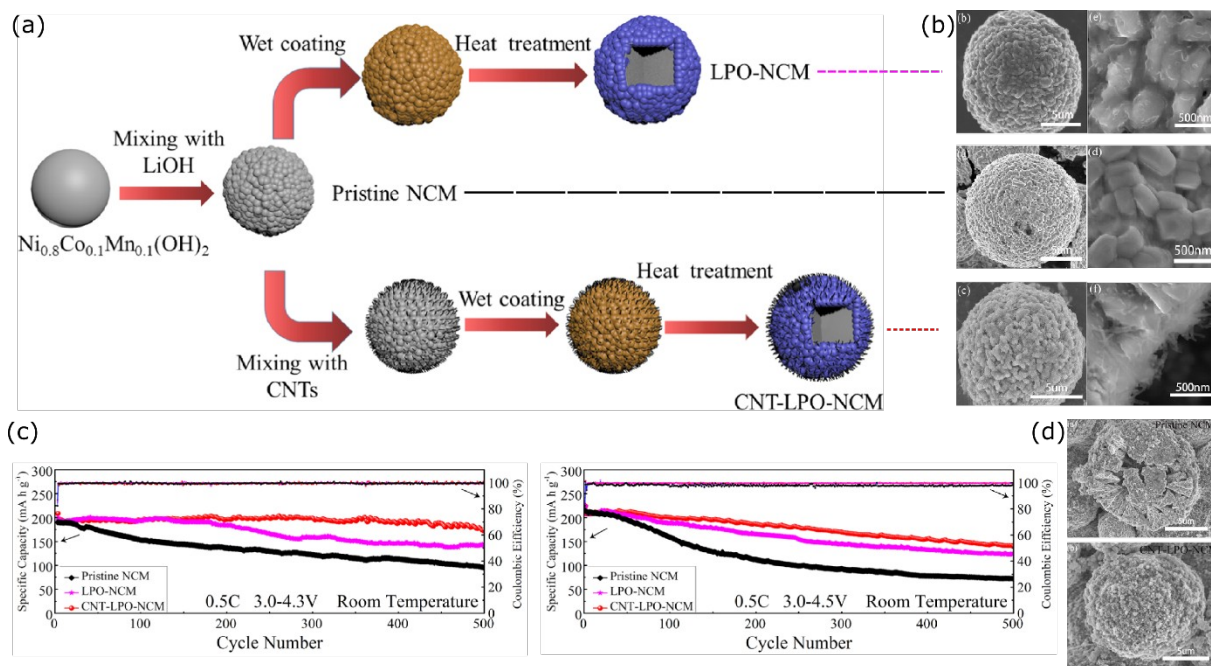
Figure 28. Coating of NCM with carbon nanotube (CNT) and the Li^+ conductor Li_3PO_4 (LPO): (a) synthesis routes to pristine NCM, NCM coated with only LPO (LPO-NCM) and with both CNT and LPO (CNT-LPO-NCM); (b) corresponding scanning electron microscopy (SEM) images of (from top to bottom) LPO-NCM, pristine NCM811 and CNT-LPO-NCM; (c) capacity retention upon cycling with a voltage upper limit of 4.3 V (left) and 4.5 V (right); (d) SEM images of after cycling showing extensive fracture in pristine NCM (top) compared

to the structurally integrity CNT-LPO-NCM. Reproduced with permission.[88] Copyright 2019, American Chemical Society.

Composites with polymers

Other than the aforementioned carbon allotropes, polymers are another class of carbon-based material suitable as protective coating, given that they have similar advantages in terms of flexibility for buffering cathode volume change, chemical stability against the corrosive HF, and are lightweight and cost-effectiveness. Provided that the coating thickness is optimized for protective coverage and structural integrity without significantly impeding charge transport, polymer-coated NCM generally display capacity stability over long term cycling.[89] One further advantage unique to polymers (but not available for carbonaceous and inorganic materials) is that tailoring the molecular structure of their monomeric constituent(s) may confer various functions in addition to the aforementioned chemical protection and mechanical stabilization. As one example illustrating the type of functionality feasible, Han et al. identified the inexpensive polymer poly(methyl methacrylate) to be an effective coating material for NCM811 due to the presence of the ester groups, which coordinate to the surface metal species to lower their mobility and prevent their dissolution, an effect most prominent for nickel, in turn leading to enhanced capacity retention over extensive cycling.[90] In another example, Gan et al. employed polyvinylpyrrolidone (PVP) in conjunction with the electrically conducting polyaniline (PANI) to coat NCM811.[91] Here, due to the inadequate interaction between NCM particles and polyaniline which would have led to segregation of the two, PVP was used to exploit as a bridge, whereby its carbonyl groups form both hydrogen bonds with the PANI and dative bonds with surface metals on the NCM particles, yielding a thin and uniform coating on the cathode material. As a result of having both an

electrically conductive and protective coating layer, the modified NCM811 exhibited superior capacity retention both at high C-rate and over extensive cycling, as compared to the uncoated and the singly coated counterparts.

As implied in the last example, in addition to polymer selection, the coating method is another point of consideration as it affects the dispersity, uniformity, and adherence of the coating material on the cathode particles, thus also affecting whether all benefits of the coating material can be derived. Since the NCM cathode compounds are typically aggregates of primary particles, it is uncertain whether coating over such secondary particles is sufficient to inhibit the degradation processes or whether protection over individual primary particles is necessary.[92] The latter is far more challenging to realize especially in solution-based coating method, since the coating material (or cursor to the coating material) generally cannot penetrate into the sub-micron inter-particulate pores, presumably due to (but seldomly discussed in the literature) the surface tension of the coating solution and/or the large molecular size of the coating material/precursor inclusive of the solvation shell. On the other hand, penetrative coatings are feasible when using gas/vacuum-based deposition, such as chemical vapor deposition (CVD) or atomic layer deposition (ALD). The success of vacuum-based approach was recently demonstrated by Xu et al. for polymer-coated NCM111.[93] Here, the authors coated the cathode particles with poly(3,4-ethylenedioxythiophene), a well-documented polymer with both electric and ionic conductivity, by in situ polymerization of the monomer based on CVD under vacuum ($\approx$ 40 Pa) as illustrated in **Figure a** and **29b**. This process yielded a thin coating over the primary particles in the aggregate, even those in the inner part of the secondary aggregates (**Figure c**). These PEDOT-coated NCM exhibited a capacity retention of over 90% after 100 cycles at an upper voltage limit of 4.3 V for $LiNi_{0.85}Co_{0.1}Mn_{0.05}O_2$ or after 50 cycles at 4.8 V for $Li_{1.2}Ni_{0.13}Co_{0.13}Mn_{0.54}O_2$ (versus $\approx$ 54% of

the uncoated NCM in either upper voltage limit), as shown in **Figure d**, an outperformance that the authors experimentally demonstrated to be attributable to minimizing metal dissolution, preventing gas release, and enhancing the structural reversibility upon lithiation/delithiation cycles. Notwithstanding these excellent results, implementing such gas-/vacuum-based coating process faces issues related to scaling up for ton-scale production as well as environmental concerns in using volatile and often hazardous precursors (as in the above example, which used the toxic $VOCl_3$ as an oxidative initiator for PEDOT polymerization). Furthermore, as alluded to previously, the benefits of penetrative coating are not sufficiently established and questions remain as to whether similar performance metrics are obtainable by circumventing such gas-/vacuum-based procedures with simpler and safer solution processing. This is exemplified by the publications of Kim and co-workers, who employed a copolymer of PEDOT and poly(ethylene glycol) (PEG) for coating NCM622, either as a single component coating obtained by a solution-based process, or co-deposited together with alumina nanoparticles following a sequential dry- and wet-coating method to yield a hierarchal Al_2O_3-polymer coating.[94] These PEDOT-PEG copolymer-coated cathodes have capacity retention of over 90% after 100 cycles with a voltage limit of 4.3 V as similar to the above example, an improvement in capacity retention that can also be experimentally attributed to the PEDOT-PEG inhibiting metal dissolution and gas evolution. It is noteworthy to remind the readers here that the authors achieved similar metrics for capacity retention using NCM622 (c.f. NCM111 used in the ALD-based PEDOT deposition in the previous example), and that NCM622 is a more demanding system considering the greater severity of deterioration processes in nickel-rich cathodes.
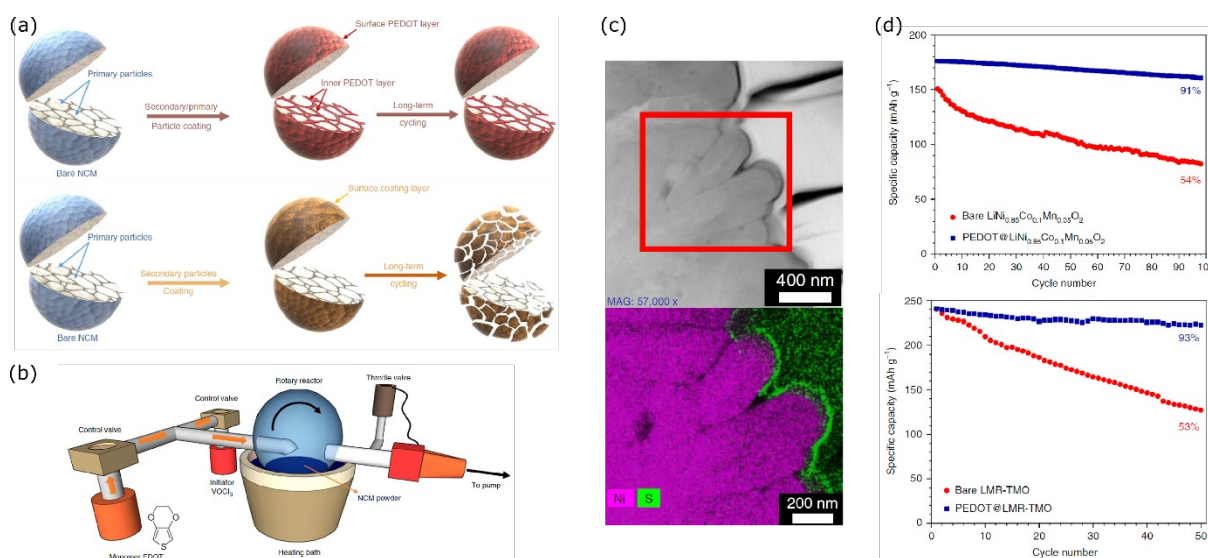
Figure 29. Polymeric coverage of primary particles by CVD: (a) anticipated advantage of conformal coating over primary particles even those within the interior of the secondary particle, illustrating minimal fracture over long term cycling (top), compared to particle fracture if coating is only over the secondary particle (bottom); (b) apparatus used for CVD deposition showing injection of the monomer and the vanadium-based oxidizer for in situ polymerization over NCM (c) HAADF STEM image and the corresponding elemental mapping by energy dispersive spectroscopy showing the thin homogeneous PEDOT coating; (d) capacity retention upon cycling for uncoated and PEDOT-coated NCM samples with the upper voltage limit of 4.3 V for $LiNi_{0.85}Co_{0.1}Mn_{0.05}O_2$ (top) and 4.8 V for Li-rich $Li_{1.2}Ni_{0.13}Co_{0.13}Mn_{0.54}O_2$ (bottom). Reproduced with permission.[93] Copyright 2019, Springer Nature.

In light of these recent developments on coating microstructures, one research direction in the future should be to clarify whether coating over individual primary particles is necessary, or if coating over the secondary aggregates will suffice in enhancing the cell performance of NCM cathode materials. On the one hand, sufficiently adhesive and homogeneous coatings

with thickness controllable down to tens of nanometers are accessible through wet-chemistry techniques. In oxidized oxygen point of view, the major role of the coating on the material act as a protection layer preventing the direct contact of labile oxygen with the electrolyte. The oxidized surface oxygens at the cathode-electrolyte interfaces are extremely labile so that easily react to form oxygen gas or by-products, the irreversible oxygen oxidation is expected to be reduced. In spite of the simplicity and cost-effectiveness of these solution-based methods, the level of protection against cathode degradation processes is seemingly close to or on par with those prepared by gas-/vacuum-based techniques, as assessed by battery performance metrics. To further narrow any performance gap between solution-based and gas-/vacuum-based coating techniques, specific areas for future research include the selection of coating materials, modification of functional groups to confer specific properties, as well as optimization of deposition in terms of solution parameters. Given that solution processing is economical and straightforward to implement, this research direction has the advantage in that it can be immediately and facilely transferred to an industrial-scale setting. On the other hand, gas-/vacuum-based methods such as CVD and ALD provide coatings with unparalleled control over homogeneity and thickness, sometimes down to unit cell resolution. Hence, they are essential for uniformly coating substrates with sub-micron asperities, and will be especially applicable if protection of individual primary particles in the secondary aggregates were found to be necessary to achieve complete, long-term protection against cathode deterioration. In recognizing these benefits of ALD and CVD, advances in this direction aims to scale up these coating methods. A specific case in point is the recently developed spatial atomic layer deposition method, a specific type of ALD that can in principle be integrated into the ton-scale manufacturing of battery electrodes.[95] Further research at the fundamental and technical level into the mechanism of degradation and protection as well as process

development will be necessary to resolve which of the two divergent routes is most appropriate for continual enhancement of battery performance in the context of scalable production.

4. Summary and Outlook

As the practical capacities of conventional layered oxides are reaching their theoretical limits, the current impetus in battery research is to derive further capacity by utilizing the reversible redox reaction of the lattice oxygen to meet the demand of the increasing energy density target. To utilize the oxygen redox center, a detailed understanding of its underlying mechanism will be instrumental for improving its reversibility as well as to mitigate the myriad of degradative processes associated directly and indirectly with the electrochemical oxygen oxidation/reduction, for example, the voltage hysteresis, the TM migration, the voltage fade, the irreversible phase transition and the oxygen loss. The complexity of this redox reaction, however, has introduced various misconceptions, poorly formulated definitions, and controversial models on its mechanistic aspects, which we sought to summarize and discuss in this review based on recent developments. While most reports and discussions revolve around Li-rich materials, we note that oxygen redox reaction takes place in a variety of conventional layered cathodes too, indicating the urgent need of clarifications on the fundamental mechanism of oxygen redox reactions that remain a highly debated topic in battery field. Practically, various strategies targeting modifications of the oxide at the atomic, surficial and microstructure scales that have been successfully implemented in alkali-rich layered oxides were found to be promising in enhancing the battery performance of their conventional (i.e. non-alkali-rich) counterparts performance too at operating conditions where oxygen redox becomes prevalent. This is in spite of the different redox centers in these

two classes of materials, and is irrespective of whether or not the aforementioned strategies were aimed at stabilizing oxygen redox reactions. Indeed, as demonstrated in the examples reviewed here, there is no single approach for alleviating the harmful processes associated with the oxygen oxidation. Therefore, a combinational approach in the form of hierarchal material, from atomic to microstructure scale, is likely required to fully harness the power and benefit of the oxygen redox center. The appropriateness of each approach (or combination thereof) will need to be critically assessed while our understanding of oxygen redox evolves. Through the reviews and comparisons in this work, we show that a fundamental mechanism of the oxygen redox reaction, which could interpret a variety of reliable characterization results in different classes of materials, is yet to be achieved. Additionally, many fundamental questions remain, e.g., the low kinetics of oxygen redox reaction in most materials, the voltage fade that seems to be associated with irreversible oxygen oxidation, the oxygen loss pathway, the relationship between the oxygen loss and lattice oxygen redox, and the effects from both TMs and oxygen unhybridized states on the oxygen activities. With the advances of modern experimental and theoretical techniques, we optimistically expect a better understanding of this enigmatic redox reaction, which will lead to better controls of the oxygen redox reaction towards a much improved energy storage system with high energy density.

Acknowledgements

References

[1]   a) J. Goodenough, *Prog. Solid. State Ch.* **1971**, 5, 145; b) A. Manthiram, *Nat. Commun.* **2020**, 11; c) K. Mizushima, P. C. Jones, P. J. Wiseman, J. B. Goodenough, *Mater. Res. Bull.* **1980**, 15, 783.

[2]   a) W. Lee, S. Muhammad, C. Sergey, H. Lee, J. Yoon, Y. M. Kang, W. S. Yoon, *Angew. Chem. Int. Ed.* **2020**, 59, 2578; b) Z. Zhu, D. Yu, Y. Yang, C. Su, Y. Huang, Y. Dong, I. Waluyo, B. Wang, A. Hunt, X. Yao, J. Lee, W. Xue, J. Li, *Nat. Energy* **2019**, 4, 1049; c) M. Kim, M. Jeong, W.-S. Yoon, B. Kang, *Energy Environ. Sci.* **2020**, DOI: 10.1039/d0ee02518f; d) U. H. Kim, H. H. Ryu, J. H. Kim, R. Mucke, P. Kaghazchi, C. S. Yoon, Y. K. Sun, *Adv. Energy Mater.* **2019**, 9, 1803902; e) L. Liang, W. Zhang, F. Zhao, D. K. Denis, F. u. Zaman, L. Hou, C. Yuan, *Adv. Mater. Interfaces* **2019**, 7, 1901749; f) S. H. Min, M. R. Jo, S.-Y. Choi, Y.-I. Kim, Y.-M. Kang, *Adv. Energy Mater.* **2016**, 6; g) Y. Jiang, Z. Liu, Y. Zhang, H. Hu, X. Teng, D. Wang, P. Gao, Y. Zhu, *Electrochim. Acta* **2019**, 309, 74; h) J. Alvarado, C. Wei, D. Nordlund, T. Kroll, D. Sokaras, Y. Tian, Y. Liu, M. M. Doeff, *Mater. Today* **2019**, DOI: 10.1016/j.mattod.2019.11.009; i) S. Kim, W. Cho, X. Zhang, Y. Oshima, J. W. Choi, *Nat. Commun.* **2016**, 7.

[3]   a) X. Wang, G. Liu, T. Iwao, M. Okubo, A. Yamada, **2014**, 118, 2970; b) N. Yabuuchi, S. Komaba, *Sci. Technol. Adv. Mater.* **2014**, 15, 043501; c) B. Mortemard De Boisse, G. Liu, J. Ma, S. I. Nishimura, S. C. Chung, H. Kiuchi, Y. Harada, J. Kikkawa, Y. Kobayashi, M. Okubo, A. Yamada, *Nat. Commun.* **2016**, 7; d) D.-H. Seo, J. Lee, A. Urban, R. Malik, S. Kang, G. Ceder, *Nat. Chem.* **2016**, 8, 692; e) Y. Xie, M. Saubanère, M. L. Doublet, *Energy Environ. Sci.* **2017**, 10, 266; f) Q. Jacquet, A. Iadecola, M. Saubanère, H. Li, E. J. Berg, G. Rousse, J. Cabana, M.-L. Doublet, J.-M. Tarascon, *J. Am. Chem. Soc.* **2019**, 141, 11452; g) N. Kuganathan, E. Sgourou, Y. Panayiotatos, A. Chroneos, *Energies* **2019**, 12, 1329; h) N. Li, S. Sallis, J. K. Papp, J. Wei, B. D. McCloskey, W. Yang, W. Tong, *ACS Energy Lett.* **2019**, 4, 2836; i) M. Jia, Y. Qiao, X. Li, F. Qiu, X. Cao, P. He, H. Zhou, *ACS Appl. Mater. Interfaces* **2020**, 12, 851; j) W. Zhang, Y. Sun, H. Deng, J. Ma, Y. Zeng, Z. Zhu, Z. Lv, H. Xia, X. Ge, S. Cao, Y. Xiao, S. Xi, Y. Du, A. Cao, X. Chen, *Adv. Mater.* **2020**, 32.

[4]   J. M. Tarascon, G. Vaughan, Y. Chabre, L. Seguin, M. Anne, P. Strobel, G. Amatucci, *J. Solid State Chem.* **1999**, 147, 410.

[5]   a) G. H. Lee, J. Wu, D. Kim, K. Cho, M. Cho, W. Yang, Y. M. Kang, *Angew. Chem. Int. Ed.* **2020**, 59, 8681; b) Z. W. Lebens-Higgins, N. V. Faenza, M. D. Radin, H. Liu, S. Sallis, J. Rana, J. Vinckeviciute, P. J. Reeves, M. J. Zuba, F. Badway, N. Pereira, K. W. Chapman, T.-L. Lee, T. Wu, C. P. Grey, B. C. Melot, A. Van Der Ven, G. G. Amatucci, W. Yang, L. F. J. Piper, *Mater. Horiz.* **2019**, 6, 2112.

[6]   a) Y. Zhao, J. Liu, S. Wang, R. Ji, Q. Xia, Z. Ding, W. Wei, Y. Liu, P. Wang, D. G. Ivey, *Adv. Funct. Mater* **2016**, 26, 4760; b) X. Ding, D. Luo, J. Cui, H. Xie, Q. Ren, Z. Lin, *Angew. Chem. Int. Ed.* **2020**, 59, 7778; c) T. Lin, T. U. Schulli, Y. Hu, X. Zhu, Q. Gu, B. Luo, B. Cowie, L. Wang, *Adv. Funct. Mater* **2020**, DOI: 10.1002/adfm.201909192.

[7]   a) D. Eum, B. Kim, S. J. Kim, H. Park, J. Wu, S.-P. Cho, G. Yoon, M. H. Lee, S.-K. Jung, W. Yang, W. M. Seong, K. Ku, O. Tamwattana, S. K. Park, I. Hwang, K. Kang, *Nat. Mater.* **2020**, 19, 419; b) J. Wu, Z. Zhuo, X. Rong, K. Dai, Z. Lebens-Higgins, S. Sallis, F. Pan, L. F. J. Piper, G. Liu, Y.-D. Chuang, Z. Hussain, Q. Li, R. Zeng, Z.-X.

Shen, W. Yang, *Sci. Adv.* **2020**, 6, eaaw3871; c) R. A. House, U. Maitra, M. A. Pérez-Osorio, J. G. Lozano, L. Jin, J. W. Somerville, L. C. Duda, A. Nag, A. Walters, K.-J. Zhou, M. R. Roberts, P. G. Bruce, *Nature* **2020**, 577, 502.

[8]   a) H. Koga, L. Croguennec, M. Menetrier, K. Douhil, S. Belin, L. Bourgeois, E. Suard, F. Weill, C. Delmas, *J. Electrochem. Soc.* **2013**, 160, A786; b) M. Sathiya, K. Ramesha, G. Rousse, D. Foix, D. Gonbeau, A. S. Prakash, M. L. Doublet, K. Hemalatha, J. M. Tarascon, *Chem. Mater.* **2013**, 25, 1121; c) M. Sathiya, G. Rousse, K. Ramesha, C. P. Laisa, H. Vezin, M. T. Sougrati, M. L. Doublet, D. Foix, D. Gonbeau, W. Walker, A. S. Prakash, M. Ben Hassine, L. Dupont, J. M. Tarascon, *Nat. Mater.* **2013**, 12, 827; d) A. Dunst, V. Epp, I. Hanzu, S. A. Freunberger, M. Wilkening, *Energy Environ. Sci.* **2014**, 7, 2739; e) H. Koga, L. Croguennec, M. Ménétrier, P. Mannessiez, F. Weill, C. Delmas, S. Belin, *J. Phys. Chem. C* **2014**, 118, 5700; f) E. Salager, V. Sarou-Kanian, M. Sathiya, M. Tang, J.-B. Leriche, P. Melin, Z. Wang, H. Vezin, C. Bessada, M. Deschamps, J.-M. Tarascon, *Chem. Mater.* **2014**, 26, 7009; g) E. McCalla, A. M. Abakumov, M. Saubanère, D. Foix, E. J. Berg, G. Rousse, M. L. Doublet, D. Gonbeau, P. Novák, G. Van Tendeloo, R. Dominko, J. M. Tarascon, *Science* **2015**, 350, 1516; h) E. McCalla, A. S. Prakash, E. Berg, M. Saubanère, A. M. Abakumov, D. Foix, B. Klobes, M. T. Sougrati, G. Rousse, F. Lepoivre, S. Mariyappan, M. L. Doublet, D. Gonbeau, P. Novak, G. Van Tendeloo, R. P. Hermann, J. M. Tarascon, *J. Electrochem. Soc.* **2015**, 162, A1341; i) N. Yabuuchi, M. Takeuchi, M. Nakayama, H. Shiiba, M. Ogawa, K. Nakayama, T. Ohta, D. Endo, T. Ozaki, T. Inamasu, K. Sato, S. Komaba, *Proc. Natl. Acad. Sci. U.S.A* **2015**, 112, 7650; j) C. Delmas, *Nat. Chem.* **2016**, 8, 641; k) A. Grimaud, W. T. Hong, Y. Shao-Horn, J. M. Tarascon, *Nat. Mater.* **2016**, 15, 121; l) K. Luo, M. R. Roberts, N. Guerrini, N. Tapia-Ruiz, R. Hao, F. Massel, D. M. Pickup, S. Ramos, Y.-S. Liu, J. Guo, A. V. Chadwick, L. C. Duda, P. G. Bruce, *J. Am. Chem. Soc.* **2016**, 138, 11211; m) K. Luo, M. R. Roberts, R. Hao, N. Guerrini, D. M. Pickup, Y.-S. Liu, K. Edström, J. Guo, A. V. Chadwick, L. C. Duda, P. G. Bruce, *Nat. Chem.* **2016**, 8, 684; n) Y. Nanba, T. Iwao, B. M. D. Boisse, W. Zhao, E. Hosono, D. Asakura, H. Niwa, H. Kiuchi, J. Miyawaki, Y. Harada, M. Okubo, A. Yamada, **2016**, 28, 1058.

[9]   a) P. Rozier, M. Sathiya, A. R. Paulraj, D. Foix, T. Desaunay, P. L. Taberna, P. Simon, J. M. Tarascon, *Electrochem. Comm.* **2015**, 53, 29; b) M. Sathiya, A. M. Abakumov, D. Foix, G. Rousse, K. Ramesha, M. Saubanère, M. L. Doublet, H. Vezin, C. P. Laisa, A. S. Prakash, D. Gonbeau, G. Vantendeloo, J. M. Tarascon, *Nat. Mater.* **2015**, 14, 230; c) G. Assat, A. Iadecola, C. Delacourt, R. Dedryvère, J. M. Tarascon, *Chem. Mater.* **2017**, 29, 9714; d) P. E. Pearce, A. J. Perez, G. Rousse, M. Saubanère, D. Batuk, D. Foix, E. McCalla, A. M. Abakumov, G. Van Tendeloo, M. L. Doublet, J. M. Tarascon, *Nat. Mater.* **2017**, 16, 580; e) P. E. Pearce, G. Assat, A. Iadecola, F. Fauth, R. Dedryvère, A. Abakumov, G. Rousse, J. M. Tarascon, *J. Phys. Chem. C* **2020**, 124, 2771.

[10]   a) M. M. Thackeray, S.-H. Kang, C. S. Johnson, J. T. Vaughey, R. Benedek, S. A. Hackney, *J. Mater. Chem.* **2007**, 17; b) M. H. Rossouw, M. M. Thackeray, *Mater. Res. Bull.* **1991**, 26, 463; c) J. Kim, C. S. Johnson, M. M. Thackeray, *Electrochem. Comm.* **2002**, 4, 205.

[11]   M. Saubanère, E. McCalla, J. M. Tarascon, M. L. Doublet, *Energy Environ. Sci.* **2016**, 9, 984.

[12]   X. Rong, J. Liu, E. Hu, Y. Liu, Y. Wang, J. Wu, X. Yu, K. Page, Y.-S. Hu, W. Yang, H.

Li, X.-Q. Yang, L. Chen, X. Huang, *Joule* **2018**, 2, 125.

[13]   J. Hong, W. E. Gent, P. Xiao, K. Lim, D.-H. Seo, J. Wu, P. M. Csernica, C. J. Takacs, D. Nordlund, C.-J. Sun, K. H. Stone, D. Passarello, W. Yang, D. Prendergast, G. Ceder, M. F. Toney, W. C. Chueh, *Nat. Mater.* **2019**, 18, 256.

[14]   H. H. Eysel, S. Thym, *Z. Anorg. Allg. Chem.* **1975**, 411, 97.

[15]   M. Okubo, A. Yamada, *ACS Appl. Mater. Interfaces* **2017**, 9, 36463.

[16]   M. Ben Yahia, J. Vergnet, M. Saubanere, M. L. Doublet, *Nat. Mater.* **2019**, 18, 496.

[17]   B. Mortemard de Boisse, S.-i. Nishimura, E. Watanabe, L. Lander, A. Tsuchimoto, J. Kikkawa, E. Kobayashi, D. Asakura, M. Okubo, A. Yamada, *Adv. Energy Mater.* **2018**, 8.

[18]   a) W. Yang, T. P. Devereaux, *J. Power Sources* **2018**, 389, 188; b) S. Roychoudhury, R. Qiao, Z. Zhuo, Q. Li, Y. Lyu, J. H. Kim, J. Liu, E. Lee, B. J. Polzin, J. Guo, S. Yan, Y. Hu, H. Li, D. Prendergast, W. Yang, *Energy Environ. Mater.* **2020**, DOI: 10.1002/eem2.12119.

[19]   W. E. Gent, I. I. Abate, W. Yang, L. F. Nazar, W. C. Chueh, *Joule* **2020**, DOI: 10.1016/ j.joule.2020.05.004.

[20]   S. Ahmed, M. Bianchini, A. Pokle, M. S. Munde, P. Hartmann, T. Brezesinski, A. Beyer, J. Janek, K. Volz, *Adv. Energy Mater.* **2020**, 10, 2001026.

[21]   P. Yan, J. Zheng, Z.-K. Tang, A. Devaraj, G. Chen, K. Amine, J.-G. Zhang, L.-M. Liu, C. Wang, *Nat. Nanotechnol.* **2019**, 14, 602.

[22]   W. E. Gent, K. Lim, Y. Liang, Q. Li, T. Barnes, S.-J. Ahn, K. H. Stone, M. McIntire, J. Hong, J. H. Song, Y. Li, A. Mehta, S. Ermon, T. Tyliszczak, D. Kilcoyne, D. Vine, J.-H. Park, S.-K. Doo, M. F. Toney, W. Yang, D. Prendergast, W. C. Chueh, *Nat. Commun.* **2017**, 8.

[23]   S. Lee, W. Jin, S. H. Kim, S. H. Joo, G. Nam, P. Oh, Y. K. Kim, S. K. Kwak, J. Cho, *Angew. Chem. Int. Ed.* **2019**, 58, 10478.

[24]   J. G. Lozano, G. T. Martinez, L. Jin, P. D. Nellist, P. G. Bruce, *Nano Lett.* **2018**, 18, 6850.

[25]   a) Z. N. Taylor, A. J. Perez, J. A. Coca-Clemente, F. Braga, N. E. Drewett, M. J. Pitcher, W. J. Thomas, M. S. Dyer, C. Collins, M. Zanella, T. Johnson, S. Day, C. Tang, V. R. Dhanak, J. B. Claridge, L. J. Hardwick, M. J. Rosseinsky, *J. Am. Chem. Soc.* **2019**, 141, 7333; b) Y. Qiao, S. Guo, K. Zhu, P. Liu, X. Li, K. Jiang, C.-J. Sun, M. Chen, H. Zhou, *Energy Environ. Sci.* **2018**, 11, 299; c) X. Li, Y. Qiao, S. Guo, Z. Xu, H. Zhu, X. Zhang, Y. Yuan, P. He, M. Ishida, H. Zhou, *Adv. Mater.* **2018**, 30, 1705197.

[26]   a) U. Maitra, R. A. House, J. W. Somerville, N. Tapia-Ruiz, J. G. Lozano, N. Guerrini, R. Hao, K. Luo, L. Jin, M. A. Pérez-Osorio, F. Massel, D. M. Pickup, S. Ramos, X. Lu, D. E. McNally, A. V. Chadwick, F. Giustino, T. Schmitt, L. C. Duda, M. R. Roberts, P. G. Bruce, *Nat. Chem.* **2018**, 10, 288; b) R. A. House, U. Maitra, L. Jin, J. G. Lozano, J. W. Somerville, N. H. Rees, A. J. Naylor, L. C. Duda, F. Massel, A. V. Chadwick, S. Ramos, D. M. Pickup, D. E. McNally, X. Lu, T. Schmitt, M. R. Roberts, P. G. Bruce, *Chem. Mater.* **2019**, 31, 3293; c) Z. W. Lebens-Higgins, J. Vinckeviciute, J. Wu, N. V. Faenza, Y. Li, S. Sallis, N. Pereira, Y. S. Meng, G. G. Amatucci, A. V. Der Ven, W. Yang, L. F. J. Piper, *J. Phys. Chem. C* **2019**, 123, 13201.

[27]   G. Assat, A. Iadecola, D. Foix, R. Dedryvere, J. M. Tarascon, *ACS Energy Lett.* **2018**, 3, 2721.

[28]   Z. W. Lebens-Higgins, H. Chung, M. J. Zuba, J. Rana, Y. Li, N. V. Faenza, N. Pereira,

B. D. McCloskey, F. Rodolakis, W. Yang, M. S. Whittingham, G. G. Amatucci, Y. S. Meng, T.-L. Lee, L. F. J. Piper, *J. Phys. Chem. Lett.* **2020**, 11, 2106.

[29] M. P. Seah, W. A. Dench, *Surface and Interface Analysis* **1979**, 1, 2.

[30] F. M. F. De Groot, M. Grioni, J. C. Fuggle, J. Ghijsen, G. A. Sawatzky, H. Petersen, *Phys. Rev. B* **1989**, 40, 5715.

[31] a) Z. Zhuo, Y.-S. Liu, J. Guo, Y.-D. Chuang, F. Pan, W. Yang, *J. Phys. Chem. Lett.* **2020**, 11, 2618; b) Z. Zhuo, C. D. Pemmaraju, J. Vinson, C. Jia, B. Moritz, I. Lee, S. Sallies, Q. Li, J. Wu, K. Dai, Y.-D. Chuang, Z. Hussain, F. Pan, T. P. Devereaux, W. Yang, *J. Phys. Chem. Lett.* **2018**, 9, 6378.

[32] J. Wu, Y. Yang, W. Yang, *Dalton Trans.* **2020**, DOI: 10.1039/d0dt01782e.

[33] K. Dai, J. Wu, Z. Zhuo, Q. Li, S. Sallis, J. Mao, G. Ai, C. Sun, Z. Li, W. E. Gent, W. C. Chueh, Y.-D. Chuang, R. Zeng, Z.-X. Shen, F. Pan, S. Yan, L. F. J. Piper, Z. Hussain, G. Liu, W. Yang, *Joule* **2019**, 3, 518.

[34] J. Wu, Q. Li, S. Sallis, Z. Zhuo, W. E. Gent, W. C. Chueh, S. Yan, Y.-d. Chuang, W. Yang, *J. Phys. Condens. Matter* **2019**, 4.

[35] W. Yin, A. Grimaud, G. Rousse, A. M. Abakumov, A. Senyshyn, L. Zhang, S. Trabesinger, A. Iadecola, D. Foix, D. Giaume, J. M. Tarascon, *Nat. Commun.* **2020**, 11.

[36] X. Rong, E. Hu, Y. Lu, F. Meng, C. Zhao, X. Wang, Q. Zhang, X. Yu, L. Gu, Y. S. Hu, H. Li, X. Huang, X. Q. Yang, C. Delmas, L. Chen, *Joule* **2019**, 3, 503.

[37] G. Assat, J. M. Tarascon, *Nat. Energy* **2018**, 3, 373.

[38] a) E. Hu, X. Yu, R. Lin, X. Bi, J. Lu, S. Bak, K.-W. Nam, H. L. Xin, C. Jaye, D. A. Fischer, K. Amine, X.-Q. Yang, *Nat. Energy* **2018**, 3, 690; b) P. E. Pearce, G. Rousse, O. M. Karakulina, J. Hadermann, G. Van Tendeloo, D. Foix, F. Fauth, A. M. Abakumov, J. M. Tarascon, *Chem. Mater.* **2018**, 30, 3285; c) G. Assat, S. L. Glazier, C. Delacourt, J. M. Tarascon, *Nat. Energy* **2019**, 4, 647; d) S. Myeong, W. Cho, W. Jin, J. Hwang, M. Yoon, Y. Yoo, G. Nam, H. Jang, J.-G. Han, N.-S. Choi, M. G. Kim, J. Cho, *Nat. Commun.* **2018**, 9.

[39] K. Dai, J. Mao, Z. Zhuo, Y. Feng, W. Mao, G. Ai, F. Pan, Y. D. Chuang, G. Liu, W. Yang, *Nano Energy* **2020**, 74.

[40] a) H. Niwa, K. Higashiyama, K. Amaha, W. Kobayashi, Y. Moritomo, *J. Power Sources* **2018**, 384, 156; b) H. Wang, J. Wu, A. Dolocan, Y. Li, X. Lü, N. Wu, K. Park, S. Xin, M. Lei, W. Yang, J. B. Goodenough, *Proc. Natl. Acad. Sci. U.S.A* **2019**, 116, 23473; c) K. Dai, J. Mao, Z. Zhuo, Y. Feng, W. Mao, G. Ai, F. Pan, Y.-D. Chuang, G. Liu, W. Yang, *Nano Energy* **2020**, 74, 104831.

[41] a) Y. W. Tsai, B. J. Hwang, G. Ceder, H. S. Sheu, D. G. Liu, J. F. Lee, *Chem. Mater.* **2005**, 17, 3191; b) W.-S. Yoon, K.-B. Kim, M.-G. Kim, M.-K. Lee, H.-J. Shin, J.-M. Lee, J.-S. Lee, C.-H. Yo, *J. Phys. Chem. B* **2002**, 106, 2526; c) W.-S. Yoon, M. Balasubramanian, K. Y. Chung, X.-Q. Yang, J. McBreen, C. P. Grey, D. A. Fischer, *J. Am. Chem. Soc.* **2005**, 127, 17479.

[42] a) S. Bublil, M. Fayena-Greenstein, M. Talyanker, N. Solomatin, M. N. Tsubery, T. Bendikov, T. R. Penki, J. Grinblat, I. B. Durán, I. Grinberg, Y. Ein-Eli, Y. Elias, P. Hartmann, D. Aurbach, *J. Mater. Chem. A* **2018**, 6, 14816; b) J. Y. Hwang, J. Kim, T. Y. Yu, S. T. Myung, Y. K. Sun, *Energy Environ. Sci.* **2018**, 11, 2821; c) C. H. M. Lai, D. S. Ashby, N. H. Bashian, J. Schoiber, T. C. Liu, G. S. Lee, S. Y. Chen, P. W. Wu, B. C. Melot, B. S. Dunn, *Adv. Energy Mater.* **2019**, 9; d) J. Yang, M. Tang, H. Liu, X. Chen, Z. Xu, J. Huang, Q. Su, Y. Xia, *Small* **2019**, 15; e) C. Heubner, B. Matthey, T.

Lein, F. Wolke, T. Liebmann, C. Lämmel, M. Schneider, M. Herrmann, A. Michaelis, *Energy Storage Mater.* **2020**, 27, 377; f) M. G. T. Nathan, W. B. Park, N. Naveen, S. Park, K. S. Sohn, M. Pyo, *J. Electrochem. Soc.* **2020**, 167.

[43] a) A. Gao, M. Li, N. Guo, D. Qiu, Y. Li, S. Wang, X. Lu, F. Wang, R. Yang, *Adv. Energy Mater.* **2019**, 9; b) J. Yang, J. Zhang, V. W. H. Lau, M. Park, S. Lee, J. Kim, Y. M. Kang, *J. Phys. Chem. Lett.* **2020**, 11, 4059; c) Y. U. Park, J. Bai, L. Wang, G. Yoon, W. Zhang, H. Kim, S. Lee, S. W. Kim, J. P. Looney, K. Kang, F. Wang, *J. Am. Chem. Soc.* **2017**, 139, 12504.

[44] a) J.-Y. Hwang, C. S. Yoon, I. Belharouak, Y.-K. Sun, *J. Mater. Chem. A* **2016**, 4, 17952; b) P. Zhou, X. Liu, J. Weng, L. Wang, X. Wu, Z. Miao, J. Zhao, J. Zhou, S. Zhuo, *J. Mater. Chem. A* **2019**, 7, 657.

[45] a) J.-N. Zhang, Q. Li, C. Ouyang, X. Yu, M. Ge, X. Huang, E. Hu, C. Ma, S. Li, R. Xiao, W. Yang, Y. Chu, Y. Liu, H. Yu, X.-Q. Yang, X. Huang, L. Chen, H. Li, *Nat. Energy* **2019**, 4, 594; b) Y. Koyama, H. Arai, I. Tanaka, Y. Uchimoto, Z. Ogumi, *J. Mater. Chem. A* **2014**, 2, 11235.

[46] a) D. Kitsche, S. Schweidler, A. Mazilkin, H. Geßwein, F. Fauth, E. Suard, P. Hartmann, T. Brezesinski, J. Janek, M. Bianchini, *Mater. Adv.* **2020**, 1, 639; b) W. Liu, P. Oh, X. Liu, S. Myeong, W. Cho, J. Cho, *Adv. Energy Mater.* **2015**, 5; c) A. Choi, J. Lim, H.-J. Kim, S. C. Jung, H.-W. Lim, H. Kim, M.-S. Kwon, Y. K. Han, S. M. Oh, K. T. Lee, *Adv. Energy Mater.* **2018**, 8, 1702514; d) B. Han, S. Xu, S. Zhao, G. Lin, Y. Feng, L. Chen, D. G. Ivey, P. Wang, W. Wei, *ACS Appl. Mater. Interfaces* **2018**, 10, 39599; e) L. Bao, Z. Yang, L. Chen, Y. Su, Y. Lu, W. Li, F. Yuan, J. Dong, Y. Fang, Z. Ji, S. Chen, F. Wu, *ChemSusChem* **2019**, DOI: 10.1002/cssc.201900226; f) A. Choi, J. Lim, H. Kim, S. W. Doo, K. T. Lee, *ACS Appl. Energy Mater.* **2019**, 2, 3427; g) X. Ding, Y. X. Li, X. D. He, J. Y. Liao, Q. Hu, F. Chen, X. Q. Zhang, Y. Zhao, C. H. Chen, *ACS Appl. Mater. Interfaces* **2019**, 11, 31477; h) W. He, P. Liu, B. Qu, Z. Zheng, H. Zheng, P. Deng, P. Li, S. Li, H. Huang, L. Wang, Q. Xie, D. L. Peng, *Adv. Sci.* **2019**, DOI: 10.1002/advs.2018021141802114; i) P. Liu, H. Zhang, W. He, T. Xiong, Y. Cheng, Q. Xie, Y. Ma, H. Zheng, L. Wang, Z. Z. Zhu, Y. Peng, L. Mai, D. L. Peng, *J. Am. Chem. Soc.* **2019**, 141, 10876; j) K. Zhang, D. Kim, Z. Hu, M. Park, G. Noh, Y. Yang, J. Zhang, V. W.-H. Lau, S.-L. Chou, M. Cho, S.-Y. Choi, Y.-M. Kang, *Nat. Commun.* **2019**, 10; k) Y. Hu, Z. Qin, J. Pei, B. Cong, X. Yang, G. Chen, *ChemElectroChem* **2020**, 7, 246.

[47] a) R. Yu, Z. Zhang, S. Jamil, J. Chen, X. Zhang, X. Wang, Z. Yang, H. Shu, X. Yang, *ACS Appl. Mater. Interfaces* **2018**, 10, 16561; b) J. Billaud, D. Sheptyakov, S. Sallard, D. Leanza, M. Talianker, J. Grinblat, H. Sclar, D. Aurbach, P. Novák, C. Villevieille, *J. Mater. Chem. A* **2019**, 7, 15215; c) L. Guo, X. Tan, S. Liu, J. Wu, J. Ren, T. Zhao, X. Kang, H. Wang, W. Chu, *J. Alloys Compd.* **2019**, 790, 170; d) H. Li, P. Zhou, F. Liu, H. Li, F. Cheng, J. Chen, *Chem. Sci.* **2019**, 10, 1374; e) Q. Wang, S. Mariyappan, J. Vergnet, A. M. Abakumov, G. Rousse, F. Rabuel, M. Chakir, J. M. Tarascon, *Adv. Energy Mater.* **2019**, DOI: 10.1002/aenm.2019017851901785; f) M. Wang, L. Chen, M. Liu, Y. Chen, Y. Gu, *J. Alloys Compd.* **2020**, 848; g) R. Zhao, J. Zhang, G.-H. Lee, K. Zhang, V. W.-H. Lau, J.-J. Lee, I. Moudrakovski, Y.-L. Yang, F. Zou, M. Park, I. M. Hung, Y.-M. Kang, *J. Mater. Chem. A* **2020**, 8, 12424.

[48] Q. Liu, X. Su, D. Lei, Y. Qin, J. Wen, F. Guo, Y. A. Wu, Y. Rong, R. Kou, X. Xiao, F. Aguesse, J. Bareño, Y. Ren, W. Lu, Y. Li, *Nat. Energy* **2018**, 3, 936.

[49] K. Hoang, *Phys. Rev. Mater.* **2017**, 1.

[50] H. Lee, S. B. Lim, J. Y. Kim, M. Jeong, Y. J. Park, W. S. Yoon, *ACS Appl. Mater. Interfaces* **2018**, 10, 10804.

[51] a) M. Hou, J. Liu, S. Guo, J. Yang, C. Wang, Y. Xia, **2014**, 49, 83; b) Z. Sun, L. Xu, C. Dong, H. Zhang, M. Zhang, Y. Ma, Y. Liu, Z. Li, Y. Zhou, Y. Han, Y. Chen, *Nano Energy* **2019**, 63, 103887; c) S. Chen, Y. Xie, W. Chen, J. Chen, W. Yang, H. Zou, Z. Lin, *ACS Sustain. Chem. Eng.* **2020**, 8, 121; d) X. Hou, Y. Wang, J. Song, H. Gu, R. Guo, W. Liu, Y. Mao, J. Xie, *Solid State Ion.* **2018**, 325, 1; e) J. Lee, J. K. Papp, R. J. Clément, S. Sallis, D.-H. Kwon, T. Shi, W. Yang, B. D. McCloskey, G. Ceder, *Nat. Commun.* **2017**, 8.

[52] a) X. Liu, T. Huang, A. Yu, **2015**, 648, 7; b) B. Qiu, M. Zhang, L. Wu, J. Wang, Y. Xia, D. Qian, H. Liu, S. Hy, Y. Chen, K. An, Y. Zhu, Z. Liu, Y. S. Meng, *Nat. Commun.* **2016**, 7, 12108; c) M. J. Lee, E. Lho, P. Oh, Y. Son, J. Cho, *Nano Res.* **2017**, 10, 4210; d) S. N. Lim, J. Y. Seo, S. A. Song, K. Y. Kim, S. B. Park, D. S. Jung, *J. Electron. Mater.* **2017**, 46, 1855; e) K. Xu, S. Pang, Y. Wang, X. Shen, H. Wen, W. Wang, Y. Su, X. Xi, *J. Electrochem. Soc.* **2017**, 164, A2348; f) N. Leifer, I. Matlahov, E. M. Erickson, H. Sclar, F. Schipper, J. Y. Shin, C. Erk, F. F. Chesneau, J. Lampert, B. Markovsky, D. Aurbach, G. Goobes, *J. Phys. Chem. C* **2018**, 122, 3773; g) S. Pang, M. Zhu, K. Xu, X. Shen, H. Wen, Y. Su, G. Yang, X. Wu, S. Li, W. Wang, X. Xi, H. Wang, *J. Electrochem. Soc.* **2018**, 165, A1897; h) B. Chen, B. Zhao, J. Zhou, Z. Fang, Y. Huang, X. Zhu, Y. Sun, *J. Mater. Sci. Technol.* **2019**, 35, 994; i) J. Fan, G. Li, B. Li, D. Zhang, D. Chen, L. Li, *ACS Appl. Mater. Interfaces* **2019**, 11, 19950; j) S. Ramakrishnan, B. Park, J. Wu, W. Yang, B. D. McCloskey, *J. Am. Chem. Soc.* **2020**, 142, 8522; k) M. Richard, E. Fuller, J. Dahn, *Solid State Ion.* **1994**, 73, 81.

[53] E. M. Erickson, H. Sclar, F. Schipper, J. Liu, R. Tian, C. Ghanty, L. Burstein, N. Leifer, J. Grinblat, M. Talianker, J. Y. Shin, J. K. Lampert, B. Markovsky, A. I. Frenkel, D. Aurbach, *Adv. Energy Mater.* **2017**, 7.

[54] a) D. S. Ko, J. H. Park, S. Park, Y. N. Ham, S. J. Ahn, J. H. Park, H. N. Han, E. Lee, W. S. Jeon, C. Jung, *Nano Energy* **2019**, 56, 434; b) O. C. Harris, S. E. Lee, C. Lees, M. Tang, *J. Phys.: Energy* **2020**, 2, 032002; c) D. Leanza, C. A. F. Vaz, G. Melinte, X. Mu, P. Novak, M. El Kazzi, *ACS Appl Mater Interfaces* **2019**, 11, 6054.

[55] a) I. Takahashi, H. Kiuchi, A. Ohma, T. Fukunaga, E. Matsubara, *J. Phys. Chem. C* **2020**, 124, 9243; b) S. Y. Liu, L. D. Y. Wang, C. C. Zhang, B. B. Chu, C. P. Wang, T. Huang, A. S. Yu, *J. Power Sources* **2019**, 438, 226979; c) Q. Li, Y. Wang, X. Wang, X. Sun, J. N. Zhang, X. Yu, H. Li, *ACS Appl Mater Interfaces* **2020**, 12, 2319.

[56] a) H.-H. Ryu, K.-J. Park, C. S. Yoon, Y.-K. Sun, *Chem. Mater.* **2018**, 30, 1155; b) P. Yan, J. Zheng, M. Gu, J. Xiao, J. G. Zhang, C. M. Wang, *Nat. Commun.* **2017**, 8, 14101; c) A. O. Kondrakov, A. Schmidt, J. Xu, H. Geßwein, R. Mönig, P. Hartmann, H. Sommer, T. Brezesinski, J. Janek, *J. Phys. Chem. C* **2017**, 121, 3286.

[57] a) R. Sahore, D. C. O'Hanlon, A. Tornheim, C. W. Lee, J. C. Garcia, H. Iddir, M. Balasubramanian, I. Bloom, *J. Electrochem. Soc.* **2020**, 167, 020513; b) W. Li, *J. Electrochem. Soc.* **2020**, 167; c) D. R. Gallus, R. Schmitz, R. Wagner, B. Hoffmann, S. Nowak, I. Cekic-Laskovic, R. W. Schmitz, M. Winter, *Electrochim. Acta* **2014**, 134, 393.

[58] a) H. S. Liu, J. M. Foster, A. Gully, S. Krachkovskiy, M. Jiang, Y. Wu, X. Y. Yang, B. Protas, G. R. Goward, G. A. Botton, *J. Power Sources* **2016**, 306, 300; b) D. J. Miller, C. Proff, J. G. Wen, D. P. Abraham, J. Bareno, *Adv. Energy Mater.* **2013**, 3, 1098.

[59] a) H. Yoshizawa, T. Ohzuku, *Electrochem.* **2003**, 71, 1177; b) N. Yabuuchi, T.

Ohzuku, *J. Power Sources* **2003**, 119, 171; c) T. Ohzuku, Y. Makimura, *Chem. Lett.* **2001**, 30, 642; d) Z. Lu, D. D. MacNeil, J. R. Dahn, *Electrochem. Solid-State Lett.* **2001**, 4, A200.

[60]   a) J. Li, A. R. Cameron, H. Li, S. Glazier, D. Xiong, M. Chatzidakis, J. Allen, G. A. Botton, J. R. Dahn, *J. Electrochem. Soc.* **2017**, 164, A1534; b) Y. L. Liu, J. Harlow, J. Dahn, *J. Electrochem. Soc.* **2020**, 167, 020512; c) F. Friedrich, B. Strehle, A. T. S. Freiberg, K. Kleiner, S. J. Day, C. Erk, M. Piana, H. A. Gasteiger, *J. Electrochem. Soc.* **2019**, 166, A3760.

[61]   T. Kimijima, N. Zettsu, K. Yubuta, K. Hirata, K. Kami, K. Teshima, *J. Mater. Chem. A* **2016**, 4, 7289.

[62]   F. Fu, G. L. Xu, Q. Wang, Y. P. Deng, X. Li, J. T. Li, L. Huang, S. G. Sun, *J. Mater. Chem. A* **2013**, 1, 3860.

[63]   a) J. Li, R. Yao, C. Cao, *ACS Appl Mater Interfaces* **2014**, 6, 5075; b) W. B. Pi, T. Mei, Z. X. Zhang, X. Li, J. Y. Wang, J. H. Li, X. B. Wang, *Crystengcomm* **2017**, 19, 442.

[64]   a) Z. Chang, Z. Chen, F. Wu, X.-Z. Yuan, H. Wang, *Electrochim. Acta* **2009**, 54, 6529; b) K. Du, Z. D. Peng, G. R. Hu, Y. N. Yang, L. Qi, *J. Alloys Compd.* **2009**, 476, 329; c) M. V. Reddy, G. V. S. Rao, B. V. R. Chowdari, *J. Power Sources* **2006**, 159, 263.

[65]   J. C. Garcia, J. Bareño, J. Yan, G. Chen, A. Hauser, J. R. Croy, H. Iddir, *J. Phys. Chem. C* **2017**, 121, 8290.

[66]   G. Chen, B. Hai, A. K. Shukla, H. Duncan, *J. Electrochem. Soc.* **2012**, 159, A1543.

[67]   J. Zhu, G. Chen, *J. Mater. Chem. A* **2019**, 7, 5463.

[68]   a) J. Li, R. Yao, C. Cao, *ACS Appl. Mater. Interfaces* **2014**, 6, 5075; b) X. Ju, H. Huang, W. He, H. Zheng, P. Deng, S. Li, B. Qu, T. Wang, *ACS Sustain. Chem. Eng.* **2018**, 6, 6312; c) M. Jiang, Q. Zhang, X. Wu, Z. Chen, D. L. Danilov, R.-A. Eichel, P. H. L. Notten, *ACS Appl. Energy Mater.* **2020**, 3, 6583.

[69]   L. Zou, W. Zhao, H. Jia, J. Zheng, L. Li, D. P. Abraham, G. Chen, J. R. Croy, J.-G. Zhang, C. Wang, *Chem. Mater.* **2020**, 32, 2884.

[70]   J.-H. Kim, S. J. Kim, T. Yuk, J. Kim, C. S. Yoon, Y.-K. Sun, *ACS Energy Lett.* **2018**, 3, 3002.

[71]   S. Y. Lee, G. S. Park, C. Jung, D. S. Ko, S. Y. Park, H. G. Kim, S. H. Hong, Y. Zhu, M. Kim, *Adv. Sci.* **2019**, 6, 1800843.

[72]   J. Zhu, S. Sharifi-Asl, J. C. Garcia, H. H. Iddir, J. R. Croy, R. Shahbazian-Yassar, G. Chen, *ACS Appl. Energy Mater.* **2020**, 3, 4799.

[73]   F. Zhang, S. Lou, S. Li, Z. Yu, Q. Liu, A. Dai, C. Cao, M. F. Toney, M. Ge, X. Xiao, W. K. Lee, Y. Yao, J. Deng, T. Liu, Y. Tang, G. Yin, J. Lu, D. Su, J. Wang, *Nat. Commun.* **2020**, 11, 3050.

[74]   a) E. J. Cheng, K. Hong, N. J. Taylor, H. Choe, J. Wolfenstine, J. Sakamoto, *J. Eur. Ceram. Soc.* **2017**, 37, 3213; b) W. Cho, J. H. Song, K. W. Lee, M. W. Lee, H. Kim, J. S. Yu, Y. J. Kim, K. J. Kim, *J. Phys. Chem. Lett.* **2018**, 123, 271; c) J. M. Lim, T. Hwang, D. Kim, M. S. Park, K. Cho, M. Cho, *Sci. Rep.* **2017**, 7, 39669.

[75]   a) H. Bockholt, M. Indrikova, A. Netz, F. Golks, A. Kwade, *J. Power Sources* **2016**, 325, 140; b) T. Günther, D. Schreiner, A. Metkar, C. Meyer, A. Kwade, G. Reinhart, *Energy Technol.* **2019**, 8, 1900026.

[76]   a) B. W. Xiao, X. L. Sun, *Adv. Energy Mater.* **2018**, 8, 1802057; b) S. Kalluri, M. Yoon, M. Jo, H. K. Liu, S. X. Dou, J. Cho, Z. Guo, *Adv. Mater.* **2017**, 29, 1605807; c) J. Cabana, B. J. Kwon, L. Hu, *Acc. Chem. Res.* **2018**, 51, 299; d) L. Liang, W. Zhang,

F. Zhao, D. K. Denis, F. U. Zaman, L. Hou, C. Yuan, *Adv. Mater. Interfaces* **2020**, 7, 1901749.

[77]   H. H. Sun, H.-H. Ryu, U.-H. Kim, J. A. Weeks, A. Heller, Y.-K. Sun, C. B. Mullins, *ACS Energy Lett.* **2020**, 5, 1136.

[78]   a) Y. K. Sun, S. T. Myung, M. H. Kim, J. Prakash, K. Amine, *J. Am. Chem. Soc.* **2005**, 127, 13411; b) D.-W. Jun, C. S. Yoon, U.-H. Kim, Y.-K. Sun, *Chem. Mater.* **2017**, 29, 5048; c) C. S. Yoon, K.-J. Park, U.-H. Kim, K. H. Kang, H.-H. Ryu, Y.-K. Sun, *Chem. Mater.* **2017**, 29, 10436; d) Y. K. Sun, S. T. Myung, B. C. Park, J. Prakash, I. Belharouak, K. Amine, *Nat. Mater.* **2009**, 8, 320.

[79]   C. S. Yoon, S. J. Kim, U. H. Kim, K. J. Park, H. H. Ryu, H. S. Kim, Y. K. Sun, *Adv. Funct. Mater* **2018**, 28.

[80]   C. S. Yoon, S. J. Kim, U.-H. Kim, K.-J. Park, H.-H. Ryu, H.-S. Kim, Y.-K. Sun, *Adv. Funct. Mater* **2018**, 28, 1802090.

[81]   Y. K. Sun, S. T. Myung, B. C. Park, J. Prakash, I. Belharouak, K. Amine, *Nat. Mater.* **2009**, 8, 320.

[82]   P. Y. Hou, H. Z. Zhang, Z. Y. Zi, L. Q. Zhang, X. J. Xu, *J. Mater. Chem. A* **2017**, 5, 4254.

[83]   a) R. Amin, M. Chiang, *J. Electrochem. Soc.* **2016**, 163, A1512; b) S. Burkhardt, M. S. Friedrich, J. K. Eckhardt, A. C. Wagner, N. Bohn, J. R. Binder, L. M. Chen, M. T. Elm, J. Janek, P. J. Klar, *ACS Energy Lett.* **2019**, 4, 2117.

[84]   R. Y. Tian, N. Alcala, S. J. K. O'Neill, D. V. Horvath, J. Coelho, A. J. Griffin, Y. Zhang, V. Nicolosi, C. O'Dwyer, J. N. Coleman, *ACS Appl. Energy Mater.* **2020**, 3, 2966.

[85]   Y. Yu, Y. Luo, H. Wu, K. Jiang, Q. Li, S. Fan, J. Li, J. Wang, *Nanoscale* **2018**, 10, 19972.

[86]   a) C. Venkateswara Rao, A. Leela Mohana Reddy, Y. Ishikawa, P. M. Ajayan, *ACS Appl. Mater. Interfaces* **2011**, 3, 2966; b) K. C. Jiang, X. L. Wu, Y. X. Yin, J. S. Lee, J. Kim, Y. G. Guo, *ACS Appl. Mater. Interfaces* **2012**, 4, 4858; c) J.-r. He, Y.-f. Chen, P.-j. Li, Z.-g. Wang, F. Qi, J.-b. Liu, *RSC Adv.* **2014**, 4, 2568; d) Z. Zhuang, L. Yang, B. Ju, G. Lei, Q. Zhou, H. Liao, A. Yin, Z. Deng, Y. Tang, S. Qin, F. Tu, *ChemistrySelect* **2020**, 5, 2291.

[87]   X. Li, X. Zhao, M. S. Wang, K. J. Zhang, Y. Huang, M. Z. Qu, Z. L. Yu, D. S. Geng, W. G. Zhao, J. M. Zheng, *RSC Adv.* **2017**, 7, 24359.

[88]   S. Yang, Q. Fan, Z. Shi, L. Liu, J. Liu, X. Ke, J. Liu, C. Hong, Y. Yang, Z. Guo, *ACS Appl. Mater. Interfaces* **2019**, 11, 36742.

[89]   a) H. Wang, W. Ge, W. Li, F. Wang, W. Liu, M. Z. Qu, G. Peng, *ACS Appl. Mater. Interfaces.* **2016**, 8, 18439; b) B. Li, G. Li, D. Zhang, J. Fan, D. Chen, Y. Ge, F. Lin, C. Zheng, L. Li, *ChemistrySelect* **2019**, 4, 6354.

[90]   Y. K. Han, S. Heng, Y. Wang, Q. T. Qu, H. H. Zheng, *ACS Energy Lett.* **2020**, 5, 2421.

[91]   Q. Gan, N. Qin, Y. Zhu, Z. Huang, F. Zhang, S. Gu, J. Xie, K. Zhang, L. Lu, Z. Lu, *ACS Appl. Mater. Interfaces* **2019**, 11, 12594.

[92]   P. F. Yan, J. M. Zheng, J. Liu, B. Q. Wang, X. P. Cheng, Y. F. Zhang, X. L. Sun, C. M. Wang, J. G. Zhang, *Nat. Energy* **2018**, 3, 600.

[93]   G. L. Xu, Q. Liu, K. K. S. Lau, Y. Liu, X. Liu, H. Gao, X. W. Zhou, M. H. Zhuang, Y. Ren, J. D. Li, M. H. Shao, M. G. Ouyang, F. Pan, Z. H. Chen, K. Amine, G. H. Chen, *Nat. Energy* **2019**, 4, 484.

[94]   a) S. H. Ju, I.-S. Kang, Y.-S. Lee, W.-K. Shin, S. Kim, K. Shin, D.-W. Kim, *ACS Appl.*

Mater. Interfaces **2014**, 6, 2546; b) Y.-S. Lee, W.-K. Shin, A. G. Kannan, S. M. Koo, D.-W. Kim, *ACS Appl. Mater. Interfaces* **2015**, 7, 13944.

[95]   a) J. R. van Ommen, A. Goulas, *Mater. Today Chem.* **2019**, 14, 100183; b) A. S. Yersak, K. Sharma, J. M. Wallas, A. A. Dameron, X. M. Li, Y. G. Yang, K. E. Hurst, C. M. Ban, R. C. Tenent, S. M. George, *J. Vac. Sci. Technol. A* **2018**, 36, 01A123.
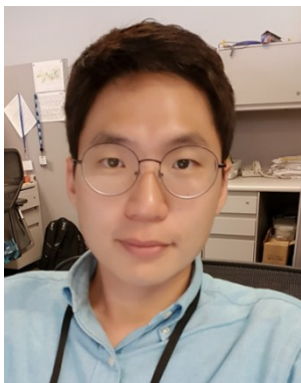
Gi-Hyeok Lee received his B.S. in Chemistry from Dongguk University in 2015. Presently, he is a Ph. D. candidate in Department of Energy and Materials Engineering, Dongguk university under the supervision of Prof. Yong-Mook Kang and has been a doctoral fellow in Advanced Light Source division of Lawrence Berkeley National Laboratory since 2019. His current research interests cover the reaction mechanism of the energy storage materials based on experimental techniques including X-ray spectroscopies and electrochemistry.

Vincent Wing-hei Lau received his B.Sc (Hons I) in 2006 and PhD in 2011 under the supervision of Prof. Thomas Maschmeyer. He joined the Max Planck Institute of Solid State Research as a postdoctoral researcher in 2012, was appointed as Research Professor in Dongguk University in 2017, and then transferred to Korea University in 2020. His research focuses on the chemistry of materials and their interfaces as relevant to applications in photo-/electrochemical energy conversion and storage.

Wanli Yang received his B.S. in Physics from Shandong University, China (1995), and his Ph. D. in Condensed Matter Physics from Insititute of Physics, Chinese Academy of Sciences (2000). He was a postdoctoral fellow at Stanford University, and then a staff scientist at the Geballe Laboratory for Adv. Mater. at Stanford University, working on photo-electron spectroscopy of nano materials. He has been a physicist scientist at the Advanced Light Source division of Lawrence Berkeley National Laboratory since 2006. His current research interests include novel instrumentation and methodology of employing soft X-ray spectroscopy for studying energy harvesting and storage materials.

Yong-Mook Kang received his B.S.(1999), M.S.(2001), Ph. D. (2004) in Materials Science and Engineering from Korea Advanced Institute of Science and Technology. He is currently a professor at Department of Materials Science and Engineering in Korea University. He. He was a senior researcher in Samsung SDI Co., LTD, a professor in Dongguk University, and has been a fellow of Royal Society of Chemistry from 2015 and member of Young Academy of Science and Technology from 2020. His research area covers electrode or catalyst materials for Li rechargeable batteries and various next-generation energy storage systems.

Utilizing oxygen redox in layered oxides is central to overcoming the capacity limitation of current cathode materials in lithium ion batteries. This review critically analyses this phenomenon from the atomic to microstructure scale, summarizing recent advances in understanding the reaction mechanism, reappraising research methodologies, and evaluating various strategies for harnessing this redox center for charge storage.

Gi-Hyeok Lee†, Dr. Vincent Wing-hei Lau†, Dr. Wanli Yang* and Prof. Yong-Mook Kang*

Utilizing oxygen redox in layered cathode materials from multi-scale perspective

ToC figure ((Please choose one size: 55 mm broad × 50 mm high **or** 110 mm broad × 20 mm high. Please do not use any other dimensions))